

**The deconfinement transition in an
effective theory for heavy quark
Lattice QCD to $\mathcal{O}(\kappa^4)$**

Institute for Theoretical Physics
Goethe-Universität Frankfurt

Master's Thesis

Miguel Salg

5th November, 2020

Supervisor and first referee: Prof. Dr. Owe Philipsen
Second referee: Prof. Dr. Marc Wagner

Abstract

In this Master's Thesis, we study a three-dimensional effective theory for Lattice QCD in the strong coupling and heavy quark regime with a Monte Carlo simulation. In the numerical code, the effective action is implemented up to the order κ^4 in the hopping parameter κ . This simulation program is then used to measure the phase diagram of the effective theory at zero chemical potential. In particular, we determine the phase boundary of the deconfinement transition and the critical end point, where its type changes from first order to crossover. These investigations are carried out for one and two degenerate quark flavours, and for two different values of the temporal lattice extent ($N_\tau = 4$ and 6). Additionally, a further approximation of the effective theory in the limit of large N_τ and its range of validity at finite temperatures are discussed. On the analytical side, we derive the $\mathcal{O}(\kappa^6)$ -corrections to the nearest-neighbour fermion interaction. Finally, a resummation scheme that is specific to the nearest-neighbour interaction is constructed, which facilitates the evaluation of a certain kind of terms.

Contents

Abstract	2
1. Introduction	5
2. An effective theory for (Lattice) QCD	7
2.1. QCD in the continuum	7
2.2. QCD on the lattice	9
2.3. General idea and purpose of the effective theory	11
2.4. The strong coupling expansion	12
2.5. The hopping parameter expansion	13
2.5.1. The static quark determinant	14
2.5.2. The kinetic quark determinant: general approach	15
2.5.3. The kinetic quark determinant: results for the leading and next-to-leading order	20
2.6. Gauge corrections	20
2.7. Resummation of the effective action	21
2.8. Transformation to Polyakov loops	22
3. Numerical results	24
3.1. The integration measure	24
3.2. The Monte Carlo method and the Metropolis algorithm	25
3.3. Implementation of the effective action and parallelisation	27
3.4. The Polyakov loop as an observable for the deconfinement transition	29
3.5. Data analysis	31
3.6. The deconfinement transition at zero chemical potential	34
3.6.1. The analysis using the example of static quarks	35
3.6.2. Effect of larger-distance interactions in the gauge action	37
3.6.3. The critical point of the one-flavour theory to $\mathcal{O}(\kappa^4)$	38
3.6.4. The critical point of the two-flavour theory to $\mathcal{O}(\kappa^4)$	43
3.7. Range of validity of the large- N_τ approximation	45
4. Higher-order corrections to the nearest-neighbour fermion interaction	49
4.1. The Dirac trace	49
4.2. Integration over spatial links	51
4.3. Evaluation of the temporal sums	54
4.3.1. Traces	54
4.3.2. Determinants	58
4.4. Ladder resummation	61
5. Conclusions and outlook	64
Acknowledgements	66

A. Appendix	67
A.1. Series expansions for the effective couplings	67
A.2. Gauge integrals	68
A.3. Additional analytical calculations for SU(3)-matrices	70
A.3.1. Application of the Cayley-Hamilton theorem for SU(3)-matrices	70
A.3.2. Determinants of 3×3 -matrices	71
A.4. Results for the kinetic quark determinant up to $\mathcal{O}(\kappa^4)$	71
A.4.1. Two-point interaction	71
A.4.2. Three-point interaction	73
A.4.3. Four-point interaction	73
A.5. Additional plots for static quarks	74
A.6. Plots using the ‘full’ implemented action	76
A.6.1. One-flavour theory with $N_\tau = 4$	76
A.6.2. One-flavour theory with $N_\tau = 6$	78
A.6.3. Two-flavour theory with $N_\tau = 4$	79
A.6.4. Two-flavour theory with $N_\tau = 6$	81
A.7. Plots for the study of the large- N_τ approximation	82
A.8. Result for the $\mathcal{O}(\kappa^6)$ -contribution to the nearest-neighbour fermion interaction	84

1. Introduction

The elementary particles which make up the visible matter in our universe are described by the Standard Model of particle physics: the fermionic quarks and leptons, and the bosonic exchange particles. They can interact through four fundamental forces: the strong, weak, electromagnetic and gravitational interactions. The theoretical formulation of the Standard Model is realised in terms of Quantum Field Theories. Three of the four above-mentioned forces can be represented in this way; only gravity is not yet included.

The theory of the strong interaction in the context of the Standard Model is Quantum Chromodynamics (QCD). It contains fermions – the quarks – in six flavours (up, down, strange, charm, bottom and top), which additionally come in three different colours (red, green and blue). The colour charges of the quarks are assigned to the fundamental representation of the gauge group of QCD, which is $SU(3)$. The exchange particles mediating the strong force are called gluons. They carry a colour charge in the adjoint representation of $SU(3)$ and thus appear in $3^2 - 1 = 8$ species.

Two of the most prominent features of QCD are confinement and asymptotic freedom. These are due to the self-interaction of the gluons. At large distances or low energies, the coupling of QCD is large and it exhibits colour confinement: The only finite-energy asymptotic states of the theory are those that are singlets of $SU(3)$, or – in other words – colour neutral. This means that colour charged particles, like the quarks, cannot be isolated and have to form composite particles, the hadrons. Here, one distinguishes between baryons and mesons: The former ones consist of three quarks, while the latter ones are built from one quark and one antiquark. The situation is the opposite at small distances or high energies: The coupling of QCD weakens, and the quarks and gluons are quasi-free. One refers to such behaviour as asymptotic freedom, and the state of the particles is called quark-gluon plasma.

The existence of two so completely dissimilar states of strongly interacting matter suggests a rich phase structure of QCD. The phase diagram in the temperature-chemical potential plane is sketched in fig. 1.1. Despite decades of intense theoretical and experimental research, vast parts of it are still driven by speculation. There is, however, widespread agreement that the deconfinement transition, which delineates the boundary between the confined phase and the quark-gluon plasma, is an analytic crossover at zero chemical potential and finite temperature. At zero temperature and finite chemical potential, it is believed to be a first-order phase transition. It is hence highly suggestive that a second-order critical end point exists at some intermediary values of the parameters. The nuclear liquid-gas transition, which is also of first order, is found at zero temperature and a baryon chemical potential around the mass of the nucleon. At even larger chemical potentials, some models predict a (number of) colour superconducting phase(s).

Owing to the large coupling constant, the low-energy (confinement) regime of QCD is inaccessible to perturbative methods. A very powerful tool to study the theory non-perturbatively is Lattice QCD. Here, one replaces space-time by a four-dimensional Euclidean lattice. It serves as a natural regulator for the quantum field theory, and allows for both analytical

1. Introduction

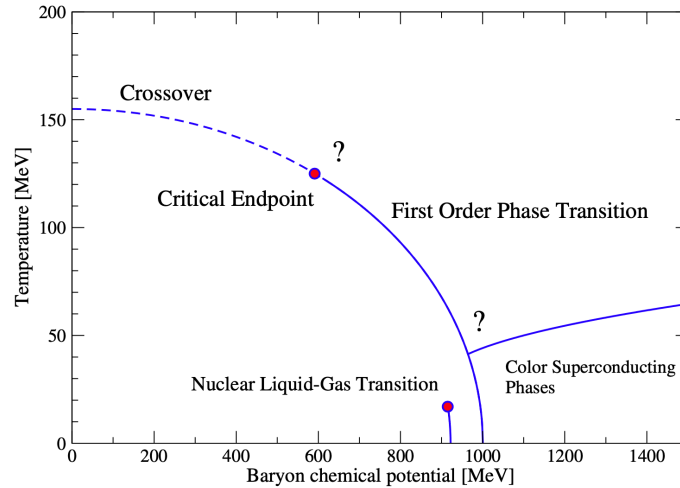


Figure 1.1.: Sketch of the QCD phase diagram in the temperature and baryon chemical potential plane [1]

understanding and computational research. However, the infamous sign problem seriously hampers any numerical investigations at finite chemical potential, thus calling for effective theories.

This thesis starts with a brief recapitulation of the essentials of continuum QCD and its lattice discretisation in chapter 2. We will then demonstrate how one can construct an effective theory for Lattice QCD in the limit of strong coupling and heavy quarks. Afterwards, two additional details will be discussed: the resummation of the resulting effective action back to an exponential form and the transformation of the degrees of freedom to Polyakov loops. Chapter 3 deals with the implementation of a numerical Monte Carlo simulation of the effective theory. This will be employed to explore the phase diagram of the effective theory at zero chemical potential. In particular, we will locate the phase boundary of the deconfinement transition and the critical end point, where its nature changes from first order to crossover, in the parameter space of the couplings. Such measurements will be performed for one and two degenerate quark flavours. Apart from this, a further approximation of the effective action and its range of validity will be examined. Chapter 4 is dedicated to more analytical questions. Here, we will derive higher-order corrections to certain parts of the effective action. Chapter 5 finally draws some conclusions and gives an outlook for possible further inquiries.

2. An effective theory for (Lattice) QCD

In the present chapter, we will review the basics of the lattice discretisation of QCD and explain the general procedure for the derivation of the effective theory used in this thesis. Moreover, the resulting action will be presented up to the order implemented in the numerical simulation (cf. chapter 3).

2.1. QCD in the continuum

Most physicists agree that Quantum Chromodynamics (QCD) is the correct theoretical description of the strong nuclear force. It is a non-Abelian gauge theory with gauge group $SU(3)$, coupled to fermions (quarks) in the fundamental representation [2]. The Lagrangian therefore consists of a fermionic part \mathcal{L}_F and a gauge part \mathcal{L}_G :

$$\mathcal{L}_{\text{QCD}} = \mathcal{L}_F + \mathcal{L}_G = \sum_{f=1}^{N_f} \bar{\psi}^f(x) \left(i\gamma^\mu D_\mu - m^f \right) \psi^f(x) - \frac{1}{4} F_{\mu\nu}^a(x) F^{\mu\nu a}(x). \quad (2.1)$$

Here, the sum in the first term runs over the individual flavours $f = 1, \dots, N_f$ of the quarks, which are described by Dirac 4-spinors $\psi^f(x)$. The gluons are represented by the gauge fields $A_\mu^a(x)$, contained in the covariant derivative and the field strength tensor:

$$D_\mu = \partial_\mu - igA_\mu^a(x)T^a, \quad T^a = \frac{\lambda^a}{2}, \quad (2.2)$$

$$F_{\mu\nu}^a(x) = \partial_\mu A_\nu^a(x) - \partial_\nu A_\mu^a(x) + gf^{abc}A_\mu^b(x)A_\nu^c(x). \quad (2.3)$$

The quark and gluon fields also carry colour and Dirac indices, which have been suppressed in favour of a matrix/vector notation. g is the coupling constant of QCD; f^{abc} are the structure constants of $SU(3)$ and T^a its generators, which satisfy the commutation relations $[T^a, T^b] = if^{abc}T^c$. The Dirac matrices obey the anticommutation relations $\{\gamma^\mu, \gamma^\nu\} = 2g^{\mu\nu}$, where the metric is $g^{\mu\nu} = \eta^{\mu\nu}$ in Minkowski space.

Using this Lagrangian, it is possible to express the transition amplitude between two field configurations as a Feynman path integral:

$$\langle \phi_1 | e^{-iH(t_2-t_1)} | \phi_2 \rangle \propto \int [d\bar{\psi}][d\psi][dA] \exp \left(i \int dt \int d^3x \mathcal{L}_{\text{QCD}} \right), \quad (2.4)$$

where H is the Hamiltonian and the quantity in the exponent on the right-hand side is called the action. It is given by the space-time integral over the Lagrangian:

$$S_{\text{QCD}} = \int dt \int d^3x \mathcal{L}_{\text{QCD}}. \quad (2.5)$$

It turns out that it is difficult to give a satisfactory mathematical meaning to the measure of the path integral in eq. (2.4) [3]. This is due to the fact that the integral is complex and strongly

2. An effective theory for (Lattice) QCD

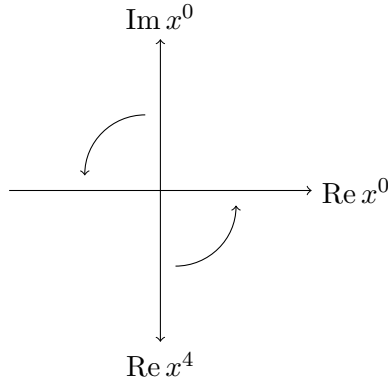


Figure 2.1.: Illustration of the Wick rotation, indicated by curved arrows (adapted from [3])

oscillating because of the complex weight e^{iS} in the integrand. For a numerical treatment of the theory this behaviour is also highly problematic. It is therefore common to switch to a purely imaginary time coordinate

$$x^0 = -ix^4, \quad x^4 = \tau \in \mathbb{R}, \quad (2.6)$$

by performing a so-called Wick rotation (cf. fig. 2.1). The space-time metric for the coordinates x^1, \dots, x^4 is then a Euclidean one: $g_{\mu\nu} = \delta_{\mu\nu}$. Moreover, the time evolution operator $\exp(-iHt)$ has to be replaced by $\exp(-H\tau)$, which is a well-defined positive operator [3]. The expression for the Euclidean transition amplitude then looks like:

$$\langle \phi_1 | e^{-H(\tau_2 - \tau_1)} | \phi_2 \rangle \propto \int [d\bar{\psi}][d\psi][dA] \exp\left(-\int d^4x \mathcal{L}_{\text{QCD}}^{(E)}\right). \quad (2.7)$$

The weight factor is now given by the exponential of the Euclidean action $S^{(E)} = -iS$. After an appropriate transformation of the Dirac matrices and the gauge fields, the Euclidean Lagrangian of QCD can be written as [4]

$$\mathcal{L}_{\text{QCD}}^{(E)} = \mathcal{L}_F^{(E)} + \mathcal{L}_G^{(E)} = \sum_{f=1}^{N_f} \bar{\psi}^f(x) (\gamma^\mu D_\mu + m^f) \psi^f(x) + \frac{1}{4} F_{\mu\nu}^a(x) F^{a\mu\nu}(x). \quad (2.8)$$

Another major advantage of the Euclidean formulation of Quantum Field Theories is that it exhibits a structural equivalence with statistical mechanics [4]. The grand canonical partition function of a quantum mechanical many-body system has the form

$$Z = \text{tr} \left[e^{-\beta(H - \mu N_q)} \right], \quad \beta = \frac{1}{T}. \quad (2.9)$$

This has a striking similarity with the functional integral from eq. (2.7), if one makes the formal identification $\beta H \leftrightarrow S^{(E)}$. As the Euclidean quark number operator is given by the spatial volume integral over the temporal component of the conserved vector current $\bar{\psi}(x)\gamma_4\psi(x)$,

$$N_q = \int d^3x \bar{\psi}(x)\gamma_4\psi(x), \quad (2.10)$$

one has to add such a term to the Dirac operator in eq. (2.8) in order to allow for finite chemical potential. The partition function for Euclidean QCD at finite temperature and density then

takes the form of a path integral:

$$Z_{\text{QCD}} = \int [d\bar{\psi}][d\psi][dA] e^{-S_{\text{QCD}}^{(E)}} = \int [d\bar{\psi}][d\psi][dA] \exp\left(-\int_0^\beta d\tau \int_{\mathbb{R}^3} d^3x \mathcal{L}_{\text{QCD}}^{(E)}\right), \quad (2.11)$$

$$\mathcal{L}_{\text{QCD}}^{(E)} = \sum_{f=1}^{N_f} \bar{\psi}^f(x) (\gamma^\mu D_\mu + m^f - \gamma_4 \mu^f) \psi^f(x) + \frac{1}{4} F_{\mu\nu}^a(x) F^{a\mu\nu}(x). \quad (2.12)$$

2.2. QCD on the lattice

The Euclidean formulation of QCD cures the problem of having an imaginary exponent in the integrand as long as the action $S_{\text{QCD}}^{(E)}$ is real. The path integral in eq. (2.11), however, is still an infinite-dimensional integral. Therefore, one introduces a hypercubical lattice

$$\Lambda = \{x = (x_1, x_2, x_3, x_4) \mid x_{1,2,3} = 0, 1, \dots, N_s - 1; x_4 = 0, 1, \dots, N_\tau - 1\} \quad (2.13)$$

to replace space-time, where a is referred to as lattice constant. The spatial extent of the lattice is given by N_s and the temporal extent by N_τ . Hence, the lattice consists of a total of $N_s^3 N_\tau$ points. As one can see from the upper bound of the τ -integral in eq. (2.11), the size of the lattice in the temporal direction is related to the inverse temperature:

$$T = \frac{1}{aN_\tau}. \quad (2.14)$$

The introduction of a finite lattice spacing a has two major advantages: On the one hand, the number of dimensions becomes finite, making the path integral in eq. (2.11) mathematically well-defined and numerically computable. On the other hand, the lattice provides a natural regulator for the theory by introducing a momentum cut-off $2\pi/a$ [3]. In this context, it is useful to distinguish two different limiting procedures: For the thermodynamic limit, one has to take the infinite volume limit at fixed lattice spacing and temperature:

$$N_s \rightarrow \infty, N_\tau \text{ fixed}, a \text{ fixed} \Rightarrow aN_s \rightarrow \infty, T \text{ fixed}. \quad (2.15)$$

In this limit, the allowed momenta become continuous, but the cut-off remains intact. For the continuum limit, one keeps physical volume and temperature fixed:

$$N_s \rightarrow \infty, N_\tau \rightarrow \infty, a \rightarrow 0 \Rightarrow aN_s \text{ fixed}, T \text{ fixed}, \quad (2.16)$$

so that the momenta remain discrete, but the cut-off is removed. Another important point concerns the correct boundary conditions. For bosonic fields, the appropriate boundary conditions are periodic in all directions. Fermions by contrast obey the Pauli principle, which implies that their boundary conditions have to be chosen antiperiodic in time and periodic in space.

In order to apply the lattice method to QCD, one has to find a suitable discretisation of the action. We will start the discussion with the gauge part, as this is relatively straightforward. For the transcription of the concept of a gauge field to the case of a lattice regularisation of the Euclidean continuum it is useful to view these fields as parallel transporters. On a lattice with shortest distance a the elementary parallel transporters are those associated with the links (or bonds) connecting nearest neighbouring points x and $x + a\hat{\mu}$. The parallel transporter which

2. An effective theory for (Lattice) QCD

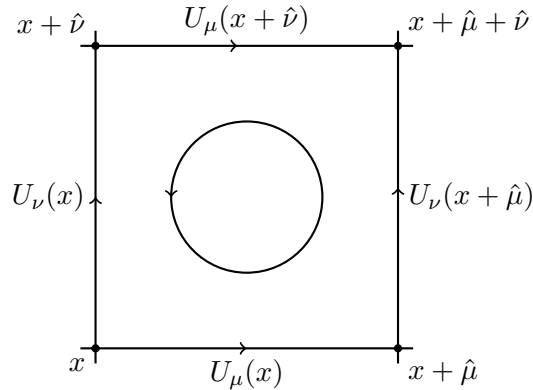


Figure 2.2.: The four link variables which build up the plaquette $U_{\mu\nu}(x)$. The circle indicates the order that the links are run through in the plaquette [4]

corresponds to this bond is called link variable $U_\mu(x)$ and is related to the continuum gauge field via [3]

$$U_\mu(x) = e^{igaA_\mu^a(x)T^a} \in \text{SU}(3). \quad (2.17)$$

Since the Lagrangian has to be gauge invariant, one has to find gauge invariant quantities built from these link variables. The simplest one is a trace over a closed loop of link variables. For the construction of the gauge action it is sufficient to use the shortest, non-trivial closed loop, the so-called plaquette (cf. fig. 2.2)

$$\begin{aligned} U_p &= U_{\mu\nu}(x) = U_\mu(x)U_\nu(x + \hat{\mu})U_{-\mu}(x + \hat{\mu} + \hat{\nu})U_{-\nu}(x + \hat{\nu}) \\ &= U_\mu(x)U_\nu(x + \hat{\mu})U_\mu^\dagger(x + \hat{\nu})U_\nu^\dagger(x). \end{aligned} \quad (2.18)$$

The action which has been proposed by Wilson for lattice gauge theory [5] is given by a sum over all plaquettes, including every plaquette with only one orientation [4]:

$$S_G[U] = \frac{2}{g^2} \sum_p \text{Re tr}(\mathbf{1} - U_p) = \frac{\beta}{3} \sum_{x \in \Lambda} \sum_{\mu < \nu} \text{Re tr}(\mathbf{1} - U_{\mu\nu}(x)). \quad (2.19)$$

Here, the inverse lattice coupling $\beta = 6/g^2$ (not to be confused with the inverse temperature from eqs. (2.9) and (2.11)!) has been introduced. It is easy to prove that this action converges to the Yang-Mills action in the (naive) continuum limit $a \rightarrow 0$ [4].

It turns out to be far more complicated to derive a discretised version of the fermionic part of the QCD Lagrangian. The simplest way of constructing a gauge invariant Lagrangian with the correct naive continuum limit exhibits a phenomenon called fermion doubling. The propagator for free fermions, which is given by the inverse of the Dirac operator, has $2^4 = 16$ poles, one at each corner of the Brillouin zone [4]. This means that 15 unphysical poles arise, the doublers. A possible solution to remove these in the continuum limit was suggested by Wilson [6]. He added an extra term to the action which behaves like a second derivative. The full Wilson-Dirac action then reads [4]:

$$\begin{aligned} S_{F,W}[\psi, \bar{\psi}, U] &= \sum_{f=1}^{N_f} a^4 \sum_{x,y \in \Lambda} \bar{\psi}^f(x) \left[\left(m^f + \frac{4}{a} \right) \delta_{x,y} \right. \\ &\quad \left. - \frac{1}{2a} \sum_{\mu=1}^4 [(\mathbf{1} - \gamma_\mu)U_\mu(x)\delta_{x+\hat{\mu},y} + (\mathbf{1} + \gamma_\mu)U_{-\mu}(x)\delta_{x,y+\hat{\mu}}] \right] \psi^f(y). \end{aligned} \quad (2.20)$$

2.3. General idea and purpose of the effective theory

Even in the limit of massless quarks, however, the Wilson term breaks chiral symmetry explicitly. Introducing the hopping parameter $\kappa^f = (2am^f + 8)^{-1}$, one can use the freedom of field normalisation and bring the lattice action to a particularly simple form by $a^2/\sqrt{2a\kappa^f}\psi^f(x) \rightarrow \psi^f(x)$:

$$S_{F,W}[\psi, \bar{\psi}, U] = \sum_{f=1}^{N_f} \sum_{x,y \in \Lambda} \bar{\psi}^f(x) Q^f(x,y) \psi^f(x), \quad Q^f(x,y) = \mathbf{1} - \kappa^f H(x,y), \quad (2.21)$$

$$H(x,y) = \sum_{\mu=1}^4 [(\mathbf{1} - \gamma_\mu) U_\mu(x) \delta_{x+\hat{\mu},y} + (\mathbf{1} + \gamma_\mu) U_{-\mu}(x) \delta_{x,y+\hat{\mu}}], \quad (2.22)$$

where Q^f is the Dirac operator and H the hopping matrix.

While the link variables eq. (2.17) are SU(3)-matrices, the fermion fields are formulated in terms of anticommuting numbers, so-called Grassmann numbers. In QCD, the path integral for the fermions is Gaussian (cf. eqs. (2.11) and (2.21)), making it possible to integrate them out analytically [3]:

$$\int d\eta_1^\dagger d\eta_1 \cdots d\eta_N^\dagger d\eta_N \exp\left(-\sum_{i,j} \eta_j^\dagger Q_{ji} \eta_i\right) = \det Q. \quad (2.23)$$

With this so-called fermion or quark determinant, one is left with a path integral just in terms of integrals over gauge fields:

$$Z_{\text{LQCD}} = \int [dU] \prod_{f=1}^{N_f} \det(Q^f[U]) e^{-S_G[U]}, \quad (2.24)$$

$$\int [dU] = \prod_{x \in \Lambda} \prod_{\mu=1}^4 dU_\mu(x). \quad (2.25)$$

In these formulae, the individual measures for the integration over the link variables $dU_\mu(x)$ are taken to be the invariant group measure or Haar measure [4].

Implementing the chemical potential by simply adding a term $\mu^f \gamma_4 \delta_{x,y}$ to the Dirac operator $Q^f(x,y)$ as in eq. (2.12) leads to an energy density which is divergent in the continuum limit [4]. One therefore replaces the hopping term in eq. (2.22) with

$$H^f(x,y) = e^{a\mu^f} (\mathbf{1} - \gamma_4) U_4(x) \delta_{x+\hat{4},y} + e^{-a\mu^f} (\mathbf{1} + \gamma_4) U_4^\dagger(x - \hat{4}) \delta_{x,y+\hat{4}} + \sum_{i=1}^3 [(\mathbf{1} - \gamma_i) U_i(x) \delta_{x+\hat{i},y} + (\mathbf{1} + \gamma_i) U_i^\dagger(x - \hat{i}) \delta_{x,y+\hat{i}}]. \quad (2.26)$$

The introduction of the chemical potential comes with a serious technical drawback: For $a\mu \neq 0$ the Dirac operator is no longer γ_5 -hermitian. Consequently, a non-vanishing real μ creates a particle-antiparticle asymmetry, which renders the determinant of the Dirac operator complex [4]. A straightforward application of importance sampling is hence impossible: the infamous sign problem.

2.3. General idea and purpose of the effective theory

The purpose of the effective theory is to reproduce the main characteristics of Lattice QCD in a relevant parameter region, whilst providing a simplification of the numerical and analytical

2. An effective theory for (Lattice) QCD

properties. It still suffers from the aforementioned sign problem at finite chemical potential, but this gets less severe in the sense that it can be treated, for example, by sign reweighting. Moreover, the effective theory reduces the numerical effort, especially for the computation of the fermion determinant, substantially and makes the theory also accessible to analytical studies [7]. Besides, the effective theory can be improved systematically. As we will later see, it converges at a finite order in the hopping parameter (cf. eq. (2.56)) and reduces the degrees of freedom to Polyakov loops (cf. section 2.8).

The starting point for the derivation of the effective theory is full Wilson Lattice QCD in $3+1$ dimensions, see eq. (2.24). It basically consists of two combined expansion: The first one is a strong coupling expansion around the limit $\beta \rightarrow 0$ for the gauge action (cf. section 2.4). The fermion determinant is expanded around the limit $\kappa \rightarrow 0$ with a hopping parameter expansion (cf. section 2.5). These steps allow us to perform the gauge integration over the spatial links analytically. The effective action S_{eff} then solely depends on the temporal links:

$$Z_{\text{eff}} = \int [dU_4] e^{-S_{\text{eff}}}, \quad -S_{\text{eff}} = \ln \int [dU_i] \prod_{f=1}^{N_f} \det(Q^f[U]) e^{-S_G[U]}. \quad (2.27)$$

This permits to change the integration measure to Polyakov loops, which are traces over closed loops of link variables in temporal direction:

$$\int [dU_4] \rightarrow \int [dL], \quad L_{\mathbf{x}} = \text{tr } W_{\mathbf{x}} = \text{tr} \prod_{\tau=0}^{N_\tau-1} U_4(\mathbf{x}, \tau). \quad (2.28)$$

As with the plaquette, the Polyakov loop as a closed loop is a gauge invariant observable. The final stage of the derivation is to evaluate the sum over the temporal positions, which stems from the determinant over the temporal space in $\det Q^f$. This leads to a dimensional reduction, so that the resulting theory is only three-dimensional and has a significantly reduced number of degrees of freedom: N_s^3 complex numbers $L_{\mathbf{x}}$, compared to $4N_s^3 N_\tau$ $\text{SU}(3)$ -matrices $U_\mu(x)$ in full Lattice QCD.

2.4. The strong coupling expansion

We will start our discussion with the expansion of the pure gauge action. As this thesis does not aim to provide any further improvements on the results in this part of the action, we will only briefly review them. For a more detailed presentation of the derivation the reader may refer to [7, 8].

By making use of the character expansion, the effective action of pure Yang-Mills theory can be written as

$$-S_{\text{eff}}^G = \ln \int [dU_i] \prod_p \left[1 + \sum_{r \neq 0} d_r a_r(\beta) \chi_r(U_p) \right]. \quad (2.29)$$

Here, the sum runs over all non-trivial irreducible representations r of $\text{SU}(3)$ with dimension d_r and character χ_r . The a_r are the corresponding expansion coefficients. The coefficient of the trivial character has been factored out and neglected, as it only gives a constant contribution to the action. Terms which do not wind through the temporal boundary of the lattice will become independent of the temporal link variables after the spatial link integration. Therefore, such terms also give constant contributions and cancel when calculating expectation values.

The leading-order contribution then comes from chains of plaquettes looping through the temporal boundary, if plaquettes which do not contain any temporal links are neglected. The group integration over the spatial links enforces all plaquettes of a graph to belong to the same representation:

$$-S_{\text{eff,NN}}^G = \ln \prod_{\langle \mathbf{x}\mathbf{y} \rangle} \left[1 + \sum_{r \neq 0} [a_r(\beta)]^{N_\tau} \chi_r(W_{\mathbf{x}}) \chi_r(W_{\mathbf{y}}^\dagger) \right]. \quad (2.30)$$

One is hence left with an interaction between nearest neighbour sites $\langle \mathbf{x}\mathbf{y} \rangle$ on the spatial lattice in all representations, including the corresponding conjugate representations, if they are inequivalent [9].

The leading-order contribution is given by the fundamental and anti-fundamental representations with the expansion parameter $a_f = u$ and the effective coupling $\lambda_1 = u^{N_\tau} + \mathcal{O}(u^{N_\tau+4})$:

$$-S_{\text{eff,1}}^G = \sum_{\langle \mathbf{x}\mathbf{y} \rangle} \ln[1 + \lambda_1(L_{\mathbf{x}}^* L_{\mathbf{y}} + L_{\mathbf{x}} L_{\mathbf{y}}^*)]. \quad (2.31)$$

Higher-order contributions to the strong coupling series for λ_1 stem from the inclusion of additional spatial plaquettes and are collected in appendix A.1.

The next contribution comes from the term in eq. (2.30) where r is the adjoint representation, starting at order u^{2N_τ} :

$$-S_{\text{eff},a}^G = \sum_{\langle \mathbf{x}\mathbf{y} \rangle} \ln[1 + \lambda_a(\chi_a(W_{\mathbf{x}}) \chi_a(W_{\mathbf{y}}))]. \quad (2.32)$$

The adjoint representation is its own conjugate and has the character $\chi_a(U) = \text{tr} U \text{tr} U^\dagger - 1$ [9], which implies for our case $\chi_a(W_{\mathbf{x}}) = |L_{\mathbf{x}}|^2 - 1$.

Other higher-order terms are obtained from the interaction between Polyakov loops at distances larger than one. As the planar graph with Polyakov loops at distance $2a$ is cancelled by the contribution of the nearest-neighbour graph squared [8], the leading non-zero contribution comes from L-shaped graphs with diagonal distance $\sqrt{2}a$, abbreviated by $[\mathbf{x}\mathbf{y}]$:

$$-S_{\text{eff},2}^G = \sum_{[\mathbf{x}\mathbf{y}]} \ln[1 + \lambda_2(L_{\mathbf{x}} L_{\mathbf{y}}^* + L_{\mathbf{x}}^* L_{\mathbf{y}})], \quad (2.33)$$

where $\lambda_2 = u^{2N_\tau+2} + \mathcal{O}(u^{2N_\tau+4})$. The strong coupling series expansions for λ_a and λ_2 including contributions of spatial detours can again be found in appendix A.1.

2.5. The hopping parameter expansion

We will now proceed with the hopping parameter expansion of the quark determinant in the strong coupling limit $\beta = 0$. Section 2.6 will then discuss the corrections that arise to the fermionic action when one moves away from this limit by including mixing terms.

From eq. (2.26) it is clear that the hopping matrix can be separated into temporal and spatial parts:

$$H(x, y) = \underbrace{T_{x,y}^+ + T_{x,y}^-}_{=T_{x,y}} + \sum_{i=1}^3 \underbrace{(S_{x,y,i}^+ + S_{x,y,i}^-)}_{=S_{x,y,i}}. \quad (2.34)$$

2. An effective theory for (Lattice) QCD

The respective hopping terms are

$$T_{x,y}^+ = e^{a\mu}(\mathbb{1} - \gamma_4)U_4(x)\delta_{x+\hat{4},y}, \quad (2.35)$$

$$T_{x,y}^- = e^{-a\mu}(\mathbb{1} + \gamma_4)U_4^\dagger(x - \hat{4})\delta_{x,y+\hat{4}}, \quad (2.36)$$

$$S_{x,y,i}^+ = (\mathbb{1} - \gamma_i)U_i(x)\delta_{x+\hat{i},y}, \quad (2.37)$$

$$S_{x,y,i}^- = (\mathbb{1} + \gamma_i)U_i^\dagger(x - \hat{i})\delta_{x,y+\hat{i}}. \quad (2.38)$$

From now on, we will only consider degenerate quarks in N_f flavours. Therefore, we can drop the index f , since in this case $\prod_{i=1}^{N_f} \det Q^f = \det Q^{N_f}$. Splitting the hopping matrix as in eq. (2.34) then permits to divide the fermion determinant into temporal and spatial hopping terms:

$$\det_{c,d,s,t} Q^{N_f} = \det_{c,d,s,t} (\mathbb{1} - \kappa T - \kappa S)^{N_f} = \det_{c,d,s,t} (\mathbb{1} - \kappa S (\mathbb{1} - \kappa T)^{-1})^{N_f} \det_{c,d,s,t} (\mathbb{1} - \kappa T)^{N_f}. \quad (2.39)$$

Here, indices c , d , s and t have been introduced to indicate that the determinant is over colour, Dirac, spatial and temporal space. In the limit of static – that is infinitely heavy – quarks, only temporal hops will contribute. Hence, the second determinant in eq. (2.39) is called static determinant, while the corrections arising from spatial hops are contained in the first, kinetic determinant.

2.5.1. The static quark determinant

The Dirac deltas in the definition of T imply that only closed quark lines give a non-vanishing contribution. In the static limit, the only possibility to form such a closed quark line is by looping around the lattice through the temporal boundary. This is equivalent to a temporal Wilson line or untraced Polyakov loop (cf. eq. (2.28)). It also shows that in the static limit, which corresponds to $\kappa \rightarrow 0$, the system prefers a situation where the smallest possible power of κ appears. Calculating the Dirac, spatial and temporal determinants, one ends up with [7]

$$\det_{c,d,s,t} (\mathbb{1} - \kappa T) = \prod_{\mathbf{x}} \det_c \left[\mathbb{1} + (2\kappa e^{a\mu})^{N_\tau} W_{\mathbf{x}} \right]^2 \det_c \left[\mathbb{1} + (2\kappa e^{-a\mu})^{N_\tau} W_{\mathbf{x}}^\dagger \right]^2. \quad (2.40)$$

By defining the effective couplings for static quarks and antiquarks,

$$h_1 = (2\kappa e^{a\mu})^{N_\tau} = \exp[N_\tau(a\mu + \ln(2\kappa))], \quad (2.41)$$

$$\bar{h}_1 = (2\kappa e^{-a\mu})^{N_\tau} = \exp[N_\tau(-a\mu + \ln(2\kappa))], \quad (2.42)$$

and using the relation (A.32) for the determinant involving an SU(3)-matrix, one arrives at the final expression for the static quark determinant:

$$\det_{c,d,s,t} (\mathbb{1} - \kappa T) = \prod_{\mathbf{x}} (1 + h_1 L_{\mathbf{x}} + h_1^2 L_{\mathbf{x}}^\dagger + h_1^3)^2 (1 + \bar{h}_1 L_{\mathbf{x}}^\dagger + \bar{h}_1^2 L_{\mathbf{x}} + \bar{h}_1^3)^2. \quad (2.43)$$

The integration over the spatial links is trivial for the static determinant, as those have been neglected.

2.5.2. The kinetic quark determinant: general approach

The static determinant corresponds to the leading term in the spatial hopping expansion of the full fermion determinant. Continuing the calculation in eq. (2.39), employing the well-known identity [4]

$$\det e^A = e^{\text{tr} A}, \quad (2.44)$$

which holds for any complex square matrix $A \in \mathbb{C}^{n \times n}$, $n \in \mathbb{N}$, and expanding the logarithm, one obtains:

$$\det_{c,d,s,t} Q^{N_f} = \exp \left[-N_f \sum_{k=1}^{\infty} \frac{\kappa^k}{k} \text{tr}_{c,d,s,t} \left(\left(S(\mathbb{1} - \kappa T)^{-1} \right)^k \right) \right] \det_{c,d,s,t} (\mathbb{1} - \kappa T)^{N_f}. \quad (2.45)$$

The static propagator

Before proceeding with the expansion of the kinetic quark determinant, the static propagator $(\mathbb{1} - \kappa T)^{-1}$ has to be computed. Since $(\mathbb{1} + \gamma_\mu)(\mathbb{1} - \gamma_\mu) = 0$, graphs involving backtracking, i. e. 180° turns, give no contribution. Hence, hops in forward and backward time direction do not mix:

$$(\mathbb{1} - \kappa T_{x,y})^{-1} = (\mathbb{1} - \kappa T_{x,y}^+)^{-1} + (\mathbb{1} - \kappa T_{x,y}^-)^{-1} - \mathbb{1}. \quad (2.46)$$

The static propagator describes quarks moving only in temporal direction; no spatial propagation is involved. For this reason, one may fix $\mathbf{x} = \mathbf{y}$. The static propagator can furthermore be split up in spin space according to

$$(\mathbb{1} - \kappa T_{x,y})^{-1} = A_{x,y}^+ + \gamma_4 B_{x,y}^+ + A_{x,y}^- - \gamma_4 B_{x,y}^-. \quad (2.47)$$

The respective terms read [10]:

$$\begin{aligned} A_{x,y}^+ &= \frac{1}{2} \left[\mathbb{1} - \frac{h_1 W_{\mathbf{x}}}{\mathbb{1} + h_1 W_{\mathbf{x}}} \right] \delta_{x,y} + \frac{1}{2} h_1^{\frac{\tau_y - \tau_x}{N_\tau}} \frac{W_{\mathbf{x}}(\tau_x, \tau_y)}{\mathbb{1} + h_1 W_{\mathbf{x}}} [\Theta(\tau_y - \tau_x) - h_1 \Theta(\tau_x - \tau_y)] \delta_{\mathbf{x},\mathbf{y}}, \\ B_{x,y}^+ &= -\frac{1}{2} \frac{h_1 W_{\mathbf{x}}}{\mathbb{1} + h_1 W_{\mathbf{x}}} \delta_{x,y} + \frac{1}{2} h_1^{\frac{\tau_y - \tau_x}{N_\tau}} \frac{W_{\mathbf{x}}(\tau_x, \tau_y)}{\mathbb{1} + h_1 W_{\mathbf{x}}} [\Theta(\tau_y - \tau_x) - h_1 \Theta(\tau_x - \tau_y)] \delta_{\mathbf{x},\mathbf{y}}, \\ A_{x,y}^- &= \frac{1}{2} \left[\mathbb{1} - \frac{\bar{h}_1 W_{\mathbf{x}}^\dagger}{\mathbb{1} + \bar{h}_1 W_{\mathbf{x}}^\dagger} \right] \delta_{x,y} + \frac{1}{2} \bar{h}_1^{\frac{\tau_x - \tau_y}{N_\tau}} \frac{W_{\mathbf{x}}^\dagger(\tau_x, \tau_y)}{\mathbb{1} + \bar{h}_1 W_{\mathbf{x}}^\dagger} [\Theta(\tau_x - \tau_y) - \bar{h}_1 \Theta(\tau_y - \tau_x)] \delta_{\mathbf{x},\mathbf{y}}, \\ B_{x,y}^- &= -\frac{1}{2} \frac{\bar{h}_1 W_{\mathbf{x}}^\dagger}{\mathbb{1} + \bar{h}_1 W_{\mathbf{x}}^\dagger} \delta_{x,y} + \frac{1}{2} \bar{h}_1^{\frac{\tau_x - \tau_y}{N_\tau}} \frac{W_{\mathbf{x}}^\dagger(\tau_x, \tau_y)}{\mathbb{1} + \bar{h}_1 W_{\mathbf{x}}^\dagger} [\Theta(\tau_x - \tau_y) - \bar{h}_1 \Theta(\tau_y - \tau_x)] \delta_{\mathbf{x},\mathbf{y}}. \end{aligned} \quad (2.48)$$

Here, $W_{\mathbf{x}}(\tau_x, \tau_y)$ denotes a temporal Wilson line going from τ_x to τ_y in positive temporal direction (cf. fig. 2.3):

$$W_{\mathbf{x}}(\tau_x, \tau_y) = \begin{cases} \prod_{\tau=\tau_x}^{\tau_y-1} U_4(\mathbf{x}, \tau), & \tau_x < \tau_y \\ \prod_{\tau=\tau_x}^{N_\tau-1} U_4(\mathbf{x}, \tau) \cdot \prod_{\tau=0}^{\tau_y-1} U_4(\mathbf{x}, \tau), & \tau_x > \tau_y \\ \prod_{\tau=0}^{N_\tau-1} U_4(\mathbf{x}, \tau) = W_{\mathbf{x}}, & \tau_x = \tau_y \end{cases} \quad (2.49)$$

$W_{\mathbf{x}}^\dagger(\tau_x, \tau_y)$ by contrast connects the time slices τ_x and τ_y in negative temporal direction:

$$W_{\mathbf{x}}^\dagger(\tau_x, \tau_y) = \begin{cases} \left(\prod_{\tau=\tau_y}^{N_\tau-1} U_4(\mathbf{x}, \tau) \cdot \prod_{\tau=0}^{\tau_x-1} U_4(\mathbf{x}, \tau) \right)^\dagger, & \tau_x < \tau_y \\ \left(\prod_{\tau=\tau_y}^{\tau_x-1} U_4(\mathbf{x}, \tau) \right)^\dagger, & \tau_x > \tau_y \\ \left(\prod_{\tau=0}^{N_\tau-1} U_4(\mathbf{x}, \tau) \right)^\dagger = W_{\mathbf{x}}^\dagger, & \tau_x = \tau_y \end{cases} \quad (2.50)$$

For the Heaviside step function, the convention $\Theta(0) = 0$ is used.

2. An effective theory for (Lattice) QCD

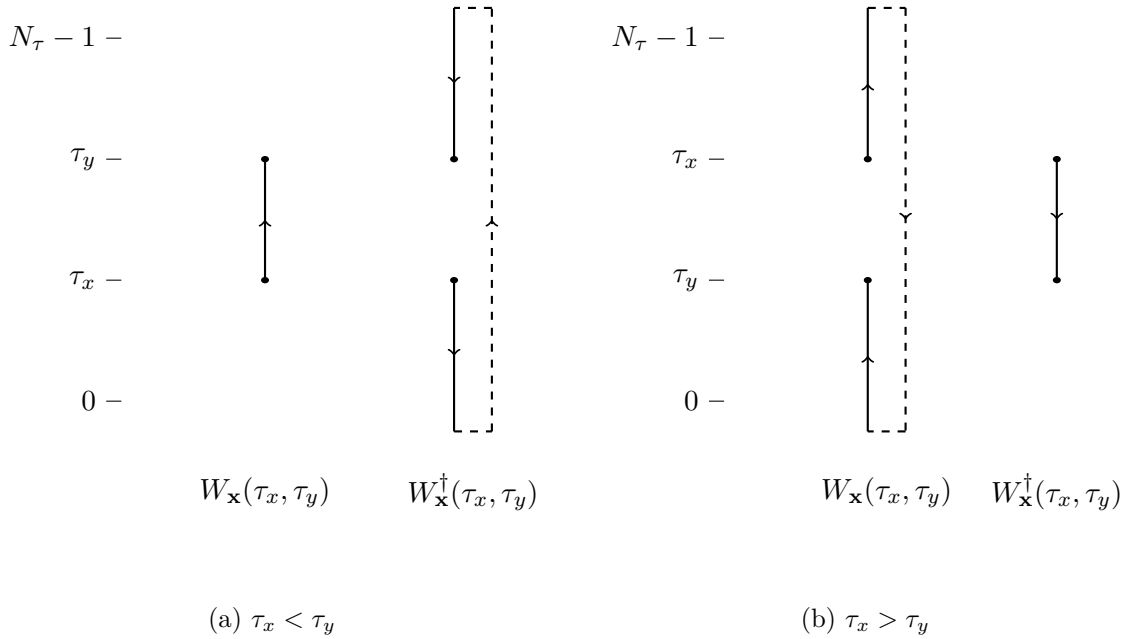


Figure 2.3.: Illustration of the fractional Wilson lines eqs. (2.49) and (2.50) which appear in the static propagator. $W_{\mathbf{x}}$ always describes propagation in positive time direction, $W_{\mathbf{x}}^\dagger$ in negative time direction. Earlier time slices can be reached by crossing the antiperiodic boundaries of the lattice

The loop matrices

As already mentioned, only closed quark lines give a non-vanishing contribution to the fermion determinant. Therefore, it is possible to write eq. (2.45) in terms of a product of smaller determinants of loop matrices $\tilde{M}_{C_{s_0}}$. Here, C_{s_0} describes a closed spatial path of length s_0 . The loop matrices $\tilde{M}_{C_{s_0}}$ are given by the ordered product of the matrices $S(\mathbf{1} - \kappa T)^{-1}$ along that path [11]:

$$\tilde{M}_{C_{s_0}} = \prod_{\substack{i=0 \\ \mathbf{x}_i \in C_{s_0}}}^{s_0-1} S_{\mathbf{x}_i, \mathbf{x}_{(i+1) \bmod s_0}} (\mathbf{1} - \kappa T)_{\mathbf{x}_{(i+1) \bmod s_0}}^{-1}. \quad (2.51)$$

In this expression, colour, Dirac and time indices have been suppressed to shorten the notation. Likewise, the second spatial index on the static propagator has been omitted, because it is diagonal in space. Graphically, a particular matrix element of $\tilde{M}_{C_{s_0}}$ with time indices τ_s and τ_e corresponds to the sum over all possible ways to draw a quark world-line connecting (\mathbf{x}_0, τ_s) and (\mathbf{x}_0, τ_e) by winding exactly once around the spatial loop C_{s_0} . This process is built up of alternating spatial hops S and temporal (static) propagations $(\mathbf{1} - \kappa T)^{-1}$.

As one such loop matrix $\tilde{M}_{C_{s_0}}$ already corresponds to s_0 powers of $S(\mathbf{1} - \kappa T)^{-1}$, one may set $k = s_0 n$ in eq. (2.45). An additional prefactor of s_0 arises from the fact that $\text{tr} \left((S(\mathbf{1} - \kappa T)^{-1})^k \right)$

contains $\text{tr} \left(\tilde{M}_{C_{s_0}}^n \right)$ s_0 times (once for each base point of the spatial loop):

$$\begin{aligned}
 \det_{c,d,s,t} Q^{N_f} &= \exp \left[-N_f \sum_{s_0} \sum_{\{C_{s_0}\}} \sum_{n=1}^{\infty} \frac{(\kappa^{s_0})^n}{n} \text{tr}_{c,d,t} \left(\tilde{M}_{C_{s_0}}^n \right) \right] \det_{c,d,s,t} (\mathbb{1} - \kappa T)^{N_f} \\
 &= \exp \left[N_f \sum_{s_0} \sum_{\{C_{s_0}\}} \text{tr}_{c,d,t} \left(\ln \left(\mathbb{1} - \kappa^{s_0} \tilde{M}_{C_{s_0}} \right) \right) \right] \det_{c,d,s,t} (\mathbb{1} - \kappa T)^{N_f} \\
 &= \left(\prod_{s_0} \prod_{\{C_{s_0}\}} \det_{c,d,t} \left(\mathbb{1} - \kappa^{s_0} \tilde{M}_{C_{s_0}} \right)^{N_f} \right) \det_{c,d,s,t} (\mathbb{1} - \kappa T)^{N_f}. \tag{2.52}
 \end{aligned}$$

With this so-called spatial loop expansion one has an expansion of the kinetic quark determinant in terms of the interaction range. By restricting the product over s_0 in eq. (2.52) to a finite number of factors, one still gets the full interactions between the involved sites. This is in contrast to a direct spatial hopping expansion in powers of κ as in [7], where each term contains only an approximated version of different interactions which contribute up to the specified order. Nevertheless, the derivation of the effective theory is equally complicated in both formalisms.

Expansion in terms of traces

To obtain explicit expressions for the different interaction terms, it is also in our approach necessary to expand the corresponding determinants from eq. (2.52) in terms of traces. This is due to the fact that the group integrals over the spatial links cannot be carried out if those links are in the exponent. One possible method is to use again the relation (2.44) and carry out a trace-log expansion:

$$\begin{aligned}
 \det_{c,d,t} \left(\mathbb{1} - \kappa^{s_0} \tilde{M}_{C_{s_0}} \right)^{N_f} &= \exp \left[N_f \text{tr}_{c,d,t} \left(\ln \left(\mathbb{1} - \kappa^{s_0} \tilde{M}_{C_{s_0}} \right) \right) \right] \\
 &= \exp \left[-N_f \sum_{k=1}^{\infty} \frac{(\kappa^{s_0})^k}{k} \text{tr}_{c,d,t} \left(\tilde{M}_{C_{s_0}}^k \right) \right] \\
 &= \prod_{k=1}^{\infty} \exp \left[-N_f \frac{(\kappa^{s_0})^k}{k} \text{tr}_{c,d,t} \left(\tilde{M}_{C_{s_0}}^k \right) \right] \\
 &= \prod_{k=1}^{\infty} \sum_{n_k=0}^{\infty} \frac{N_f^{n_k}}{n_k!} \left[-\frac{(\kappa^{s_0})^k}{k} \text{tr}_{c,d,t} \left(\tilde{M}_{C_{s_0}}^k \right) \right]^{n_k}. \tag{2.53}
 \end{aligned}$$

From here, one has to figure out which combinations of k and n_k contribute up to the desired order in κ , calculate the corresponding prefactors and collect the terms by their power of κ .

An alternative approach may be pursued in order to obtain all the relevant trace terms and their prefactors in a more systematic fashion. To that end, one can express the determinant on the left-hand side of eq. (2.53) in terms of the characteristic polynomial of $\tilde{M}_{C_{s_0}}$.

The characteristic polynomial of a square matrix $A \in \mathbb{C}^{n \times n}$, $n \in \mathbb{N}$ is defined as

$$\chi_A(\lambda) = \det(\mathbb{1}\lambda - A) = \sum_{k=0}^n \lambda^k c_k(A). \tag{2.54}$$

It is a polynomial in λ whose degree is given by the dimension of the matrix A . Its coefficients $c_k(A)$ are all polynomial expressions in the entries of the matrix and can be obtained from the

2. An effective theory for (Lattice) QCD

recursive LeVerrier-Fadeev algorithm. For this purpose, one starts with a matrix $B_0(A) = 0$ and the constant $c_n(A) = 1$ and then determines the remaining coefficients from the top down [11]:

$$B_k(A) = AB_{k-1}(A) + c_{n-k+1}(A)\mathbb{1}, \quad c_{n-k}(A) = -\frac{1}{k} \text{tr}(AB_k(A)), \quad k = 1, \dots, n. \quad (2.55)$$

Since the loop matrices $\tilde{M}_{C_{s_0}}$ are matrices in colour, Dirac and temporal space, their dimension is $\dim(\tilde{M}_{C_{s_0}}) = N_c N_d N_\tau = 12N_\tau$, and the application of the method explained above yields

$$\begin{aligned} \det_{c,d,t}(\mathbb{1} - \kappa^{s_0} \tilde{M}_{C_{s_0}}) &= \kappa^{12s_0 N_\tau} \det_{c,d,t}(\mathbb{1} \kappa^{-s_0} - \tilde{M}_{C_{s_0}}) = \kappa^{12s_0 N_\tau} \chi_{\tilde{M}_{C_{s_0}}}(\kappa^{-s_0}) \\ &= \kappa^{12s_0 N_\tau} \sum_{k=0}^{12N_\tau} \kappa^{-s_0 k} c_k(\tilde{M}_{C_{s_0}}) = \sum_{k=0}^{12N_\tau} \kappa^{s_0(12N_\tau - k)} c_k(\tilde{M}_{C_{s_0}}) \\ &= \sum_{k=0}^{12N_\tau} \kappa^{s_0 k} c_{12N_\tau - k}(\tilde{M}_{C_{s_0}}). \end{aligned} \quad (2.56)$$

For multiple flavours, this whole expression has to be taken to the power of N_f , so that the series terminates at $\mathcal{O}(\kappa^{12s_0 N_\tau N_f})$ for the fermion interaction at distance s_0 . This is one of the major advantages of writing the determinant in terms of the characteristic polynomial instead of performing a trace-log expansion: It is apparent that the series only has a finite number of terms. The flavour dependence, on the other hand, is more obvious in the form (2.53): Up to $\mathcal{O}(\kappa^n)$ with $n \leq 12s_0 N_\tau$ it can be included by multiplying each term by $N_f^{\#\text{tr}}$, where $\#\text{tr}$ is the number of traces appearing in the corresponding term. From the perspective of eq. (2.56), this follows from expanding the N_f -th power of the sum by using the multinomial theorem, collecting the terms by their power of κ and plugging in the coefficients of the characteristic polynomial.

The Dirac trace

By means of one of these expansions, the kinetic quark determinant for a specific interaction range s_0 can be expressed in terms of powers of traces over powers of the corresponding loop matrix, i. e. $[\text{tr}(\tilde{M}_{C_{s_0}}^k)]^{n_k}$. Here, the necessary values of k and n_k are determined by the order in κ sought. According to eq. (2.51), the ingredients for these expressions are the spatial hopping matrices S from eqs. (2.37) and (2.38) and the static quark propagator from eq. (2.47). From these relations, the Dirac structure of the terms is evident, so that the calculation of the Dirac trace becomes an easy task. Alternatively, by implementing the basic relations obeyed by the Dirac matrices, the computation can be automated. This has been realised with **Mathematica** in the context of the thesis at hand. The result then consists of traces over colour and temporal space of products of spatial links U_i and A s and B s from eq. (2.48).

Integration over spatial links

The next step of the programme outlined in section 2.3 is the integration over the spatial links. The procedure from the previous steps leaves integrals over products of entries U_{IJ} of group elements U in the fundamental representation,

$$\int_{\text{SU}(N_c)} dU \prod_{\alpha=1}^a U_{I_\alpha, J_\alpha} \prod_{\beta=1}^b U_{K_\beta, L_\beta}^\dagger, \quad (2.57)$$

as the most general form of gauge integrals which have to be evaluated. This type of integral is non-zero if and only if $a = b \pmod{N_c}$ [12]. As the spatial links $U_i(\mathbf{x}, x_4)$ appearing in our equations are in general situated at different spatial and temporal positions (\mathbf{x}, x_4) and point into different directions i , this gives a strong constraint on their allowed combinations.

The geometry of the terms is determined by the spatial positions \mathbf{x} and directions i of these links. Therefore, it is natural to sort the terms by these two indices and aim to fulfil the restriction imposed by the gauge integration with the temporal indices. To do so, one splits the temporal sums into all combinations of mutually equal temporal coordinates which yield a non-vanishing contribution after gauge integration. Physically, this can be interpreted as quarks hopping to and fro the different (spatial) lattice sites involved. Because the Haar measure projects out the contribution of the integrand to the trivial representation of the group [4], only colour-neutral combinations are permitted for these particle configurations, i. e. mesons and baryons.

The general procedure for computing the integrals eq. (2.57), as well as the results for the gauge group $SU(3)$ and $a, b \leq 3$, can be found in appendix A.2. Qualitatively, mesonic contributions yield Kronecker δ s, which will give traces of A and B after contraction of the colour indices, whereas baryonic contributions yield Levi-Civita ϵ s, which will give determinants of A and B . Hence, after the gauge integration, the kinetic determinant can be expressed in terms of traces and determinants of A and B .

For the calculation of the effective action, all the resulting expressions have to be summed over the spatial position \mathbf{x} (in eq. (2.52), this is contained in the product over all spatial loops, $\prod_{\{C_{s_0}\}}$). This induces some further simplifications: All terms that transform into each other under the interchange of two lattice sites, for example $\mathbf{x} \leftrightarrow \mathbf{x} + \hat{i}$, give the same result.

Evaluation of the temporal sums

The final step of the derivation is to evaluate the sum over the temporal positions explicitly. This leaves a sum only over the spatial positions, making the action three-dimensional. Equation (2.48) reveals that A and B have a part which is diagonal in temporal space as well as an off-diagonal part. While the diagonal part is independent of the temporal coordinate, there is such a dependence for the off-diagonal part, that additionally differs depending on which of the two temporal indices is the greater one. Consequently, one has to split the sum into all possible arrangements of the temporal coordinates. For the $\mathcal{O}(\kappa^4)$ -correction, for example, the spatial link integration leaves maximally two unequal temporal coordinates, so that the sum has to be split according to $\sum_{\tau_1 \neq \tau_2} = \sum_{\tau_1 < \tau_2} + \sum_{\tau_1 > \tau_2}$. It turns out that the outcome of the summation only depends on the number of descents in the permutation $(\tau_1, \tau_2, \dots, \tau_k, \tau_1)$, not on the precise arrangement (cf. section 4.4). For the example above this means that the result will be the same for both cases, since there is always exactly one descent. Therefore, the splitting of the temporal sums induces no further multiplication of terms here.

From this point, one has to plug in the corresponding parts of A and B from eq. (2.48), expand the occurring powers and figure out the products of the fractional Wilson lines. In the end, only whole Wilson lines will be left, ensuring gauge invariance. The remaining degrees of

2. An effective theory for (Lattice) QCD

freedom are then trace over Wilson line constructs of the form

$$W_{n_1 m_1 n_2 m_2}(\mathbf{x}) = \text{tr}_c \left(\frac{(h_1 W_{\mathbf{x}})^{m_1}}{(\mathbf{1} + h_1 W_{\mathbf{x}})^{n_1}} \frac{(\bar{h}_1 W_{\mathbf{x}}^\dagger)^{m_2}}{(\mathbf{1} + \bar{h}_1 W_{\mathbf{x}}^\dagger)^{n_2}} \right), \quad (2.58)$$

$$W_{n_1 m_1 n_2 m_2}^\pm(\mathbf{x}) = W_{n_1 m_1 00}(\mathbf{x}) \pm W_{00 n_2 m_2}(\mathbf{x}), \quad (2.59)$$

where the shortened notation from [13] has been introduced.

2.5.3. The kinetic quark determinant: results for the leading and next-to-leading order

Now that the general strategy for the derivation of the kinetic quark determinant is known, it can be applied to obtain concrete results for the leading and next-to-leading order. To $\mathcal{O}(\kappa^2)$, the only contribution comes from $s_0 = 2$, which corresponds to a two-point (nearest-neighbour) interaction. To $\mathcal{O}(\kappa^4)$, also $s_0 = 4$ has to be included, which describes three- and four-point interactions. Moreover, two separate spatial loops \tilde{M}_{C_2} can be considered, yielding additional, disconnected three- and four-point interactions, depending on whether the loops share one spatial point or none at all. The expansion in terms of traces (cf. eqs. (2.53) and (2.56)) gives:

$$\begin{aligned} \det_{c,d,t} \left(\mathbf{1} - \kappa^2 \tilde{M}_{C_2} \right)^{N_f} &= 1 - N_f \kappa^2 \text{tr}_{c,d,t} \left(\tilde{M}_{C_2} \right) + \frac{\kappa^4}{2} \left(N_f^2 \text{tr}_{c,d,t}^2 \left(\tilde{M}_{C_2} \right) - N_f \text{tr}_{c,d,t} \left(\tilde{M}_{C_2}^2 \right) \right) \\ &\quad + \mathcal{O}(\kappa^6), \end{aligned} \quad (2.60)$$

$$\det_{c,d,t} \left(\mathbf{1} - \kappa^4 \tilde{M}_{C_4} \right)^{N_f} = 1 - N_f \kappa^4 \text{tr}_{c,d,t} \left(\tilde{M}_{C_4} \right) + \mathcal{O}(\kappa^8). \quad (2.61)$$

As the relevant features of the general procedure have been explained in section 2.5.2 and the corrections up to $\mathcal{O}(\kappa^4)$ are already known from the literature [7, 10], no more detailed calculations will be shown here. Instead, the final results for all possible geometries are collected in appendix A.4.

2.6. Gauge corrections

So far, the strong coupling and hopping parameter expansions have been discussed in isolation. Moving away from the strong coupling limit, however, also introduces mixing terms. These are diagrams which contain gauge plaquettes as well as quark lines. Many of these new contributions reduce to graphs already present in the strong coupling limit after the spatial link integration. They can thus be absorbed into the respective coupling constants, which then also become power series in u . Such corrections have been calculated in [7], and since the present work does not expand on these results, they are only reported in appendix A.1. An entirely new contribution arises from the term $\text{tr} \left(\tilde{M}_{C_4} \right)$ when the spatial loop C_4 forms a square [7]. This graph has only singly occupied spatial links and therefore vanishes in the strong coupling limit as a result of the gauge integration. For finite values of β , by contrast, it becomes non-zero if one inserts a gauge plaquette inside the square. The result for this term is presented alongside the rest of the fermionic $\mathcal{O}(\kappa^4)$ -action in appendix A.4.

2.7. Resummation of the effective action

The fermion action we started with in eq. (2.45) was written in the exponential. The expansion of this exponential became necessary in order to be able to carry out the group integrals over the spatial links. For numerical as well as analytical studies of the effective theory, however, it is much more convenient to work with an action in the exponential. To this end, the effective fermion action derived so far needs to be resummed.

Taking a closer look at the $\mathcal{O}(\kappa^2)$ -term in eq. (A.33), one indeed finds suitable terms of $\mathcal{O}(\kappa^4)$ which enable a resummation:

$$\begin{aligned}
& 1 - 2N_f \frac{\kappa^2 N_\tau}{N_c} \sum_{\mathbf{x}, i} W_{1111}^-(\mathbf{x}) W_{1111}^-(\mathbf{x} + \hat{i}) \\
& + 2N_f^2 \frac{\kappa^4 N_\tau^2}{N_c^2} \sum_{\mathbf{x}, \mathbf{y}, i, j} W_{1111}^-(\mathbf{x}) W_{1111}^-(\mathbf{x} + \hat{i}) W_{1111}^-(\mathbf{y}) W_{1111}^-(\mathbf{y} + \hat{j}) + \mathcal{O}(\kappa^6) \\
& = \exp \left[-2N_f \frac{\kappa^2 N_\tau}{N_c} \sum_{\mathbf{x}, i} W_{1111}^-(\mathbf{x}) W_{1111}^-(\mathbf{x} + \hat{i}) + \mathcal{O}(\kappa^6) \right]. \tag{2.62}
\end{aligned}$$

This opportunity is due to the fact that above $\mathcal{O}(\kappa^4)$ -terms are disconnected in the sense that the two loops share no spatial links, and the gauge integrals factorise. Therefore, up to $\mathcal{O}(\kappa^4)$, all the results of eqs. (2.60) and (2.61) can be written in the exponential, if the term $2N_f^2 \kappa^4 N_\tau^2 / N_c^2 \sum_{\mathbf{x}, \mathbf{y}, i, j} W_{1111}^-(\mathbf{x}) W_{1111}^-(\mathbf{x} + \hat{i}) W_{1111}^-(\mathbf{y}) W_{1111}^-(\mathbf{y} + \hat{j})$ is left out. Similar to the approach in appendix A.4, this can be separated into its contributions to the different interaction ranges. For the three- and four-point interactions, eq. (A.38) and its counterpart will not be present any more after the resummation. For the two-point interaction, the situation is a little bit more complicated: The term from the exponential is $\propto N_\tau^2$, whereas the corresponding term in the unresummed $\mathcal{O}(\kappa^4)$ -action is $\propto N_\tau(N_\tau - 1)$ (cf. eq. (A.35)). Consequently, a counterterm has to be introduced in the exponential:

$$\begin{aligned}
& 1 - 2N_f \frac{\kappa^2 N_\tau}{N_c} \sum_{\mathbf{x}, i} W_{1111}^-(\mathbf{x}) W_{1111}^-(\mathbf{x} + \hat{i}) \\
& + 2N_f^2 \frac{\kappa^4 N_\tau^2}{N_c^2} \sum_{\mathbf{x}, \mathbf{y}, i, j} W_{1111}^-(\mathbf{x}) W_{1111}^-(\mathbf{x} + \hat{i}) W_{1111}^-(\mathbf{y}) W_{1111}^-(\mathbf{y} + \hat{j}) \\
& - 2N_f^2 \frac{\kappa^4 N_\tau}{N_c^2} \sum_{\mathbf{x}, i} \left(W_{1111}^-(\mathbf{x}) \right)^2 \left(W_{1111}^-(\mathbf{x} + \hat{i}) \right)^2 + \mathcal{O}(\kappa^6) \\
& = \exp \left[-2N_f \frac{\kappa^2 N_\tau}{N_c} \sum_{\mathbf{x}, i} W_{1111}^-(\mathbf{x}) W_{1111}^-(\mathbf{x} + \hat{i}) \right. \\
& \quad \left. - 2N_f^2 \frac{\kappa^4 N_\tau}{N_c^2} \sum_{\mathbf{x}, i} \left(W_{1111}^-(\mathbf{x}) \right)^2 \left(W_{1111}^-(\mathbf{x} + \hat{i}) \right)^2 + \mathcal{O}(\kappa^6) \right] \tag{2.63}
\end{aligned}$$

This resummation also improves the convergence of the effective theory, since it includes an infinite number of higher-order graphs [7]. Another resummation scheme, which is particular to the nearest-neighbour interaction, will be discussed in section 4.4.

2.8. Transformation to Polyakov loops

With the methods explained so far it is possible to derive the kinetic quark determinant in terms of trace over Wilson line constructs $W_{n_1 m_1 n_2 m_2}$. For further studying the effective theory, however, it is highly advantageous to express these quantities also in terms of Polyakov loops eq. (2.28), as it has already been shown for the effective gauge action (cf. eqs. (2.31) to (2.33)) and the static quark determinant eq. (2.43).

The first step in doing so is to bring the denominators inside the trace in eq. (2.58) to the numerator. For this purpose, observe that for a square matrix $A \in \mathbb{C}^{n \times n}$, $n \in \mathbb{N}$, it follows from the Cayley-Hamilton theorem [14] that

$$\chi_A(A) = \sum_{k=0}^n c_k(A) A^k = c_0(A) \mathbb{1} + \sum_{k=1}^n c_k(A) A^k = c_0(A) \mathbb{1} + AB_n(A) = 0 \quad (2.64)$$

$$\Rightarrow AB_n(A) = -c_0(A) \mathbb{1} = (-1)^{n-1} \det(A) \mathbb{1}, \quad (2.65)$$

where $B_n(A) = \sum_{k=1}^n c_k(A) A^{k-1}$ is the n -th auxiliary matrix from the LeVerrier-Fadeev algorithm (cf. eq. (2.55)). With the definition of the adjugate matrix [14],

$$A \operatorname{adj}(A) = \det(A) \mathbb{1} = \operatorname{adj}(A) A, \quad (2.66)$$

this implies that

$$\operatorname{adj}(A) = (-1)^{n-1} B_n(A) = (-1)^{n-1} \sum_{k=1}^n c_k(A) A^{k-1}. \quad (2.67)$$

Therefore, the inverses appearing in eq. (2.58) can be written as

$$\begin{aligned} (\mathbb{1} + h_1 W)^{-1} &= \frac{1}{\det_c(\mathbb{1} + h_1 W)} \operatorname{adj}(\mathbb{1} + h_1 W) \\ &= \frac{1}{\det_c(\mathbb{1} + h_1 W)} (-1)^{N_c-1} \sum_{i=0}^{N_c-1} c_{i+1}(\mathbb{1} + h_1 W) \cdot (\mathbb{1} + h_1 W)^i \\ &= \frac{1}{\det_c(\mathbb{1} + h_1 W)} (-1)^{N_c-1} \sum_{i=0}^{N_c-1} c_{i+1}(\mathbb{1} + h_1 W) \sum_{k=0}^i \binom{i}{k} (h_1 W)^k \\ &= \frac{1}{\det_c(\mathbb{1} + h_1 W)} (-1)^{N_c-1} \sum_{k=0}^{N_c-1} \left(\sum_{i=k}^{N_c-1} c_{i+1}(\mathbb{1} + h_1 W) \binom{i}{k} \right) (h_1 W)^k. \end{aligned} \quad (2.68)$$

Now, the coefficients of the characteristic polynomial of $\mathbb{1} + h_1 W$ must be transformed to the ones of the characteristic polynomial of W . The two polynomials are related by

$$\begin{aligned} \chi_{\mathbb{1}+h_1 W}(\lambda) &= \sum_{i=0}^{N_c} c_i(\mathbb{1} + h_1 W) \lambda^i = \det_c(\lambda \mathbb{1} - \mathbb{1} - h_1 W) = \det_c((\lambda - 1) \mathbb{1} - h_1 W) \\ &= h_1^{N_c} \det_c \left(\frac{\lambda - 1}{h_1} \mathbb{1} - W \right) = h_1^{N_c} \chi_W \left(\frac{\lambda - 1}{h_1} \right) = h_1^{N_c} \sum_{i=0}^{N_c} c_i(W) h_1^{-i} (\lambda - 1)^i \\ &= \sum_{i=0}^{N_c} c_i(W) h_1^{N_c-i} \sum_{k=0}^i \binom{i}{k} (-1)^{i-k} \lambda^k = \sum_{k=0}^{N_c} \sum_{i=k}^{N_c} \binom{i}{k} (-1)^{i-k} h_1^{N_c-i} c_i(W) \lambda^k. \end{aligned} \quad (2.69)$$

The relation between the corresponding coefficients is hence

$$c_k(\mathbb{1} + h_1 W) = \sum_{i=k}^{N_c} \binom{i}{k} (-1)^{i-k} h_1^{N_c-i} c_i(W). \quad (2.70)$$

Plugging this into eq. (2.68) and switching sums once again yields

$$\begin{aligned} (\mathbb{1} + h_1 W)^{-1} &= \frac{1}{\dots} (-1)^{N_c-1} \sum_{k=0}^{N_c-1} \left(\sum_{i=k}^{N_c-1} \binom{i}{k} \sum_{j=i+1}^{N_c} \binom{j}{i+1} (-1)^{j-i-1} h_1^{N_c-j} c_j(W) \right) (h_1 W)^k \\ &= \frac{1}{\dots} (-1)^{N_c-1} \sum_{k=0}^{N_c-1} \left[\sum_{j=k+1}^{N_c} \left(\sum_{i=k}^{j-1} (-1)^{j-i-1} \binom{i}{k} \binom{j}{i+1} \right) h_1^{N_c-j} c_j(W) \right] (h_1 W)^k \\ &= \frac{1}{\det_c(\mathbb{1} + h_1 W)} (-1)^{N_c-1} \sum_{k=0}^{N_c-1} \left(\sum_{j=k+1}^{N_c} (-1)^{1+j-k} h_1^{N_c-j} c_j(W) \right) (h_1 W)^k. \end{aligned} \quad (2.71)$$

Specifically for $N_c = 3$, the determinant is given by eq. (A.32) and the coefficients of the characteristic polynomial by eqs. (A.25) and (A.27). The final result for the inverse sought-after is thus

$$(\mathbb{1} + h_1 W)^{-1} = \frac{1}{1 + h_1 L + h_1^2 L^\dagger + h_1^3} (1 + h_1 L - h_1 W + h_1^2 W^\dagger), \quad (2.72)$$

where $L = \text{tr}_c W$. By renaming $h_1 \rightarrow \bar{h}_1$ and $W \rightarrow W^\dagger$, it follows analogously that

$$(\mathbb{1} + \bar{h}_1 W^\dagger)^{-1} = \frac{1}{1 + \bar{h}_1 L^\dagger + \bar{h}_1^2 L + \bar{h}_1^3} (1 + \bar{h}_1 L^\dagger - \bar{h}_1 W^\dagger + \bar{h}_1^2 W). \quad (2.73)$$

With these relations at hand, the trace over Wilson line constructs eq. (2.58) can be written as

$$\begin{aligned} W_{n_1 m_1 n_2 m_2} &= \frac{1}{(1 + h_1 L + h_1^2 L^\dagger + h_1^3)^{n_1} (1 + \bar{h}_1 L^\dagger + \bar{h}_1^2 L + \bar{h}_1^3)^{n_2}} \\ &\quad \text{tr}_c \left[(h_1 W)^{m_1} (1 + h_1 L - h_1 W + h_1^2 W^\dagger)^{n_1} (\bar{h}_1 W^\dagger)^{m_2} \right. \\ &\quad \left. (1 + \bar{h}_1 L^\dagger - \bar{h}_1 W^\dagger + \bar{h}_1^2 W)^{n_2} \right] \end{aligned} \quad (2.74)$$

In this expression, no more inverses occur in the trace. Therefore, the Cayley-Hamilton theorem eq. (2.64) can be applied to reduce higher powers of W and W^\dagger to lower ones. To this end, one plugs eq. (A.28) for W^2 , eq. (A.29) for $(W^\dagger)^2$ and $WW^\dagger = \mathbb{1}$ recursively into eq. (2.74) until only solitary first powers of W and W^\dagger remain. Due to the trace in front of the whole numerator, the final outcome then only depends on the Polyakov loop L and its complex conjugate L^\dagger . This procedure has been automated with `Mathematica` in the context of the thesis at hand. In that way, the $W_{n_1 m_1 n_2 m_2}$ s can be expressed in terms of Polyakov loops for arbitrary values of n_1 , m_1 , n_2 and m_2 without any further effort, and also the last ingredient of the effective action has been transformed to Polyakov loops.

This completes our discussion of the effective theory in general, and equips us with all the tools and results required to implement it in a numerical simulation up to $\mathcal{O}(\kappa^4)$.

3. Numerical results

In this chapter, we will present the results obtained from a numerical Monte Carlo simulation of the effective theory which we constructed in chapter 2. Additionally, a further approximation of the theory in the limit of large N_τ and its range of validity in the case of finite-temperature studies will be discussed.

3.1. The integration measure

In section 2.8 it was shown how the degrees of freedom of the effective action can be transformed to Polyakov loops. For this reason, it is possible to change also the integration measure from temporal links to Polyakov loops, cf. eq. (2.28). This has the great advantage that one does not need to sample SU(3)-matrices U_4 , but only complex numbers L . The transformation introduces a Jacobian which can be written in the form of an effective potential:

$$Z_{\text{eff}} = \int [dU_4] e^{-S_{\text{eff}}} = \int [dL] e^{-S_{\text{eff}}} e^V. \quad (3.1)$$

For the gauge group SU(3), this potential is given by [7]

$$V = \sum_{\mathbf{x}} V_{\mathbf{x}} = \frac{1}{2} \sum_{\mathbf{x}} \ln \left(27 - 18|L_{\mathbf{x}}|^2 + 8 \operatorname{Re}(L_{\mathbf{x}}^3) - |L_{\mathbf{x}}|^4 \right). \quad (3.2)$$

The potential restricts the Polyakov loops to the domain allowed for traces of SU(3)-matrices as shown in fig. 3.1.

In order to sample this region correctly in the framework of a numerical simulation, it is convenient to adopt the gauge – frequently referred to as Polyakov gauge – where the temporal links $U_4(\mathbf{x}, \tau)$ are independent of τ and diagonal [15]:

$$U_4(\mathbf{x}, \tau) = \operatorname{diag} \left(e^{i\theta_1(\mathbf{x})/N_\tau}, e^{i\theta_2(\mathbf{x})/N_\tau}, e^{i\theta_3(\mathbf{x})/N_\tau} \right). \quad (3.3)$$

Here, the angles obey the SU(3) constraint $\theta_1(\mathbf{x}) + \theta_2(\mathbf{x}) + \theta_3(\mathbf{x}) = 0$ and are limited to the interval $[-\pi, \pi]$ [16]. In this gauge, the Polyakov loop takes the form

$$L_{\mathbf{x}} = e^{i\theta_1(\mathbf{x})} + e^{i\theta_2(\mathbf{x})} + e^{-i(\theta_1(\mathbf{x})+\theta_2(\mathbf{x}))}. \quad (3.4)$$

It turns out that changing the integration measure to the angles $\theta_{1,2}$ introduces another Jacobian which is identical to the one in eq. (3.1) [7], so that

$$Z_{\text{eff}} = \int [dU_4] e^{-S_{\text{eff}}} = \int [dL] e^{-S_{\text{eff}}} e^V = \int [d\theta_1][d\theta_2] e^{-S_{\text{eff}}} e^{2V}. \quad (3.5)$$

The effective theory can therefore be formulated completely in terms of $2N_s^3$ real degrees of freedom given by the angles $\theta_{1,2}(\mathbf{x})$. These are the variables that need to be sampled in the numerical simulation.

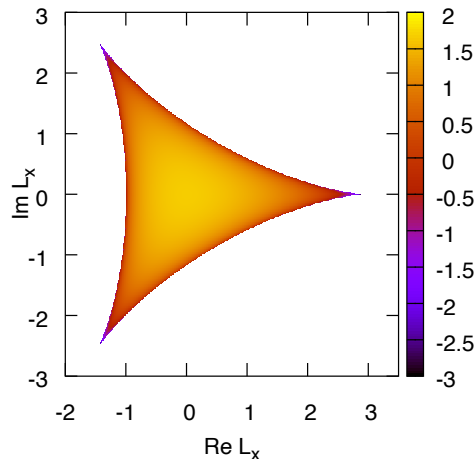


Figure 3.1.: The Polyakov loop potential for $SU(3)$ V_x induced by the change of the integration measure (cf. eq. (3.2))

3.2. The Monte Carlo method and the Metropolis algorithm

The expectation value of an observable in the effective theory is formally given by the path integral

$$\langle O \rangle = \frac{1}{Z_{\text{eff}}} \int [d\theta_1][d\theta_2] e^{-S_{\text{eff}}[\theta]} e^{2V[\theta]} O[\theta], \quad (3.6)$$

with Z_{eff} as in eq. (3.5). Even for a moderately large lattice with $N_s = 16$, this is a 8192-dimensional integral. The only way to evaluate such an expression is by Monte Carlo integration. Here, one replaces the integral by an average of the observable evaluated on N sample configurations [4],

$$\langle O \rangle \approx \hat{O} = \frac{1}{N} \sum_{n=1}^N O[\theta_n], \quad (3.7)$$

which is an estimator for the true mean value. Already for more than three dimensions, this method becomes more efficient than the usual numerical quadrature algorithms.

However, one does not need to generate the configurations $[\theta_n]$ completely randomly. For large lattice volumes the integrand of the path integral in eq. (3.6) is sharply peaked at some specific configurations, namely the ones which minimise the action [3]. Due to this, importance sampling may be applied: The huge sum in eq. (3.7) is reduced to a comparatively small sum over a subset of configurations sampled according to the probability distribution

$$dP[\theta] = \frac{1}{Z_{\text{eff}}} e^{-S_{\text{eff}}[\theta]} e^{2V[\theta]} [d\theta_1][d\theta_2]. \quad (3.8)$$

In this way it is ensured that no computation time is wasted on configurations which have only a negligible contribution.

The remaining problem consists of finding configurations $[\theta_n]$ which follow this probability distribution. The idea is to start from some arbitrary configuration and then to construct a stochastic sequence of configurations that eventually follows the desired equilibrium distribution

3. Numerical results

[4]. This is done with a Markov process, where the transition $[\theta] \rightarrow [\theta']$ happens with a given transition probability $T([\theta'] \leftarrow [\theta])$. It has to fulfil certain normalisation conditions, global balance and strong ergodicity. The latter means that every configuration can be reached with a finite probability from every other one, $T([\theta'] \leftarrow [\theta]) > 0$. Global balance implies that the equilibrium distribution is a fixed point of the Markov process [4].

A common choice for the transition probability is the Metropolis algorithm, which actually not only fulfils global balance, but also detailed balance [4]. It consists of the following two steps:

1. Choose a candidate configuration $[\theta']$ according to some a priori selection probability $T_0([\theta'] \leftarrow [\theta])$.
2. Accept the candidate configuration $[\theta']$ as the next configuration with the acceptance probability

$$T_A([\theta'] \leftarrow [\theta]) = \min \left(1, \frac{T_0([\theta] \leftarrow [\theta'])P[\theta']}{T_0([\theta'] \leftarrow [\theta])P[\theta]} \right). \quad (3.9)$$

If a suggested update is rejected, the unchanged configuration $[\theta]$ is used again in the Markov chain.

For the purpose of simulating the effective theory, only local changes are considered. In other words, the variables $\theta_{1,2}(\mathbf{x})$ are not modified at all lattice sites at once, but only at one (randomly selected) site \mathbf{x}_0 . Ergodicity is then reached by performing (at least) N_s^3 of such local updates, which is referred to as a sweep.

The candidate configuration is chosen as

$$\theta'_{1,2}(\mathbf{x}_0) = \theta_{1,2}(\mathbf{x}_0) + \varepsilon r_{1,2}, \quad (3.10)$$

where $r_{1,2}$ are two random numbers with $r_{1,2} \in [-\pi, \pi)$ and $\varepsilon < 1$ is a constant called stepsize. Since the Polyakov loop is periodic in $\theta_{1,2}$ with period 2π (cf. eq. (3.4)), one does not need to take care of the angles leaving the interval $[-\pi, \pi)$. If the random numbers $r_{1,2}$ are generated uniformly in this interval, eq. (3.10) obviously describes a symmetric selection probability in the sense that $T_0([\theta'] \leftarrow [\theta]) = T_0([\theta] \leftarrow [\theta'])$. In this case the acceptance probability eq. (3.9) simplifies to

$$T_A([\theta'] \leftarrow [\theta]) = \min \left(1, \frac{P[\theta']}{P[\theta]} \right) = \min \left(1, e^{-\Delta S} \right), \quad (3.11)$$

where $\Delta S = (S_{\text{eff}}[\theta'] - 2V[\theta']) - (S_{\text{eff}}[\theta] - 2V[\theta])$.

The stepsize is determined by fine-tuning the acceptance rate R_{acc} : If the stepsize is too large, the acceptance rate will be very low, which causes the Markov chain to frequently be stuck at a single configuration, thus wasting computation time. On the other hand, if the stepsize is too small and the acceptance rate very high, successive configurations are closely correlated. For the effective theory and the relevant lattice sizes, the optimal acceptance rate is located close to but above 50%¹. In order to find the corresponding stepsize, one starts with an initial guess ε_0 . The resulting acceptance rate is measured in the course of 10 sweeps. Afterwards, the stepsize is appropriately adapted. This procedure is repeated until the acceptance rate lies in a tolerable interval, which is chosen to be (48%, 60%). The formula employed for calculating the adapted stepsize is a double-step function,

$$\varepsilon' = \frac{1}{2} [\varepsilon \operatorname{erf}(6(R_{\text{acc}} - 0.25)) + (1 - \varepsilon) \operatorname{erf}(6(R_{\text{acc}} - 0.75)) + 1]. \quad (3.12)$$

¹[4] and Jangho Kim, private communication, 2020.

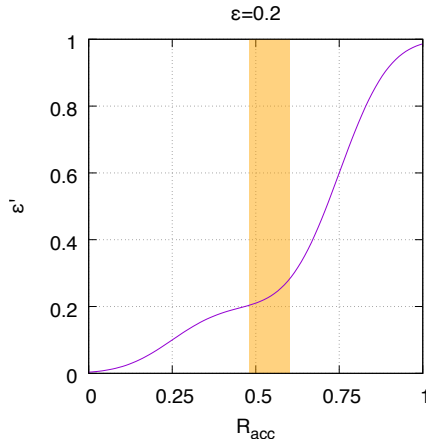


Figure 3.2.: The adaptive stepsize function eq. (3.12) for an old stepsize of $\varepsilon = 0.2$. The orange area indicates the tolerable interval for the acceptance rate

Figure 3.2 shows a plot of this function for $\varepsilon = 0.2$, which turned out to be a good initial guess. The value of ε' is restricted to the interval $(0, 1)$. If R_{acc} is close to 50%, the function is relatively flat around $\varepsilon' \sim 0.2$, allowing for fine-tuning. Farther away from the desired 50%-level, the function becomes steeper, so that ε is changed substantially within one step.

3.3. Implementation of the effective action and parallelisation

For the purpose of the C++ Monte Carlo simulation code, the effective action has been implemented including the λ_1 , λ_a and λ_2 gauge terms from eqs. (2.31) to (2.33), the static quark determinant eq. (2.43) and the kinetic quark determinant up to $\mathcal{O}(\kappa^4)$ (cf. appendix A.4) with the modifications due to the resummation, as detailed in section 2.7. For the effective couplings, the expressions in appendix A.1 have been used.

The change of the action ΔS in eq. (3.11) can be computed from the field values in the local neighbourhood alone, because only local updates are considered. In other words, the sum over the whole lattice $\sum_{\mathbf{x}}$ does not have to be evaluated for each update, but only such terms need to be considered which change if the values of $\theta_{1,2}$ are altered at one site \mathbf{x}_0 . This implies a great saving in terms of computation time.

In the following, we will go through all parts of the implemented action and explain which terms need to be included for the computation of ΔS . The effective potential eq. (3.2) and the static quark determinant eq. (2.43) are local quantities, so that only the term $\mathbf{x} = \mathbf{x}_0$ needs to be considered. For the two-point interactions (eqs. (2.31) and (2.32) for the gauge part and eqs. (A.33) to (A.35) for the fermionic part), the spatial sum can also be restricted to $\mathbf{x} = \mathbf{x}_0$, if in turn the sum over the directions i is extended to include negative directions on the spatial lattice as well, that is $i = \pm(1, 2, 3)$. The linear three-point interaction eq. (A.36) likewise has only one direction i of the hops, which needs to be extended to include negative directions. However, this still only accounts for those graphs which have their left or right end point at \mathbf{x}_0 . Those graphs which are centred at \mathbf{x}_0 need to be summed up separately, but here using positive directions i only. For the corner-like three-point interaction eq. (A.37), basically the same problem occurs, but with the additional complication that here two spatial directions i and j

3. Numerical results

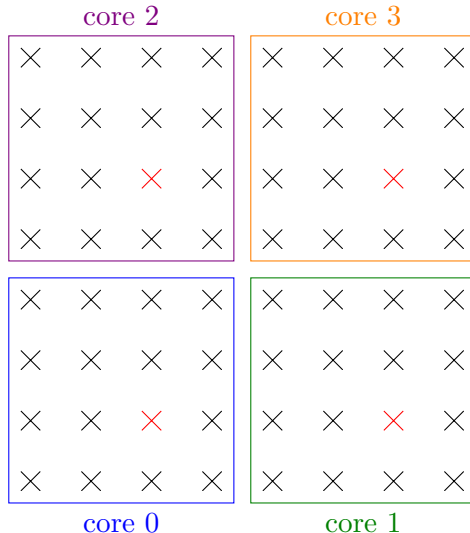


Figure 3.3.: Sub-lattices and associated CPU cores in two dimensions with $N_s = 8$. The sites which are updated simultaneously for one possible update are marked in red

need to be summed over. Both have to be extended to include negative directions, with the cases where i and j point in the same (or opposite) direction omitted. For the terms centred at \mathbf{x}_0 , an additional prefactor of $1/2$ becomes necessary because aforementioned sum double-counts the graphs with i and j interchanged. For the square-like four-point interaction eq. (A.39), the summation over i and j has to be done in the same way as for the corner-like graphs. Here, this suffices to be able to constrain the spatial sum to $\mathbf{x} = \mathbf{x}_0$; no extra terms as for the three-point interactions arise. In the gauge interaction at distance $\sqrt{2}a$ (cf. eq. (2.33)), only the end points of the diagonals are relevant, which is in contrast to the fermionic corner-like graphs. After rewriting $\sum_{[\mathbf{x}\mathbf{y}]} = \sum_{\mathbf{x}, i < j}$, one arrives at a spatial sum which one wants to restrict to $\mathbf{x} = \mathbf{x}_0$. For this purpose, in the summation over the two directions i and j (which is, in the first instance, treated as above) terms with i and j interchanged are indistinguishable and hence only to be counted once.

Apart from saving a large amount of computational cost for the updates, the fact that the variables $\theta_{1,2}$ are only changed locally allows a parallelisation of the simulation algorithm. To that end, the ‘global’ lattice is divided into several equally large ‘local’ sub-lattices. The spatial extent of these sub-lattices does not need to be the same for all directions, but it has to be equal to or greater 4 for all of them. Each CPU core then performs the calculations on one sub-lattice. A two-dimensional example of this is shown in fig. 3.3. For each update, one site of the local lattices is selected at random, and updated according to eqs. (3.10) and (3.11) on every core. The corresponding sites of the global lattice for a possible update of this kind are highlighted in red in fig. 3.3. Since two sites of the global lattice which are updated simultaneously are separated by a distance of (at least) four lattice units, but the maximal interaction distance in the implemented action is two lattice units, the local updates on the sub-lattices are independent of each other. This means that they can be carried out in parallel. As part of the thesis at hand, such a parallel version of the Metropolis algorithm for the effective theory has been implemented using MPI.

3.4. The Polyakov loop as an observable for the deconfinement transition

The simplest observable in the effective theory is the expectation value of the Polyakov loop. We will discuss its significance in the context of Lattice QCD first in the case of pure gauge theory and then address the modifications due to fermions.

For pure gauge theory, the expectation value of the Polyakov loop can be interpreted as the probability to observe a single static colour charge, as it is related to the free energy F_q of such a charge [4]:

$$|\langle L \rangle| \propto e^{-F_q/T}. \quad (3.13)$$

In the absence of dynamical quarks, a single colour charge cannot be screened in the confined phase. Therefore, $F_q \rightarrow \infty$ and the expectation value of the Polyakov loop is zero. In the deconfined phase, F_q is finite and $\langle L \rangle \neq 0$.

Another interpretation of the deconfinement transition is in terms of the centre symmetry of the gluonic action eq. (2.19). A centre transformation consists of multiplying all temporal links in a given time slice τ_0 with the same element z of the centre group Z_3 of the gauge group $SU(3)$ [4]:

$$U_4(\mathbf{x}, \tau_0) \rightarrow zU_4(\mathbf{x}, \tau_0). \quad (3.14)$$

The reason for this symmetry is that the gauge action eq. (2.19) is constructed from loops which are closed in a topologically trivial way. This means that they cross the τ_0 -plane the same number of times in the positive as in the negative direction. Because the elements of Z_3 commute with every $U \in SU(3)$, such loops are left invariant under the transformation (3.14). The Polyakov loop, however, is not closed in a topologically trivial way, but winds around the torus in the time direction, and hence transforms as $L \rightarrow zL$ [4]. Since the action is symmetric under centre transformations and the Polyakov loop is not, its expectation value has to vanish in the restored phase. Comparing to the discussion below eq. (3.13), this corresponds to the confined phase. In the deconfined phase, the Polyakov loop acquires a finite expectation value, which breaks the centre symmetry spontaneously. To sum up, $\langle L \rangle$ is an order parameter for the deconfinement transition in pure gauge theory.

In a finite volume the symmetry cannot be broken in a strict sense [4], which is why there is no true phase transition. The results for the Polyakov loop will populate the different centre sectors with equivalent probability in the broken phase, so that $\langle L \rangle$ always vanishes. Instead of $|\langle L \rangle|$ as in eq. (3.13) one therefore analyses $\langle |L| \rangle$, as both agree in the infinite volume limit [4]. This still leaves two different observables to consider, depending on whether one takes the absolute value before or after summing over the lattice:

$$Q_1 = \frac{1}{N_s^3} \left| \sum_{\mathbf{x}} L_{\mathbf{x}} \right|, \quad Q_2 = \frac{1}{N_s^3} \sum_{\mathbf{x}} |L_{\mathbf{x}}|. \quad (3.15)$$

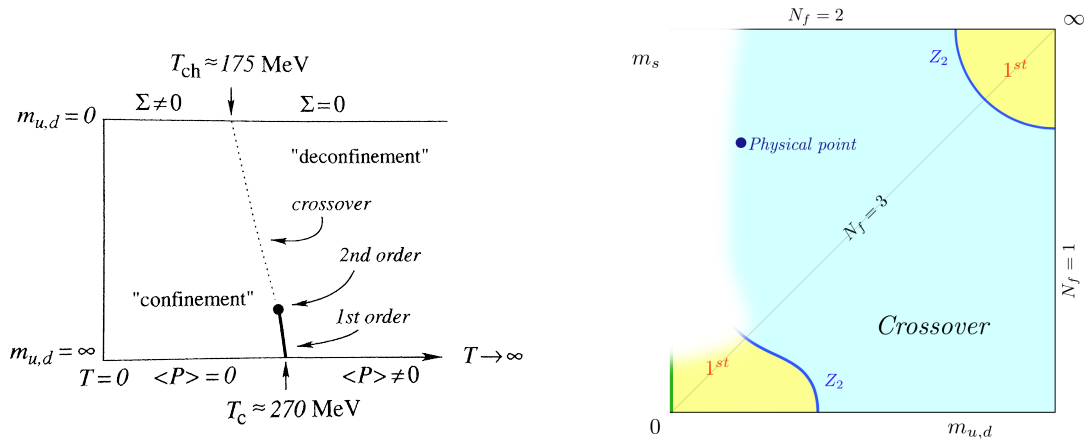
For the purpose of identifying the transition point, it is convenient to study higher moments of these observables. One defines the susceptibility χ_O , which corresponds to the variance of the distribution,

$$\chi_O = N_s^3 \mu_{2,O} = N_s^3 \langle (O - \langle O \rangle)^2 \rangle = N_s^3 (\langle O^2 \rangle - \langle O \rangle^2), \quad (3.16)$$

the skewness $\mu_{3,O}$, which corresponds to the third moment of the distribution,

$$\mu_{3,O} = \langle (O - \langle O \rangle)^3 \rangle = \langle O^3 \rangle - 3\langle O^2 \rangle \langle O \rangle + 2\langle O \rangle^3, \quad (3.17)$$

3. Numerical results



(a) The (T, m) -plane for the $N_f = 2$ sub-manifold (upper axis of fig. 3.4b) [4] (b) The Columbia plot: type of the transition for two degenerate flavours (mass $m_{u,d}$) and another third flavour (m_s) [17]

Figure 3.4.: The phase structure of Lattice QCD at zero chemical potential

and the kurtosis $B_{4,O}$, which corresponds to the fourth standardised moment of the distribution,

$$B_{4,O} = \frac{\mu_{4,O}}{\mu_{2,O}^2} = \frac{\langle (O - \langle O \rangle)^4 \rangle}{\langle (O - \langle O \rangle)^2 \rangle^2} = \frac{\langle O^4 \rangle - 4\langle O^3 \rangle \langle O \rangle + 6\langle O^2 \rangle \langle O \rangle^2 - 3\langle O \rangle^4}{(\langle O^2 \rangle - \langle O \rangle^2)^2}. \quad (3.18)$$

Here, we follow the nomenclature of [4] for the susceptibility and of [17] for the remaining moments.

So far, we were only concerned with pure gauge theory. Including dynamical fermions breaks the centre symmetry explicitly. This is due to the hopping terms $\propto \kappa$ in eq. (2.21), which contain all possible loops on the spatial lattice, including the ones which are closed in a topologically non-trivial way. Indeed, already the static determinant eq. (2.43) is formulated in terms of Polyakov loops, which are not invariant under centre transformations, as discussed above. The intuitive picture is that the dynamically generated quarks (vacuum loops) can screen the external colour charge, and the free energy F_q from eq. (3.13) is always finite [3]. This implies that $\langle L \rangle$ is not a true order parameter any more, as it is never exactly zero. Nevertheless, if the ‘symmetry breaking field’ κ is sufficiently small, the expectation value of the Polyakov loop shows a rapid change around the deconfinement transition. Under these circumstances, it may still be used to locate the transition point.

Accordingly, the first-order phase transition in Lattice QCD for $\kappa = 0$ weakens when decreasing the quark mass towards finite values. Eventually, the latent heat vanishes, and the first-order transition line ends with a critical end point, where the phase transition is of second order. For still lighter quarks, the transition is a crossover: The confinement and deconfinement domains are analytically connected [4]. In fig. 3.4a, this situation is illustrated in the (T, m) -plane for two degenerate quark flavours. When adding another flavour with a potentially different mass, the picture changes as shown in fig. 3.4b. This so-called Columbia plot visualises the type of the transition which the system undergoes for each point in the $(m_{u,d}, m_s)$ -space. The order of the transition in the two-flavour massless limit is still unclear. Therefore, the structure on the left part of the plot remains ambiguous and is blurred out [17].

3.5. Data analysis

After running the Monte Carlo simulation and measuring the observables, the next task is to analyse the obtained data. Because successive configurations are the result of a stochastic sequence, the Markov chain, there is a high chance that the observables have lots of similarities. To make a quantitative statement about this, one defines the autocorrelation function

$$C_O(O_n, O_{n+t}) = \langle (O_n - \langle O_n \rangle)(O_{n+t} - \langle O_{n+t} \rangle) \rangle = \langle O_n O_{n+t} \rangle - \langle O_n \rangle \langle O_{n+t} \rangle. \quad (3.19)$$

Here, n numbers the so-called computer time, which labels the consecutive configurations. For a Markov chain in equilibrium, which is reached for $n \rightarrow \infty$, the autocorrelation function depends only on the computer time separation t [4]:

$$C_O(t) = C_O(O_n, O_{n+t}). \quad (3.20)$$

The normalised autocorrelation function is then defined as

$$\Gamma_O(t) = \frac{C_O(t)}{C_O(0)}. \quad (3.21)$$

For correlated random variables O_n the variance of the estimator of the mean value eq. (3.7) is [4]

$$\begin{aligned} \sigma_{\hat{O}}^2 &= \langle (\hat{O} - \langle O \rangle)^2 \rangle = \left\langle \left(\frac{1}{N} \sum_{n=1}^N (O_n - \langle O \rangle) \right)^2 \right\rangle = \frac{1}{N^2} \left\langle \sum_{n,m=1}^N (O_n - \langle O \rangle)(O_m - \langle O \rangle) \right\rangle \\ &= \frac{1}{N^2} \sum_{n,m=1}^N C_O(|n-m|) = \frac{1}{N^2} \sum_{t=-N}^N (N-|t|) C_O(|t|) = \frac{C_O(0)}{N} \sum_{t=-N}^N \Gamma_O(|t|) \left(1 - \frac{|t|}{N} \right) \\ &\approx \frac{\sigma_O^2}{N} 2 \left(\frac{1}{2} + \sum_{t=1}^N \Gamma_O(t) \right) = \frac{\sigma_O^2}{N} 2\tau_{O,\text{int}}(N), \end{aligned} \quad (3.22)$$

where the integrated autocorrelation time

$$\tau_{O,\text{int}}(N) = \frac{1}{2} + \sum_{t=1}^N \Gamma_O(t) = \frac{1}{2} \sum_{t=-N}^N \Gamma_O(|t|) \quad (3.23)$$

has been introduced. From the second to the last line in eq. (3.22), the factor $1 - |t|/N$ has been neglected. This is justified for $N \rightarrow \infty$, as $\Gamma_O(t)$ is exponentially suppressed for large t [4]. For the practical determination of the autocorrelation time this implies that one may truncate the sum in eq. (3.23) at relatively small values of t . Comparing the results for different truncations then allows an accurate measurement of the autocorrelation time.

In figs. 3.5 and 3.6 two examples of this method are shown², one close to and one far away from the phase transition. In both cases, the integrated autocorrelation time plateaus at some value of t_{max} . Afterwards, the estimate for $\Gamma(t)$ becomes unreliable, and τ_{int} starts to fluctuate. One therefore usually regards the first plateau in these plots as the best estimate for the integrated autocorrelation time.

²For the calculation of the integrated autocorrelation time, the ‘Monte Carlo C++ analysis tools’ developed by Dr. Alessandro Sciarra were used.

3. Numerical results

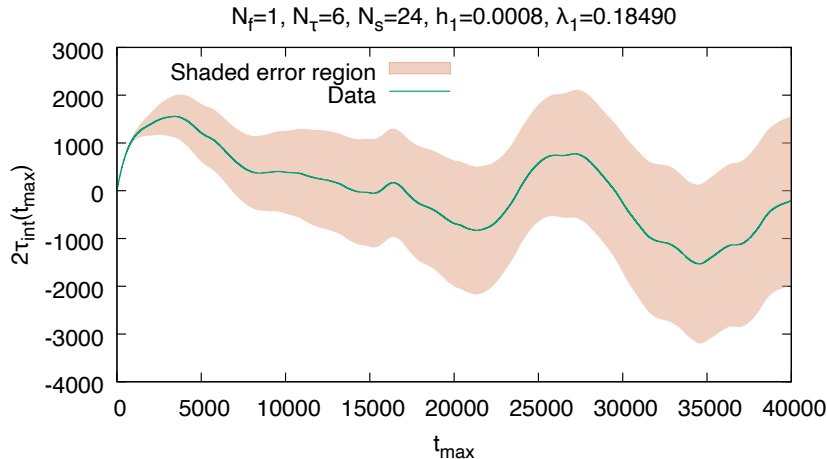


Figure 3.5.: Integrated autocorrelation time eq. (3.23) for the observable Q_2 (cf. eq. (3.15)) measured every 150 sweeps close to the phase transition

When comparing the two results, it stands out that τ_{int} is more than ten times larger for the simulation close to the phase transition than for the remote one, $2\tau_{\text{int}} \approx 1600$ in contrast to $2\tau_{\text{int}} \approx 120$, respectively. This is a well-known feature of Lattice Quantum Field Theories in general, which is referred to as critical slowing down. One expects that the integrated autocorrelation time obeys the dynamical scaling law $\tau_{O,\text{int}} \propto (\xi_O)^{z(O)}$, where ξ_O is the correlation length for the observable O and $z(O) > 0$ the dynamical critical exponent [3]. In the vicinity of critical points, which is where the parameters chosen in fig. 3.5 are located, the correlation length diverges. On finite size lattices, however, one has $\xi \leq N_s$ and thus $\tau_{O,\text{int}} \propto N_s^{z(O)}$ [4]. This shows that measurements are much more correlated when simulating close to phase transitions, especially second-order ones.

A comparison of eq. (3.22) with the result for uncorrelated observables, $\sigma_O^2 = 1/N\sigma_O^2$ [4], reveals the significance of the integrated autocorrelation time: The effective number of independent measurements is $N/2\tau_{O,\text{int}}$. If the numerical measurement of O takes a substantial amount of CPU time, it is hence better to skip about $2\tau_{O,\text{int}}$ configurations between the measurements. For most of the simulations performed in the context of the thesis at hand, 150 sweeps over the lattice volume were carried out between successive measurements. As one can see from figs. 3.5 and 3.6, a considerable amount of autocorrelation remains nevertheless.

To handle varying and unpredictable autocorrelation times, the technique of binning can be applied. One divides the data into sub-blocks of a specified size and averages the primary quantities first in these bins. The obtained bin averages themselves can then be considered as results of single measurements. If the bin size is large enough, these bin averages can be treated as uncorrelated [3].

In practice, however, the number of data is often too small to extract reliable error estimates in this way. An additional obstacle are secondary quantities, which are functions of the averages (the primary quantities). Here, dividing the whole data set into smaller parts means considering sub-samples, because secondary quantities are defined on samples. The usual bins are in most cases too small for this purpose. Moreover, the effects of error propagation may be difficult to determine.

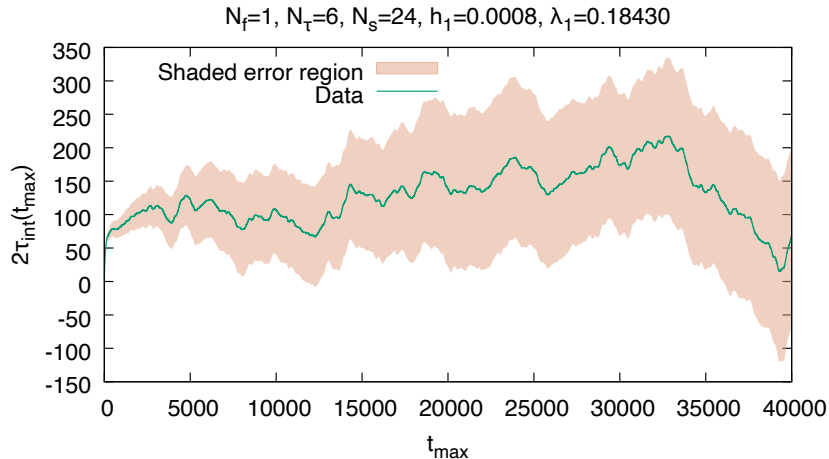


Figure 3.6.: Integrated autocorrelation time eq. (3.23) for the observable Q_2 (cf. eq. (3.15)) measured every 150 sweeps far away from the phase transition

For these reasons, a Jackknife analysis is used in this thesis for the computation of averages and error estimates. One starts with a data set of length N for a primary quantity O , whose average \hat{O} is given by eq. (3.7). Now, one constructs N subsets by removing the s -th entry of the original set ($s = 1, \dots, N$) [3]:

$$O_s^{(J)} = \frac{1}{N-1} \sum_{r \neq s} O_r. \quad (3.24)$$

The best estimator for a secondary quantity is $\hat{y} = y(\hat{O})$, not $y(\widehat{O})$ [3]. The corresponding Jackknife estimators are $y_s^{(J)} = y(O_s^{(J)})$, with an average

$$\hat{y}^{(J)} = \frac{1}{N} \sum_{s=1}^N y_s^{(J)} = \frac{1}{N} \sum_{s=1}^N y(O_s^{(J)}). \quad (3.25)$$

The variance of the Jackknife estimators is then [4]:

$$\left(\sigma_{\hat{y}^{(J)}}\right)^2 = \frac{N-1}{N} \sum_{s=1}^N \left(y_s^{(J)} - \hat{y}^{(J)}\right)^2. \quad (3.26)$$

Apart from the calculation of a more reliable error estimate, performing a Jackknife analysis allows a bias correction of the average. The unbiased estimator is given by [4]

$$\hat{y}_{\text{unbiased}} = \hat{y} - (N-1) \left(\hat{y}^{(J)} - \hat{y}\right) = N\hat{y} - (N-1)\hat{y}^{(J)}. \quad (3.27)$$

For the practical implementation the Jackknife analysis is combined with binning by organising the data in bins and constructing subsets by removing entire bins instead of only single values.

To establish the correct binsize, such an analysis is carried out for several values of the binsize. Once the bins are large enough, they are practically uncorrelated and the obtained error estimates remain constant if the bins are further increased. Two examples of this procedure can be seen in figs. 3.7 and 3.8. They belong to the same simulations as the illustrations of the

3. Numerical results

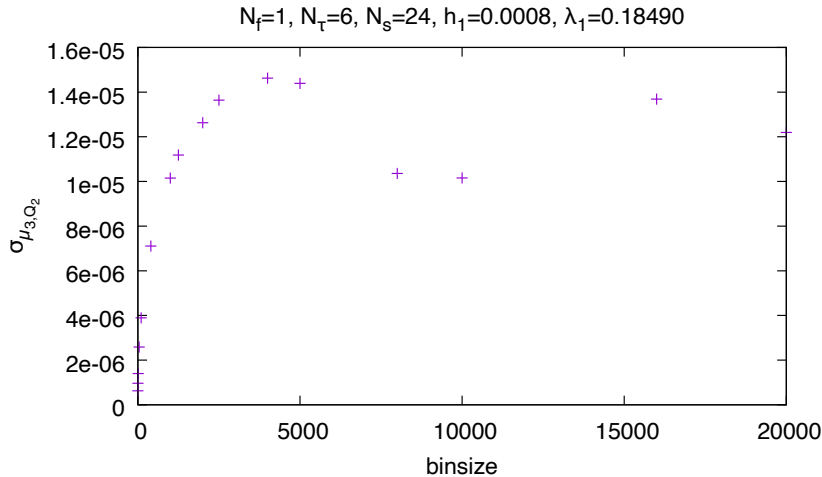


Figure 3.7.: Error analysis by binning and Jackknife for the skewness of Q_2 with measurements every 150 sweeps close to the phase transition

autocorrelation in figs. 3.5 and 3.6. Again, the resulting ideal binsizes differ by a factor of at least ten. For the simulation far away from the phase transition, a binsize of 400 already gives a reliable error estimate, whereas close to the phase transition a binsize of about 4000 is optimal. For even larger binsizes, the error estimate starts to fluctuate. This is because the number of very large bins is too small, so that the error of the error estimate becomes large [3]. The outcomes of this combined binning and Jackknife analysis may be compared with the direct computation of the integrated autocorrelation time. One finds that the former yields a quite conservative estimate of the number of configurations that needs to be skipped (or binned) for the data to decorrelate. It is therefore sufficient to create plots like figs. 3.7 and 3.8 in order to determine the correct binsize. The calculation of the integrated autocorrelation time, which is much more expensive and involved, can be avoided.

3.6. The deconfinement transition at zero chemical potential

The effective theory contains with the hopping parameter expansion an expansion around heavy quarks and is hence located in the upper right corner of the Columbia plot fig. 3.4b. It inherits the phase structure of Lattice QCD in this region [18]. For given N_f , N_τ and $\mu = 0$, the theory has two free parameters β and κ , which can alternatively be specified by the two effective couplings $\lambda \equiv \lambda_1$ and $h \equiv h_1 = \bar{h}_1$. As for full Lattice QCD, the first-order phase transition of pure gauge theory ($h = 0$) weakens for increasing h , until the transition vanishes at a critical end point. A sketch of the corresponding phase diagram for the effective theory in terms of the effective couplings λ and h is shown in fig. 3.9.

The present section aims to measure this phase diagram, and in particular the coordinates $(\lambda_c, h_c) \leftrightarrow (\beta_c, \kappa_c)$ of the critical end point.

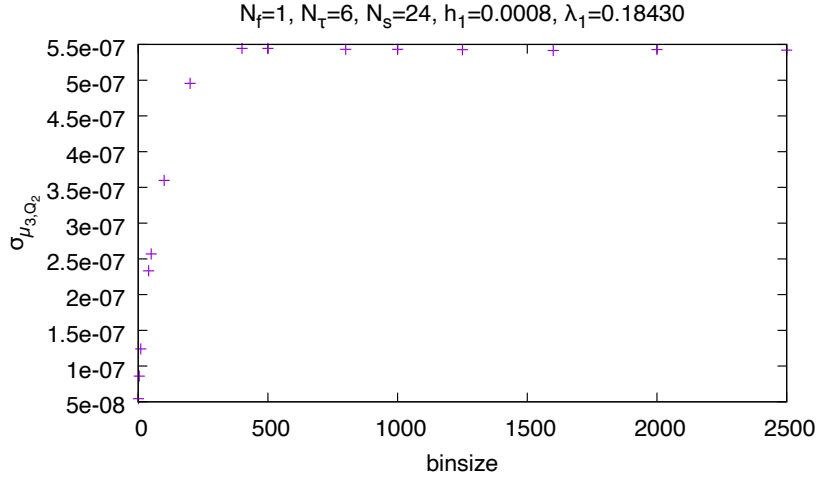


Figure 3.8.: Error analysis by binning and Jackknife for the skewness of Q_2 with measurements every 150 sweeps far away from the phase transition

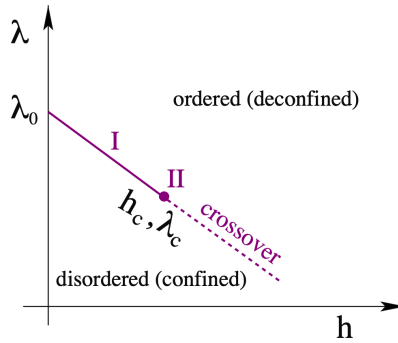


Figure 3.9.: Sketch of the phase diagram for the effective theory at $\mu = 0$ and given N_f, N_τ [18]

3.6.1. The analysis using the example of static quarks

For this purpose, a two-step procedure analogous to the one used in [18] is pursued. In the first step, one scans the phase diagram at constant values of h in the λ -direction and looks out for the phase boundary. After having established this pseudo-critical line $\lambda_{pc}(h)$, the order of the transition along that line is determined. In this way, the point where the type of the transition changes from first order to crossover can be found. We will go through both steps in detail using only the λ_1 -action eq. (2.31) for the gauge part and the static determinant eq. (2.43) for the fermionic part of the one-flavour theory. This allows us to check our implementation of the thus reduced action and of the algorithm against the results obtained in [18].

Determination of the phase boundary

The phase transition leaves different characteristic traces in the moments of the observable Q_2 . The expectation value itself shows a rather steep rise due to the remnants of the spontaneous breaking of the centre symmetry in a finite volume, as discussed in section 3.4. An example of this at $h = 0.0006$ is shown in fig. A.1. The susceptibility eq. (3.16) corresponds to the

3. Numerical results

variance of the distribution of Q_2 . Deeply in one of the phases, the probability distribution is a single Gaussian peak around its mean value. Near the transition, a second peak develops, which increases in height until it contains most of the data points and the first peak eventually vanishes. Therefore, the distribution is the broadest right at the transition point, so that χ_{Q_2} has a maximum there (cf. fig. A.2). The skewness eq. (3.17) describes how much the distribution is slanted to one side, that is how asymmetric it is. For the single Gaussian peak in one of the phases, the distribution is not askew at all, $\mu_{3,Q_2} = 0$. When closing in on the phase transition, the absolute value of μ_{3,Q_2} grows as a consequence of the evolution of a second, smaller peak. The sign of μ_{3,Q_2} depends on whether the transition is approached from the left or the right. Exactly at the transition point both peaks are equal in height and the distribution is symmetric, $\mu_{3,Q_2} = 0$ (cf. fig. A.3). The kurtosis eq. (3.18) finally quantifies the contribution of the tail of the distribution. It has a minimum at the phase transition [17] and gets larger when moving away from it (cf. fig. A.4). This is because the ansatz of two displaced Gaussians underestimates the actual distribution in its wings [19]. The maximum of the susceptibility is usually relatively broad, so that the most precise estimate of the pseudo-critical coupling $\lambda_{\text{pc}}(h)$ can be obtained from the zero-crossing of the skewness or the minimum of the kurtosis.

This analysis is repeated for several different values of h . At $h = 0$, 80 000 sweeps over the volume were performed for each λ . For finite h it were 100 000 sweeps per combination of the couplings and the system size at $N_s = 14$ and 16, and at least 200 000 at $N_s = 18, 20$ and 22. An exception is $h = 0.002$, where only 50 000 sweeps were carried out for all volumes. The result for the pseudo-critical line of the largest $N_s = 22$ is displayed in fig. 3.10. It is well described by a linear fit. This is due to the smallness of h and the fact that along the first-order transition line the free energy densities of the confined and deconfined phases are equal, that is $f_c(\lambda_{\text{pc}}(h), h) = f_d(\lambda_{\text{pc}}(h), h)$. Close to the point $(\lambda_0, 0)$ the free energy density of the confined phase is given by

$$f_c(\lambda, h) = f_c(\lambda_0, 0) + \left(\frac{\partial f_c}{\partial \lambda} \right)_{(\lambda_0, 0)} (\lambda - \lambda_0), \quad (3.28)$$

because $(\partial f_c / \partial h)_{(\lambda_0, 0)} = 0$ in the confined phase [20]. For the deconfined phase this is not the case, so that

$$f_d(\lambda, h) = f_d(\lambda_0, 0) + \left(\frac{\partial f_d}{\partial \lambda} \right)_{(\lambda_0, 0)} (\lambda - \lambda_0) + \left(\frac{\partial f_d}{\partial h} \right)_{(\lambda_0, 0)} h. \quad (3.29)$$

Setting eqs. (3.28) and (3.29) equal along the pseudo-critical line and using the condition $f_c(\lambda_0, 0) = f_d(\lambda_0, 0)$ for the first-order transition at $h = 0$, one arrives at

$$\lambda_{\text{pc}}(h) = \lambda_0 - a_1 h, \quad a_1 = - \left. \frac{\partial f_d / \partial h}{\partial (f_c - f_d) / \partial \lambda} \right|_{(\lambda_0, 0)}, \quad (3.30)$$

the asserted linear dependence. A fit with $\chi^2/\text{d.o.f.} \approx 0.44$ to the data illustrated in fig. 3.10 yields

$$\lambda_0 = 0.18804(23), \quad a_1 = 1.83(33), \quad (3.31)$$

which is in good agreement with the results obtained in [18].

Localisation of the critical point

The next task is to find the location of the critical end point on the phase boundary, which is accomplished by means of a finite size scaling analysis. In the vicinity of the critical point, the behaviour of the system is dictated by its universality class, which is in turn determined by the

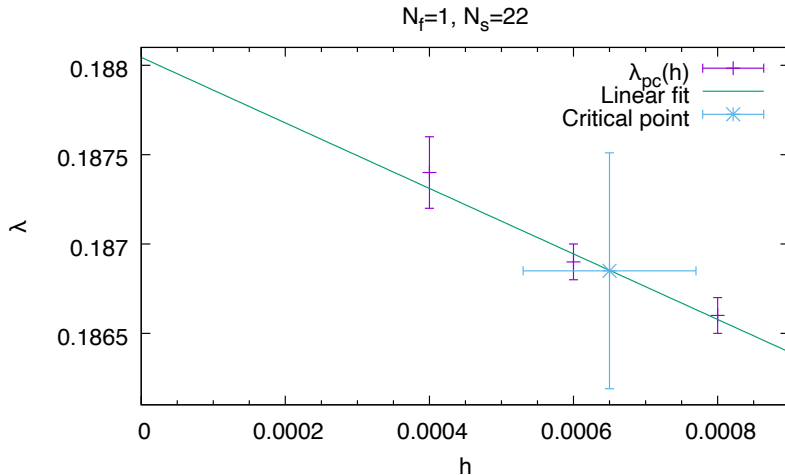


Figure 3.10.: The pseudo-critical line for static quarks with one flavour and $N_s = 22$. A linear fit according to eqs. (3.30) and (3.31) and the critical point eq. (3.34) are also shown

symmetry that is being broken. In the case of the effective theory this is a global Z_3 -symmetry (cf. section 3.4). It has been found that such models belong to the same universality class as the three-dimensional Ising model [20]. The underlying reason is that the critical point is the end point of a first-order transition line, like in a liquid-gas transition. Consequently, close to the critical point the kurtosis should scale according to

$$B_4 = f_0 + f_1(h - h_c)N_s^{1/\nu} + \dots, \quad (3.32)$$

with the universal values of $f_0 = 1.604$ and $\nu = 0.630$ [18].

The approach is now the following: The minimum values of B_{4,Q_2} , that is the ones on the pseudo-critical line, are plotted as a function of h for several volumes (cf. fig. 3.11). Then, a fit as per eq. (3.32) is performed, where $\nu = 0.630$ is kept fixed, and h_c , f_0 and f_1 are varied³. A fit with $\chi^2/\text{d.o.f.} \approx 1.12$ yields

$$h_c = 0.00065(12), \quad f_0 = 1.71(9), \quad f_1 = 7.7(1.0). \quad (3.33)$$

Considering the error, the result for f_0 is almost compatible with its universal value. The coordinates of the critical point are calculated by plugging the result for h_c into eq. (3.31):

$$\lambda_c = 0.18685(66), \quad h_c = 0.00065(12). \quad (3.34)$$

This perfectly coincides with the findings in [18], if the uncertainty ranges are taken into account. We conclude that our implementation of the effective potential, the λ_1 gauge action, the static quark determinant and the Metropolis algorithm, as well as the data analysis procedure, seem to be correct.

3.6.2. Effect of larger-distance interactions in the gauge action

The next thing one can check is the effect of including larger-distance interactions, in our case the λ_2 -action eq. (2.33), in the gauge action. For the purpose of comparing with [21], one can

³For these fits, the ‘Python Fitting GUI’ developed by Reinhold Kaiser was used.

3. Numerical results

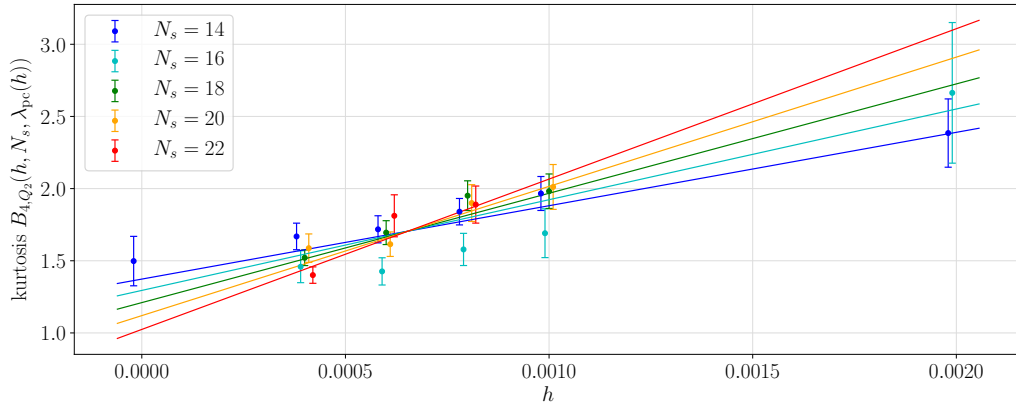


Figure 3.11.: Kurtosis B_{4,Q_2} as a function of h on the pseudo-critical line $\lambda_{pc}(h)$ for static quarks with one flavour on various volumes

choose the two couplings λ_1 and λ_2 independent of each other. The effective theory may then be regarded as an academic spin model, since the connection to QCD (or Yang-Mills theory) can only be made for the specific interrelationship of λ_1 and λ_2 implied by eqs. (A.4) and (A.5).

In order to assess the influence of a finite value of λ_2 on the location of the phase transition, pure gauge theory ($h = 0$) is simulated at a fixed, positive value of λ_2 . Similar to above, one scans this system in λ_1 and looks out for the typical signatures of the phase transition. Because the main interest of the thesis at hand is still in the effective theory as a model for QCD, a value of λ_2 close to the transition point of full Yang-Mills theory at $N_\tau = 4$ has been selected, $\lambda_2 = 0.0288$. For each combination of λ_1 and N_s , 50 000 sweeps over the volume were performed. A plot of the skewness of Q_2 as a function of λ_1 can be seen in fig. 3.12. The phase transition obviously occurs at $\lambda_{1,pc} \approx 0.102$, which is consistent with the phase boundary of the two-coupling theory as per [21]. When comparing this with the result for the one-coupling theory, $\lambda_{1,pc} \approx 0.188$ (cf. eq. (3.31)), one recognises the expected behaviour: The inclusion of such a larger-distance interaction in the gauge action lowers the pseudo-critical value of λ_1 significantly.

3.6.3. The critical point of the one-flavour theory to $\mathcal{O}(\kappa^4)$

In the following, the ‘full’ version of the implemented action (cf. section 3.3) shall be investigated. As mentioned in section 3.6.2, the connection of the effective theory to QCD can only be made if the couplings are interrelated as detailed in appendix A.1. Because the effective theory has now more than two such parameters, the choice of N_τ matters. This is in contrast to the case of static quarks with only the λ_1 gauge action, which has been examined in section 3.6.1. There, the effective theory had only two free parameters λ and h , which could be converted to the QCD parameters β and κ for any N_τ .

We will study first the one-flavour theory for two different values of N_τ in order to be able to compare the results with the ones obtained in section 3.6.1. In the next subsection, we will then turn to the physically more interesting case of the two-flavour theory.

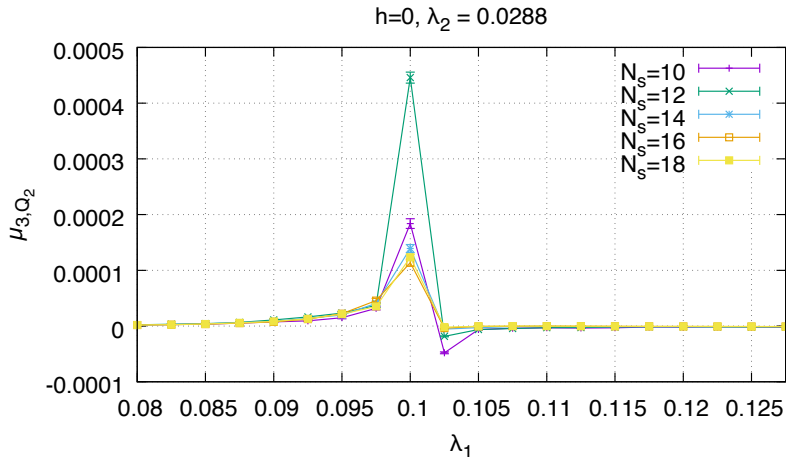


Figure 3.12.: Skewness of Q_2 for pure gauge theory with two couplings and fixed $\lambda_2 = 0.0288$ on various volumes

Results for $N_\tau = 4$

The same analysis that has been demonstrated using the example of static quarks can also be applied to the effective theory with more corrections. The simulations were again conducted at several constant values of h_1 , while varying λ_1 , because h_1 is the relevant coupling of the effective theory which governs the physical behaviour of the system. Besides, this facilitates the comparison with section 3.6.1. For the runs at $N_\tau = 4$, 200 000 sweeps over the volume were performed for each combination of the couplings and the system size at $N_s = 18, 20$ and 22 , at least 400 000 at $N_s = 24$, and at least $3 \cdot 10^6$ at $N_s = 32$. Moreover, the complete analysis has been carried out for both observables Q_1 and Q_2 from eq. (3.15). From now on, all relevant plots will be collected in appendix A.6. The pseudo-critical lines that have been obtained for the largest $N_s = 32$, for example, can be found in fig. A.5. Both curves have been fitted to eq. (3.30). For Q_1 , a fit with $\chi^2/\text{d.o.f.} \approx 0.65$ yields

$$\lambda_0 = 0.167356(48), \quad a_1 = 1.242(24), \quad (3.35)$$

and for Q_2

$$\lambda_0 = 0.167310(32), \quad a_1 = 1.206(18), \quad (3.36)$$

where $\chi^2/\text{d.o.f.} \approx 0.40$. As the two results agree within errors, it may be inferred that either observable is qualified to identify the phase transition. When comparing above number for λ_0 with the one for static quarks (cf. eq. (3.31)), one might jump to the conclusion that incorporating higher-order corrections in the fermionic action diminishes the value of λ_1 at the phase transition. However, a large reduction is already due to the inclusion of the λ_2 -action, as has been discussed in section 3.6.2. Hence, and because a_1 is smaller than in the static case as well, the fermionic corrections actually enlarge $\lambda_{1,\text{pc}}$. Since the pseudo-critical line is always going down with growing h_1 , the impact of fermions in general is to decrease $\lambda_{1,\text{pc}}$, suggesting that the $\mathcal{O}(\kappa^4)$ -corrections weaken this effect.

In order to establish the coordinates of the critical point, an analysis of the kurtosis identical to the one applied in section 3.6.1 is performed. The corresponding plots are displayed in fig. A.6 using the observable Q_1 and in fig. A.7 using Q_2 . In both cases, the data point at

3. Numerical results

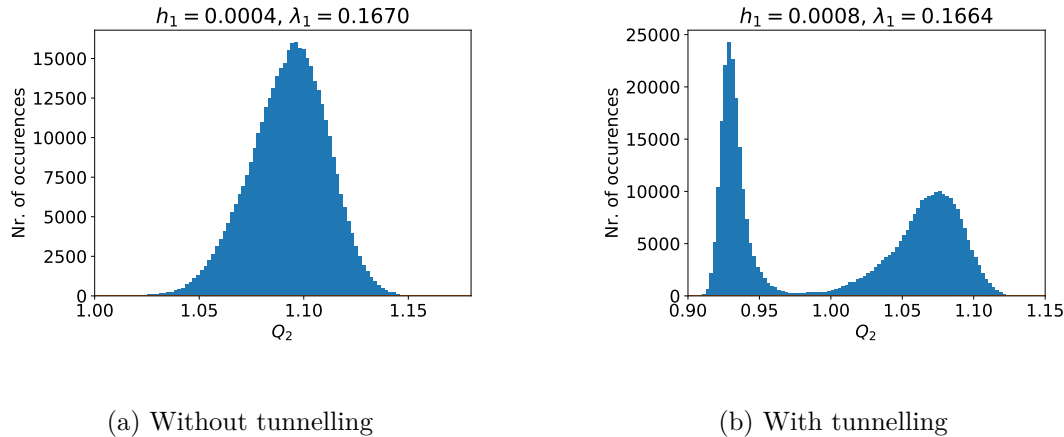


Figure 3.13.: Histograms of Q_2 for two different simulations with one flavour, $N_7 = 4$ and $N_s = 24$ in the minimum of B_{4,Q_2}

$h_1 = 0.0004$ and $N_s = 24$ has been excluded for the purpose of the final fit. The reason for this is that it has a very small error in spite of being a definite outlier. To investigate this further, one may take a look at the histogram of Q_2 for this point (cf. fig. 3.13a) and compare it with a histogram in the minimum of B_{4,Q_2} for, say, $h_1 = 0.0008$ (cf. fig. 3.13b). Here, a striking discrepancy can be observed: The histogram at $h_1 = 0.0004$ has only one peak, whereas the other one has two. This means that the Markov chain at the point in question has only visited the deconfined phase, and no tunnelling between the two phases has occurred. Consequently, only one part of the probability distribution of Q_2 has been measured, merely feigning a high precision. The resulting $B_{4,Q_2} \approx 3$ is the expected one for a single Gaussian distribution, lacks any physical meaning, and thus has to be excluded from the analysis.

Fitting the data illustrated in figs. A.6 and A.7 according to eq. (3.32) yields

$$h_{1,c} = 0.00171(13), \quad f_0 = 1.59(9), \quad f_1 = 4.59(25) \quad (3.37)$$

for Q_1 , where $\chi^2/\text{d.o.f.} \approx 0.96$, and

$$h_{1,c} = 0.00194(17), \quad f_0 = 1.84(11), \quad f_1 = 4.05(28) \quad (3.38)$$

for Q_2 , where $\chi^2/\text{d.o.f.} \approx 0.56$. By plugging the numbers for $h_{1,c}$ into eqs. (3.35) and (3.36), respectively, the coordinates of the critical point are calculated as

$$\lambda_{1,c} = 0.16523(25), \quad h_{1,c} = 0.00171(13) \quad (Q_1), \quad (3.39)$$

$$\lambda_{1,c} = 0.16497(27), \quad h_{1,c} = 0.00194(17) \quad (Q_2). \quad (3.40)$$

Here, the differences between the two observables are larger than for the determination of the pseudo-critical line. Nonetheless, the results are consistent with each other within their error ranges. Judging by the value of f_0 and the quality of the fit, the analysis with Q_1 is probably the more trustworthy one. In principle, however, both should coincide in the limit of infinite statistics, which is compatible with above findings. It is conspicuous that the result for $h_{1,c}$ is considerably larger than the one calculated for static quarks (cf. eq. (3.34)). This is in accordance with aforementioned inference that the $\mathcal{O}(\kappa^4)$ -corrections weaken the overall effect of fermions: When including those corrections, the value of κ and therefore h_1 has to be higher to achieve the same physical effect as in the static case. Still, the shift is small enough

to justify the expansions made in the derivation of the effective theory and the omission of even higher-order corrections.

The critical couplings eqs. (3.39) and (3.40) can now be converted to the QCD parameters β and κ by numerically inverting the relations (A.4) and (A.7) at fixed $N_\tau = 4$. One finds

$$\beta_c = 6.04140(69), \quad \kappa_c = 0.0976(17) \quad (Q_1), \quad (3.41)$$

$$\beta_c = 6.04068(74), \quad \kappa_c = 0.1005(20) \quad (Q_2). \quad (3.42)$$

The results for the two observables again agree with each other within their error ranges, as expected.

Another interesting quantity to compute from these values is the physical temperature eq. (2.14) at the critical point. For this purpose, the lattice spacing a has to be calculated, that is, a scale has to be set. In principle, the lattice spacing depends on both β and κ : $a = a(\beta, \kappa)$. Since the critical point of the effective theory is located in the heavy-quark regime ($\kappa \ll 1$), one can exploit the fact that heavy quarks have only a small influence on the running coupling [7]. Therefore, one approximates $a = a(\beta)$ and uses the interpolation function for pure gauge theory [7]

$$a(\beta) = r_0 \exp[-1.6804 - 1.7331(\beta - 6) + 0.7849(\beta - 6)^2 - 0.4428(\beta - 6)^3], \quad (3.43)$$

which is valid for $5.7 < \beta < 6.92$. Here, $r_0 = 0.5 \text{ fm}$ is the so-called Sommer parameter. A numerical inversion of this function yields for the lattice spacing and the physical temperature at the critical point:

$$a_c \approx 0.086814 \text{ fm} \Rightarrow T_c \approx 568.24 \text{ MeV} \quad (Q_1), \quad (3.44)$$

$$a_c \approx 0.086919 \text{ fm} \Rightarrow T_c \approx 567.56 \text{ MeV} \quad (Q_2). \quad (3.45)$$

This is in perfect concordance with the result for pure gauge theory at $N_\tau = 4$ obtained in [18] using only the static determinant and the λ_1 gauge action, and thus demonstrates once again that the physics is not strongly dependent on higher fermionic corrections to the effective theory.

Results for $N_\tau = 6$

For the one-flavour theory with $N_\tau = 6$, the same calculations were made as for $N_\tau = 4$. In the corresponding simulations, at least $3 \cdot 10^6$ sweeps over the volume were performed for each combination of the couplings and the system size. For reasons of clarity and to simplify the comparison between the different parameter sets, the results of the analysis are collected in table 3.1 together with all the previously reported ones. The associated plots can be found in appendix A.6.2.

Similar to the data for $N_\tau = 4$, there are some discrepancies between the quantities computed from the two observables Q_1 and Q_2 . They are, however, still consistent with each other within their error ranges. Here, the analysis using Q_2 seems to be the more trustworthy one, if one considers the result for f_0 and the quality of the fit. When comparing the numbers for $N_\tau = 6$ to those for $N_\tau = 4$, one notes that in the former case λ_1 at the phase transition and hence also at the critical point is larger; the same holds for β_c . This larger value of the (inverse) gauge coupling leads to a smaller lattice spacing according to eq. (3.43). Since the physical temperature is given by $T = (aN_\tau)^{-1}$, this smaller lattice spacing compensates for the growing

3. Numerical results

Table 3.1.: Numerical results for the pseudo-critical line eq. (3.30), the finite-size scaling of the kurtosis eq. (3.32) and the critical point. The fits to the pseudo-critical line all have $0.04 \lesssim \chi^2/\text{d.o.f.} \lesssim 0.65$, the ones to the kurtosis $0.29 \lesssim \chi^2/\text{d.o.f.} \lesssim 1.48$

Action		$\lambda_1 + \text{static det.}$	$\lambda_1 + \lambda_a + \lambda_2 + \text{static det.} + \kappa^2 + \kappa^4$			
N_f		1	1	1	2	2
N_τ		–	4	6	4	6
λ_0	Q_1	0.18822(11)	0.167356(48)	0.186139(31)	0.167381(15)	0.186147(67)
	Q_2	0.18804(23)	0.167310(32)	0.186163(32)	0.167329(33)	0.186126(41)
a_1	Q_1	2.17(17)	1.242(24)	1.560(28)	2.476(16)	3.21(14)
	Q_2	1.83(33)	1.206(18)	1.554(32)	2.410(32)	3.089(85)
f_0	Q_1	1.24(9)	1.59(9)	1.46(8)	1.47(6)	1.44(6)
	Q_2	1.71(9)	1.84(11)	1.69(7)	1.59(7)	1.74(4)
f_1	Q_1	7.8(8)	4.59(25)	5.2(5)	8.4(5)	11.1(9)
	Q_2	7.7(1.0)	4.05(28)	5.1(5)	8.1(5)	10.8(7)
$h_{1,c}$	Q_1	0.00035(12)	0.00171(13)	0.00084(9)	0.00081(5)	0.00040(4)
	Q_2	0.00065(12)	0.00194(17)	0.00100(8)	0.00084(6)	0.000488(27)
$\lambda_{1,c}$	Q_1	0.18746(43)	0.16523(25)	0.18483(19)	0.16538(15)	0.18486(25)
	Q_2	0.18685(66)	0.16497(27)	0.18461(19)	0.16530(20)	0.18462(17)
κ_c	Q_1	–	0.0976(17)	0.1400(21)	0.0819(12)	0.1258(18)
	Q_2	–	0.1005(20)	0.1435(16)	0.0827(14)	0.1295(10)
β_c	Q_1	–	6.04140(69)	6.32203(26)	6.04181(41)	6.32207(35)
	Q_2	–	6.04068(74)	6.32172(27)	6.04159(55)	6.32174(24)
a_c	Q_1	–	0.086814 fm	0.056980 fm	0.086755 fm	0.056977 fm
	Q_2	–	0.086919 fm	0.057005 fm	0.086787 fm	0.057003 fm
T_c	Q_1	–	568.24 MeV	577.18 MeV	568.63 MeV	577.21 MeV
	Q_2	–	567.56 MeV	576.93 MeV	568.42 MeV	576.95 MeV

temporal extent of the lattice, so that the numbers in physical units stay (roughly) constant. Indeed, the temperatures at the critical point computed in this way are very comparable for $N_\tau = 4$ and $N_\tau = 6$. On the way to the continuum, one would expect the critical temperature to decrease: The literature value for pure gauge theory there is around 270 MeV [4], and shrinks even more when switching on fermions. This is in contrast to the observations made in this thesis, with T_c rising slightly from $N_\tau = 4$ to $N_\tau = 6$. On the other hand, the increase is so small that it might well be explained by statistical uncertainties. Moreover, both numbers are entirely compatible with the pure gauge results obtained in [18] using just the static determinant and the λ_1 gauge action. These suggest that a noticeable drop in T_c only sets in for even larger $N_\tau \gtrsim 8$.

Another possibility to examine the trend in the critical temperature is to compare the values of κ_c . One finds $\kappa_c(N_\tau=6)/\kappa_c(N_\tau=4) = 1.434(47)$ for Q_1 and $1.428(44)$ for Q_2 , respectively. In the limit $am_q \gg 1$, the critical hopping parameter is approximately proportional to $\kappa_c \sim (a_c m_q)^{-1} = N_\tau T_c / m_q$. Consequently, if the physical parameters are constant, one anticipates above ratio being exactly $3/2$ [22], which is almost covered by the errors. Besides, the results for the critical hopping parameter κ_c both at $N_\tau = 4$ and $N_\tau = 6$ are well below the chiral critical

hopping parameter at the corresponding critical gauge coupling $\kappa_{\text{ch}}(u_c)$ estimated in [18]. This is required by self-consistency, because κ_{ch} is defined by the vanishing of the (renormalised) quark mass [3], but the effective theory is expanding around heavy quarks.

3.6.4. The critical point of the two-flavour theory to $\mathcal{O}(\kappa^4)$

Even more interesting than the case of one flavour, which has been studied in the previous subsection, is the effective theory with two degenerate quark flavours: It can be related to QCD with degenerate up- and down-quarks. This particular model shall be investigated in the following. Again, two different values of N_τ are taken into consideration.

Results for $N_\tau = 4$

In the simulations at $N_\tau = 4$, at least $3 \cdot 10^6$ sweeps over the volume were performed for each combination of the couplings and the system size. The results of the analysis can again be found in table 3.1 and the corresponding plots in appendix A.6.3. Like for the one-flavour theory, the numbers deduced from the two different observables all fit with each other. Judging by the value of f_0 and the quality of the fit, the analysis based on Q_2 is here apparently the more dependable one.

A comparison of the results for the critical point in the two-flavour theory with those for one flavour reveals that $h_{1,c}$ and accordingly κ_c are lowered by the inclusion of another flavour. This can be understood as follows: A larger number of flavours means that there are more fields which break the centre symmetry explicitly (cf. section 3.4). Therefore, if the number of flavours rises, the hopping parameter for each flavour can be somewhat smaller to achieve the same physical effect for the total system. In the gauge couplings at the critical point, by contrast, no significant difference between one and two flavours can be seen, since the gauge sector has been left unchanged. Also the physical temperatures at the critical point are very comparable. Because N_τ is the same for both simulations, this necessarily holds for the lattice spacings as well.

The critical point of two-flavour QCD has been examined with a very similar effective theory in [22]. There, the exact gauge action was employed in a four-dimensional simulation, and for the fermionic part the leading-order and next-to-leading-order terms of the hopping expansion were taken into account. Their result for κ_c is with 0.0640(10) of the same order of magnitude as the one obtained in this thesis. In the precise numbers, however, there is a substantial disagreement, with our value being larger. This can be explained by the impact of the $\mathcal{O}(\kappa^4)$ -corrections, which we have found to weaken the overall influence of fermions. Consequently, a larger hopping parameter is needed in comparison with [22] for the same physical effect.

Results for $N_\tau = 6$

In the simulations at $N_\tau = 6$, at least $3 \cdot 10^6$ sweeps over the volume were performed for each combination of the couplings and the system size at $N_s = 16$ and 24, and at least $6 \cdot 10^6$ at $N_s = 32$. The results of the analysis are collected in table 3.1, as before, and the associated plots in appendix A.6.4. The quantities calculated from the two observables Q_1 and Q_2 are again roughly consistent with each other. Like for the majority of the studies discussed so far, Q_2 presumably yields the more reliable results here, if one judges by the value of f_0 and the

3. Numerical results

quality of the fit. This seems to be a general tendency, as the only exception observed in this thesis is the one-flavour theory with $N_\tau = 4$, where Q_1 gave the better estimates.

Similar to the case of $N_\tau = 4$, $h_{1,c}$ and κ_c are diminished significantly by the introduction of another flavour also at $N_\tau = 6$. The critical gauge couplings and the quantities deduced from them (the lattice spacing and the temperature), on the other hand, are almost identical to the ones in the one-flavour theory. If one compares the result for κ_c with the one obtained in [22] using a next-to-leading-order expansion of the quark determinant, 0.1202(19), one notices a considerable difference. Yet, the fact that our numbers are again the larger ones is in concordance with the resolution given above in terms of the $\mathcal{O}(\kappa^4)$ -corrections.

As was done in the one-flavour theory, one can now assess the trend in the critical temperature from the evolution of κ_c with N_τ . Here, one finds $\kappa_c(N_\tau=6)/\kappa_c(N_\tau=4) = 1.536(44)$ for Q_1 and 1.566(39) for Q_2 , respectively. This is compatible with the theoretical value of $3/2$, indicating that the temperature at the critical point is independent of N_τ . Hence, the findings in the effective theory with two degenerate quark flavours are in qualitative agreement with those at $N_f = 1$.

Finally, the critical point of the effective theory can be compared with recent results from full Lattice QCD at $N_f = 2$ and $N_\tau = 6$ [23]. There, the critical gauge coupling is with $\beta_c = 5.8821$ around 8% smaller than in the thesis at hand. Such a deviation in the gauge sector has already been observed by earlier studies of the effective theory [8]. As a consequence, the lattice spacings in full Lattice QCD are substantially larger and the respective temperatures lower than the ones computed in table 3.1.

For the critical hopping parameter, [23] reports $\kappa_c = 0.0877(9)$, so that the value obtained from the effective theory with the $\mathcal{O}(\kappa^4)$ -corrections is off by about 48%. Even more troublesome is the fact that the $\mathcal{O}(\kappa^4)$ -corrections were found to increase κ_c , although it was already larger than in full Lattice QCD at lower orders in the hopping expansion, and sank from the leading to the next-to-leading order [22]. Excluding for the moment that there could be – in spite of extensive cross-checks of the analytical derivation as well as the numerical implementation – still a problem with the code, there only appear to be two plausible explanations for this unexpected development: Either the results of the hopping expansion will improve at higher orders. This would mean that the sequence of the partial sums of the hopping series is not monotonous. However, such a behaviour is not anticipated, since the hopping expansion consists of the expansion of a logarithm and an exponential (cf. eqs. (2.45), (2.52) and (2.53)). For $\kappa > 0$, both of them have a monotonous sequence of partial sums. Or the hopping expansion will continue to deteriorate at higher orders. In this case, it may converge to a wrong limit, or not be convergent at all. The most probable reason for this to occur would be that the values for κ_c in table 3.1 already lie outside the radius of convergence of the series. In order to judge the radius of convergence of the $\mathcal{O}(\kappa^4)$ -action, the $\mathcal{O}(\kappa^6)$ -action is needed, an effort towards the derivation of which is made in chapter 4. Because the method used in the present thesis to localise the critical point does not include an extrapolation to the thermodynamic limit, finite size effects – which usually enlarge κ_c [22] – may also play a role. Still, they should not alter the overall direction of the shift introduced by the $\mathcal{O}(\kappa^4)$ -terms. In any event, one can conclude that the effective theory truncated at $\mathcal{O}(\kappa^4)$ is not suited to accurately determine the critical point of QCD with two degenerate quark flavours.

3.7. Range of validity of the large- N_τ approximation

The kinetic quark determinant derived and implemented so far is quite complicated, although it is truncated at $\mathcal{O}(\kappa^4)$. A considerable simplification of the action has been observed in [7, 24] in the limit of large N_τ . In [24], even the complete $\mathcal{O}(\kappa^6)$ - and $\mathcal{O}(\kappa^8)$ -corrections to the effective action have been derived taking this limit and $\bar{h}_1 \rightarrow 0$. The resulting expressions were found to be still shorter than the non-approximated $\mathcal{O}(\kappa^4)$ -action listed in appendix A.4. This remarkable simplification happens when one splits the temporal sums into the different combinations of mutually equal temporal coordinates prior to the integration over the spatial links. In the limit of large N_τ , one neglects all particle configurations except for those where only one quark and one antiquark, that is one single meson, hop simultaneously. For a fixed order in κ , this corresponds to dismissing all terms which are of subleading order in N_τ . Only those terms which have the maximal number of unequal temporal coordinates which is allowed by the gauge integration are taken into account.

In [7, 24], this approximation was justified by studying the low-temperature regime. Evidently, it would be highly advantageous if the action shortened in such a way could be applied independent of the temperature under consideration. In principle, $N_\tau \rightarrow \infty$ is also reached by taking the continuum limit eq. (2.16), which constitutes the physically relevant limit. Yet, a large amount of care is required if one wants to determine the correct continuum limit of a theory. Specifically, it has to be established which quantities are supposed to be kept constant while sending $N_\tau \rightarrow \infty$ so as not to change the physics. Here, the temperature and the pion (or the baryon) mass have to be fixed [7]. This however implies that the quark and antiquark couplings h_1 and \bar{h}_1 appearing in the $W_{n_1 m_1 n_2 m_2 s}$ (cf. eq. (2.58)), which are the building blocks of the kinetic quark determinant, are not necessarily constant. On the contrary, they also depend on N_τ , and that in a quite non-obvious way. This could well jeopardise the validity of the aforementioned approximation for finite T in the continuum limit. The objective of the present section is therefore to find out which of the terms that are of subleading order in N_τ can really be dropped in above limit, and how large N_τ has to be in order to justify this.

To that end, all $\mathcal{O}(\kappa^4)$ -terms of the resummed action have been implemented in `Python`, without the transformation to Polyakov loops from section 2.8. Instead, only the summand for one specific \mathbf{x} is examined for each term, and the $SU(3)$ -matrices W at all spatial lattice sites which are involved in the respective interaction are chosen randomly. After creating 1000 such random configurations, the maximal relative contribution of each part of the term is computed. The whole process is repeated for several different values of N_τ . In this way, one can make a statement about how the relative importance of the different parts evolves with growing N_τ . Taking the maximal value instead of the mean ensures that the results are valid independent of the W s, and not only on average.

For the generation of random $SU(3)$ -matrices, the representation presented in [4] is adopted. First, two complex 3-vectors \mathbf{u} and \mathbf{v} are selected according to a uniform random distribution. After orthonormalising them via

$$\tilde{\mathbf{u}} = \frac{\mathbf{u}}{|\mathbf{u}|}, \quad \tilde{\mathbf{v}} = \frac{\mathbf{v} - \tilde{\mathbf{u}}(\tilde{\mathbf{u}} \cdot \mathbf{v})}{|\mathbf{v} - \tilde{\mathbf{u}}(\tilde{\mathbf{u}} \cdot \mathbf{v})|}, \quad (3.46)$$

a matrix $W \in SU(3)$ can be obtained as [4]

$$W = \begin{pmatrix} \tilde{\mathbf{u}} \\ \tilde{\mathbf{v}} \\ \tilde{\mathbf{u}}^* \times \tilde{\mathbf{v}}^* \end{pmatrix}. \quad (3.47)$$

3. Numerical results

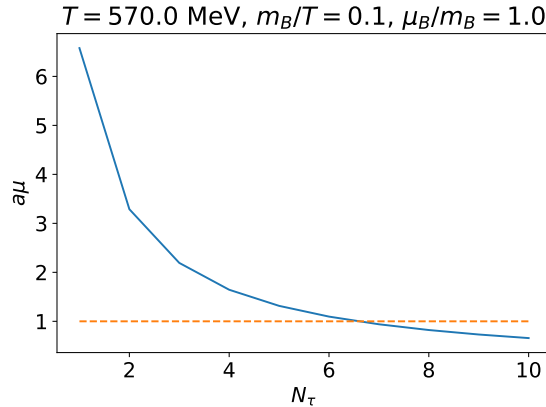


Figure 3.14.: Chemical potential in lattice units as a function of N_τ for constant baryon chemical potential $\mu_B = m_B = 0.1T = 57 \text{ MeV}$

Here, $\mathbf{u} \cdot \mathbf{v} = \sum_{i=1}^3 u_i^* v_i$ is the inner product of the complex vectors \mathbf{u} and \mathbf{v} , and $(\mathbf{u} \times \mathbf{v})_i = \sum_{j,k=1}^3 \epsilon_{ijk} u_j v_k$ their cross product.

As discussed above, the temperature and the baryon mass have to be fixed in order to study the continuum limit. The temperature is chosen as 570 MeV, which is near the critical temperature observed in table 3.1. For each value of N_τ under consideration, the corresponding lattice spacing is calculated as $a = 197.3269804593024659 \text{ MeV fm}/TN_\tau$. A numerical inversion of eq. (3.43) then yields β . The baryon mass in lattice units is given by [7]

$$am_B = \ln \left[\frac{(2\kappa)^{-3} ((2\kappa)^{-3} - 2)}{(2\kappa)^{-3} - 5/4} \right] - 18\kappa^2 \frac{u}{1-u}. \quad (3.48)$$

If one sets $m_B/T = am_B N_\tau / 197.3269804593024659 \text{ MeV fm} = 0.1$ and numerically inverts eq. (3.48), one can thus compute κ . Here, m_B/T has again been taken close to its value at the critical point (cf. table 3.1). For zero chemical potential, one has $h_1 = \bar{h}_1$, which induces some further simplifications: The real parts of some of the expressions vanish in this case. However, only the real parts are taken into account here, since they are the relevant ones for the updates eq. (3.11) in the Metropolis algorithm. In order not to falsely attribute the vanishing of such terms to the limit $N_\tau \rightarrow \infty$, when it is really due to $\mu = 0$, a finite chemical potential should be adopted for the following investigations. Because of the silver blaze property, the physical quantities are independent of the chemical potential before the onset. This happens at $\mu_B < m_B$ as a consequence of the existence of a finite binding energy [7]. Hence, $\mu_B = m_B$ is the smallest option which still guarantees a significant impact of the chemical potential. As can be seen from fig. 3.14, this choice of parameters corresponds to a chemical potential in lattice units which is smaller than 1 for $N_\tau \geq 7$. For the majority of the N_τ -values under consideration, the physics is therefore not strongly influenced by lattice saturation. Regarding the number of flavours, no particular care is required; $N_f = 1$ suffices to demonstrate the behaviour of the different terms with N_τ .

The plots resulting from the analysis described above can be found in appendix A.7. In fig. A.17 the different parts of eq. (A.34) are shown. Here, term 1 refers to the summand which is proportional to h_{3_1} and thus to $N_\tau(N_\tau - 1)$. Term 2 and term 3 are the second and third summand in eq. (A.34), respectively, which are both proportional to h_{3_2} and thus to N_τ .

These two terms become insignificant in the limit $N_\tau \rightarrow \infty$, and the asymptotically relevant contribution comes only from term 1. Additionally plotted is term 1 again with $N_\tau(N_\tau - 1)$ replaced by N_τ^2 , or, more precisely, $h_{3_1} \rightarrow h_2^2$. This is always a valid approximation for large N_τ , because the rest of the term is the same for both of the two factors N_τ^2 and N_τ . Consequently, the component proportional to N_τ can safely be neglected, independent of the behaviour of the remaining factors. The corresponding curve in fig. A.17 confirms this, as it converges towards the curve for the ‘full’ term 1.

The different pieces of the resummed version of eq. (A.35) are presented in fig. A.18. Here, term 1 is the counterterm from the resummation (cf. eq. (2.63)), which is $\propto h_{3_1}/N_{\tau-1} \propto N_\tau$. Term 2 denotes the rest of the part which is proportional to h_{3_1} . This is expected to be the leading contribution for large N_τ , since it is proportional to $N_\tau(N_\tau - 1)$. Term 3 and term 4 name the two summands in eq. (A.35) which are proportional to h_{3_2} and hence to N_τ . Also here, the aforementioned assumption is fulfilled, and terms 1, 3 and 4 become negligible for growing N_τ . Likewise, the legitimacy of the approximation $h_{3_1} \rightarrow h_2^2$ for the leading term 2 is corroborated by the data in fig. A.18.

The two summands of the linear three-point interaction eq. (A.36) are plotted in fig. A.19. In contrast to the two two-point interactions discussed above, here term 2, the prefactor of which is of subleading order in N_τ , cannot be neglected for any N_τ . Conversely, for large N_τ the ratio of the two terms becomes constant, with term 1 contributing about 17.5% and term 2 about 82.5%. Taking a closer look at eq. (A.36), this can be understood in the following way: The factor $W_{1111}^-(\mathbf{x})W_{1111}^-(\mathbf{x} + 2\hat{i})$ appears in both terms and therefore cancels in their fractions of the total real part. The remaining factors differ, but their behaviour strongly depends on the one of h_1 and \bar{h}_1 for increasing N_τ . As can be seen from the left side of fig. 3.15, κ converges to a finite value smaller than $1/2$ for $N_\tau \rightarrow \infty$. Because $h_1 \propto \exp[N_\tau \ln(2\kappa)]$, this makes h_1 approach zero exponentially for large N_τ ; the same holds for \bar{h}_1 . Consequently, all parts of the remaining factors in eq. (A.36) which are proportional to h_1 or \bar{h}_1 will give a vanishing contribution to aforementioned fractions for $N_\tau \rightarrow \infty$. Both term 1 and term 2 have one summand for which this is not the case, $W_{1010}(\mathbf{x} + \hat{i})$ and $4N_c$, respectively, and the two of them come with a prefactor of N_τ . This explains the constant ratio of term 1 and term 2 for large N_τ . Furthermore, the right side of fig. 3.15 displays both the leading-order approximation eq. (2.41) for h_1 and the relation including some gauge corrections eq. (A.7). These gauge corrections weaken the exponential decay of h_1 , but since only a finite number of them are taken into account, the exponential ultimately gains the upper hand. For this reason, above observations might just be due to insufficient gauge corrections in h_1 . This can however not be judged within the framework of the thesis at hand, which relies on the expressions collated in appendix A.1.

The corner-like three-point interaction eq. (A.37) shows a similar yet distinct trend (cf. fig. A.20). Here, term 1, which would naively be supposed to be the dominant one, actually becomes irrelevant for large N_τ , whereas term 2, which is of parametrically lower order in N_τ , prevails. Once again, the common factor $W_{1111}^-(\Gamma_{\bullet\leftarrow})W_{1111}^-(\Gamma_{\rightarrow\bullet})$ drops out of the fractions of the total real part. Contrary to the linear three-point interaction, term 1 has here no contribution which survives when h_1 tends to zero exponentially. Term 2, on the other hand, still has the summand $4N_c$ in its remaining factor and is thus the predominant one in this limit. A closer examination of the derivation of the kinetic quark determinant reveals that the constant $4N_c$ in term 2 stems from a trace of A . It is due to the identity matrix, which is contained in the diagonal part of A , but not of B (cf. eq. (2.48)). For the two-point interaction, the Dirac trace only leaves B_s , as will be proved in section 4.1. This clarifies why the terms with a prefactor of subleading order in N_τ eventually become unimportant in the two-point interactions, but not

3. Numerical results

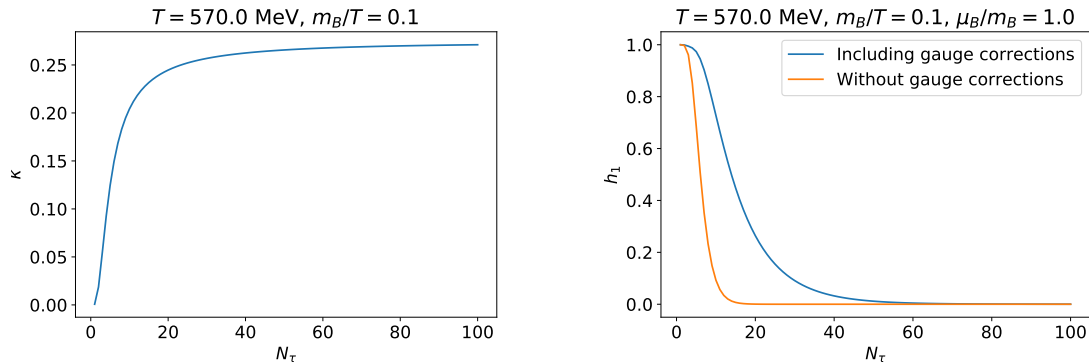


Figure 3.15.: The fermionic couplings κ and h_1 as a function of N_τ for constant temperature $T = 570$ MeV and baryon mass $m_B = 0.1T$ at $\mu_B = m_B$

in the other ones. Nevertheless, the validity of the approximation $h_{3_1} \rightarrow h_2^2$ for term 1 can be confirmed for both three-point interactions.

The four-point interaction eq. (A.39) has an overall prefactor of $h_{3_4} \propto N_\tau$. It is therefore not instructive to contrast the relative contributions of different pieces of it. In spite of this, it is interesting to see whether the N_τ -dependence of the rest of the term is such that eq. (A.39) becomes negligible in comparison with terms proportional to N_τ^2 . Accordingly, eq. (A.39) has been divided by $\kappa^4 N_\tau^2 / N_c^2$, and the result evaluated on 1000 random configurations, as explained above. The maximum of the absolute real part of this is plotted in fig. A.21. The fact that this curve tends to zero as $1/N_\tau$ permits the conclusion that the four-point interaction is indeed irrelevant for large N_τ .

In summary, it can be stated that not all $\mathcal{O}(\kappa^4)$ -terms which are of parametrically subleading order in N_τ can be dropped in the continuum limit. The reason for this is that h_1 and \bar{h}_1 are not fixed, but vanishing exponentially for $N_\tau \rightarrow \infty$. Even for those terms which finally become insignificant, the approximation is justified only for $N_\tau \gtrsim 30$ to 50. This is roughly in concordance with the findings in [7], which indicate that the low-temperature approximation gives a result better than 2% for $N_\tau \geq 50$. Consequently, the anticipated simplification of the action is not applicable for the N_τ -values used in this thesis (4 and 6). There are, however, some reservations about these statements. On the one hand, as has already been considered, the gauge corrections soften the exponential decay of h_1 . It is not clear how the inclusion of even higher corrections in h_1 would change the results of the analysis. On the other hand, the function (3.43) employed to compute β from the lattice spacing is only valid for $\beta < 6.92$, but yields already $\beta \approx 6.96$ at $N_\tau = 14$, and $\beta \approx 7.84$ at $N_\tau = 100$. As alternatives to eq. (3.43) are not easy to be found, also the influence of this systematic error remains uncertain.

4. Higher-order corrections to the nearest-neighbour fermion interaction

The aim of this chapter is to derive higher orders of the hopping parameter expansion of the quark determinant. As the corrections up to $\mathcal{O}(\kappa^4)$ are already known, we will proceed with the calculation of the $\mathcal{O}(\kappa^6)$ -contribution. Here, only the interaction between nearest-neighbouring sites on the spatial lattice shall be studied. This corresponds to the factor with $s_0 = 2$ in the spatial loop expansion eq. (2.52).

To start with, the determinant in this formula has to be expressed in terms of traces. Applying either a trace-log expansion according to eq. (2.53) or using the LeVerrier-Fadeev algorithm to compute the coefficients in eq. (2.56) yields up to the desired order:

$$\begin{aligned} \det_{c,d,t} \left(\mathbb{1} - \kappa^2 \tilde{M}_{C_2} \right)^{N_f} &= 1 - N_f \kappa^2 \text{tr}_{c,d,t} \left(\tilde{M}_{C_2} \right) + \frac{\kappa^4}{2} \left(N_f^2 \text{tr}_{c,d,t}^2 \left(\tilde{M}_{C_2} \right) - N_f \text{tr}_{c,d,t} \left(\tilde{M}_{C_2}^2 \right) \right) \\ &\quad - \frac{\kappa^6}{6} \left(N_f^3 \text{tr}_{c,d,t}^3 \left(\tilde{M}_{C_2} \right) - 3N_f^2 \text{tr}_{c,d,t} \left(\tilde{M}_{C_2} \right) \text{tr}_{c,d,t} \left(\tilde{M}_{C_2}^2 \right) \right. \\ &\quad \quad \left. + 2N_f \text{tr}_{c,d,t} \left(\tilde{M}_{C_2}^3 \right) \right) \\ &\quad + \mathcal{O}(\kappa^8). \end{aligned} \tag{4.1}$$

The task is now to explicitly perform the remaining steps outlined in section 2.5.2 for every one of these terms.

4.1. The Dirac trace

The first issue one needs to address is the Dirac trace. For this purpose, a more specific form of above traces is required. All the powers of \tilde{M}_{C_2} appearing in eq. (4.1) can be written in terms of S^\pm and $(\mathbb{1} - \kappa T)^{-1}$: The definition of the loop matrices eq. (2.51) implies that

$$\tilde{M}_{C_2} = S_{\mathbf{x}, \mathbf{x}+\hat{i}}^+ (\mathbb{1} - \kappa T)_{\mathbf{x}+\hat{i}}^{-1} S_{\mathbf{x}+\hat{i}, \mathbf{x}}^- (\mathbb{1} - \kappa T)_{\mathbf{x}}^{-1} \tag{4.2}$$

for the path C_2 which connects \mathbf{x} and $\mathbf{x}+\hat{i}$. This equation can be plugged into the relevant traces of powers of \tilde{M}_{C_2} . The Dirac structure of the resulting expressions is dictated by eqs. (2.37), (2.38) and (2.47), that is

$$S_i^\pm \propto \mathbb{1} \mp \gamma_i, \quad (\mathbb{1} - \kappa T)^{-1} \propto \mathbb{1} A + \gamma_4 B, \tag{4.3}$$

where A and B are no longer matrices in spin space. It turns out that solely by means of these relations and the properties of the Euclidean Dirac matrices, the Dirac traces for the nearest-neighbour interaction can be evaluated in general. Suppressing the colour and space-time

4. Higher-order corrections to the nearest-neighbour fermion interaction

indices for the moment, one has

$$\begin{aligned}
\text{tr}_d \left(\tilde{M}_{C_2}^k \right) &\sim \text{tr}_d \left\{ [(\mathbb{1} - \gamma_i)(\mathbb{1}A_1 + \gamma_4 B_1)(\mathbb{1} + \gamma_i)(\mathbb{1}A_2 + \gamma_4 B_2)]^k \right\} \\
&= \text{tr}_d \left\{ [(\mathbb{1}A_1 - \gamma_i A_1 + \gamma_4 B_1 - \gamma_i \gamma_4 B_1)(\mathbb{1}A_2 + \gamma_i A_2 + \gamma_4 B_2 + \gamma_i \gamma_4 B_2)]^k \right\} \\
&= \text{tr}_d \left\{ [\mathbb{1}A_1 A_2 + \gamma_4 A_1 B_2 - \gamma_i \gamma_i A_1 A_2 - \gamma_i \gamma_i \gamma_4 A_1 B_2 + \gamma_4 B_1 A_2 + \gamma_4 \gamma_i B_1 A_2 \right. \\
&\quad \left. + \gamma_4 \gamma_4 B_1 B_2 + \gamma_4 \gamma_i \gamma_4 B_1 B_2 - \gamma_i \gamma_4 B_1 A_2 - \gamma_i \gamma_4 \gamma_i B_1 A_2 - \gamma_i \gamma_4 \gamma_4 B_1 B_2 \right. \\
&\quad \left. - \gamma_i \gamma_4 \gamma_i \gamma_4 B_1 B_2]^k \right\} \quad (4.4)
\end{aligned}$$

Here, the index i specifies the spatial orientation of the loop C_2 , and is never summed over. By employing the anticommutator of the Euclidean Dirac matrices, $\{\gamma_4, \gamma_i\} = \gamma_4 \gamma_i + \gamma_i \gamma_4 = 0$ and $\gamma_\mu^2 = 1/2\{\gamma_\mu, \gamma_\mu\} = \mathbb{1}$, one realises that many of the terms in eq. (4.4) are actually identical. Hence, the result simplifies to

$$\begin{aligned}
\text{tr}_d \left(\tilde{M}_{C_2}^k \right) &\sim \text{tr}_d \left\{ [2(\mathbb{1}B_1 B_2 - \gamma_i B_1 B_2 + \gamma_4 \gamma_i B_1 A_2 + \gamma_4 B_1 A_2)]^k \right\} \\
&= 2^k \text{tr}_d \left\{ [(\mathbb{1} - \gamma_i)B_1 B_2 + \gamma_4(\mathbb{1} + \gamma_i)B_1 A_2]^k \right\}. \quad (4.5)
\end{aligned}$$

After expanding the k -th power inside the trace, the second term (the one which is proportional to $\gamma_4(\mathbb{1} + \gamma_i)$) can finally be found

- alone. This vanishes because $\text{tr}_d(\gamma_4(\mathbb{1} + \gamma_i)) = 0$.
- multiplied with itself (one or more times). This vanishes because $\gamma_4(\mathbb{1} + \gamma_i)\gamma_4(\mathbb{1} + \gamma_i) = (\mathbb{1} - \gamma_i)(\mathbb{1} + \gamma_i) = 0$.
- multiplied with $(\mathbb{1} - \gamma_i)$ from the right. This vanishes because $\gamma_4(\mathbb{1} + \gamma_i)(\mathbb{1} - \gamma_i) = 0$.
- multiplied with $(\mathbb{1} - \gamma_i)$ from the left. Since $(\mathbb{1} - \gamma_i)\gamma_4(\mathbb{1} + \gamma_i) = \gamma_4(\mathbb{1} + \gamma_i)(\mathbb{1} + \gamma_i) = 2\gamma_4(\mathbb{1} + \gamma_i)$, this case simply reproduces the second term from eq. (4.5) with an additional prefactor of 2. This eventually also vanishes by induction and the other three cases.

Consequently, the second term in eq. (4.5) never contributes anything after evaluating the Dirac trace. Regarding the first term, one notes that $(\mathbb{1} - \gamma_i)^k = 2^{k-1}(\mathbb{1} - \gamma_i)$ and $\text{tr}_d \gamma_i = 0$, so that the ultimate result is

$$\text{tr}_d \left(\tilde{M}_{C_2}^k \right) \sim 2^k \text{tr}_d \left\{ [(\mathbb{1} - \gamma_i)B_1 B_2]^k \right\} = 2^{2k-1} N_d (B_1 B_2)^k = 2^{2k+1} (B_1 B_2)^k. \quad (4.6)$$

It has thus been proved that the Dirac trace only leaves B s for the nearest-neighbour interaction.

In order to write down the complete expressions for the traces of powers of \tilde{M}_{C_2} , one needs to adopt the full definitions of the spatial hopping terms and the B s, including all colour, spatial and temporal indices. The last summand of the $\mathcal{O}(\kappa^6)$ -contribution in eq. (4.1), for instance, reads after the evaluation of the Dirac trace

$$\begin{aligned}
\text{tr}_{c,d,t} \left(\tilde{M}_{C_2}^3 \right) &= 2^7 \sum_{x_4, y_4, z_4, a_4, b_4, c_4} U_i(\mathbf{x}, x_4)_{I,J} B_{(\mathbf{x}+\hat{i}, x_4), (\mathbf{x}+\hat{i}, a_4); J, K} U_i^\dagger(\mathbf{x}, a_4)_{K,L} B_{(\mathbf{x}, a_4), (\mathbf{x}, y_4); L, M} \\
&\quad U_i(\mathbf{x}, y_4)_{M,N} B_{(\mathbf{x}+\hat{i}, y_4), (\mathbf{x}+\hat{i}, b_4); N, O} U_i^\dagger(\mathbf{x}, b_4)_{O,P} B_{(\mathbf{x}, b_4), (\mathbf{x}, z_4); P, Q} \\
&\quad U_i(\mathbf{x}, z_4)_{Q,R} B_{(\mathbf{x}+\hat{i}, z_4), (\mathbf{x}+\hat{i}, c_4); R, S} U_i^\dagger(\mathbf{x}, c_4)_{S,T} B_{(\mathbf{x}, c_4), (\mathbf{x}, x_4); T, I}. \quad (4.7)
\end{aligned}$$

Here, x_4, y_4, z_4, a_4, b_4 and c_4 are the temporal indices and the capital letters denote the colour indices, for which the Einstein summation convention applies. The remaining $\mathcal{O}(\kappa^6)$ -terms in eq. (4.1) look similar, but have a different index structure in colour and temporal space.

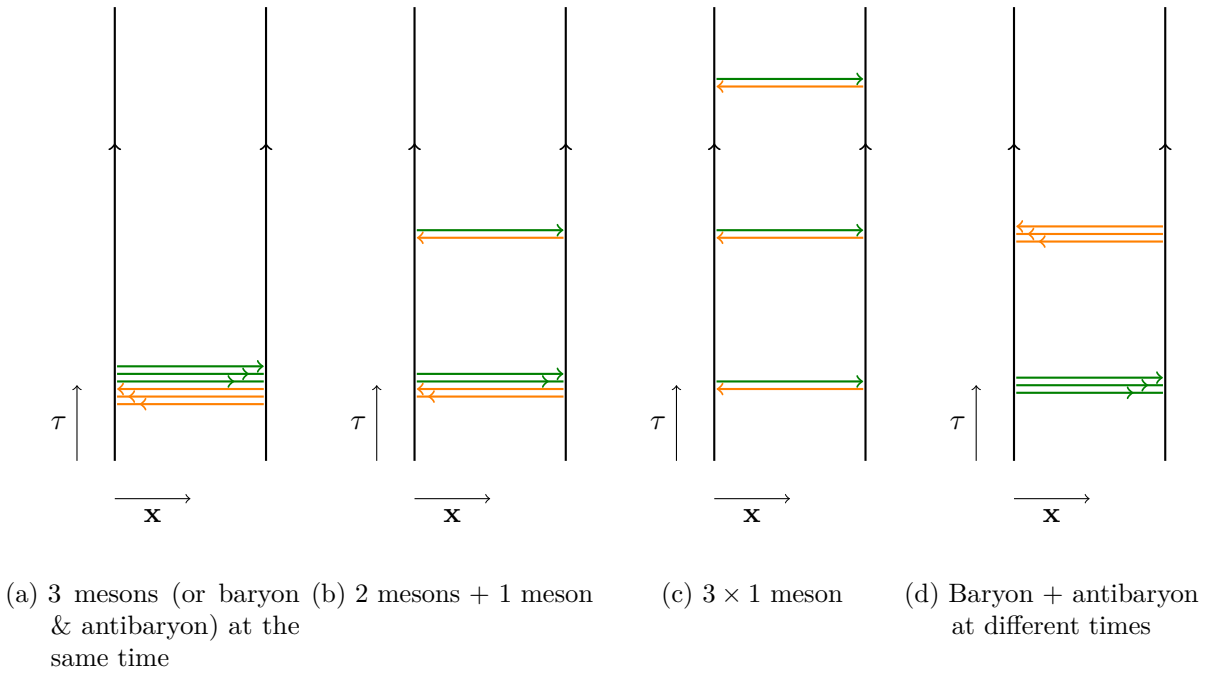


Figure 4.1.: Illustration of the physically distinct particle configurations for the $\mathcal{O}(\kappa^6)$ -contribution to the nearest-neighbour interaction

4.2. Integration over spatial links

The next stage of the procedure described in section 2.5.2 is the integration over the spatial links. Before plugging in the results for the gauge integrals, the temporal sums in expressions like eq. (4.7) need to be split into all combinations of mutually equal temporal coordinates which yield a non-vanishing contribution after gauge integration. In this way, one can figure out which of the links actually lie on top of each other and are hence part of the same integral. Physically, this can be understood as particles hopping between the two lattice sites \mathbf{x} and $\mathbf{x} + \hat{i}$. Figure 4.1 gives an overview over the possible arrangements for the $\mathcal{O}(\kappa^6)$ -contribution: Either all hops happen at the same time, which corresponds to three mesons or one baryon and one antibaryon being interchanged simultaneously (cf. fig. 4.1a). Or one quark- and one antiquark-hop happen at a different time, so that two mesons are exchanged at one time and one meson at a later (or earlier) time (cf. fig. 4.1b). Another option is that all three mesons are interchanged at unequal times (cf. fig. 4.1c). Finally, also three quarks and three antiquarks can be grouped together, which is interpreted as one baryon and one antibaryon being exchanged separately (cf. fig. 4.1d). One has to keep in mind that these are only the four physically distinct cases. For the mathematics, by contrast, all possible permutations of these have to be taken into account, since the individual gauge links possess different colour indices as well.

4. Higher-order corrections to the nearest-neighbour fermion interaction

For the example from eq. (4.7) this means that

$$\begin{aligned}
\int [dU_i] \operatorname{tr}_{c,d,t} \left(\tilde{M}_{C_2}^3 \right) &= 2^7 \int [dU_i] \left\{ \sum_{x_4} (\cdots)_{x_4=a_4=y_4=b_4=z_4=c_4} \right. \\
&+ \sum_{x_4 \neq y_4} \left[(\cdots)_{\substack{x_4=a_4 \\ y_4=b_4=z_4=c_4}} + (\cdots)_{\substack{x_4=b_4 \\ y_4=a_4=z_4=c_4}} \right. \\
&\quad \left. + (\cdots)_{\substack{x_4=c_4 \\ y_4=a_4=b_4=z_4}} + (\cdots)_{\substack{x_4=a_4=b_4=z_4 \\ y_4=c_4}} \right. \\
&\quad \left. + (\cdots)_{\substack{x_4=a_4=c_4=z_4 \\ y_4=b_4}} + (\cdots)_{\substack{x_4=b_4=c_4=z_4 \\ y_4=a_4}} \right] \\
&+ \sum_{x_4 \neq z_4} \left[(\cdots)_{\substack{z_4=a_4 \\ x_4=y_4=b_4=c_4}} + (\cdots)_{\substack{z_4=b_4 \\ x_4=a_4=y_4=c_4}} \right. \\
&\quad \left. + (\cdots)_{\substack{z_4=c_4 \\ x_4=a_4=y_4=b_4}} \right] \\
&+ \sum_{x_4 \neq y_4 \neq z_4} \left[\text{yellow } (\cdots)_{\substack{x_4=a_4 \\ y_4=b_4 \\ z_4=c_4}} + (\cdots)_{\substack{x_4=a_4 \\ y_4=c_4 \\ z_4=b_4}} + (\cdots)_{\substack{x_4=b_4 \\ y_4=c_4 \\ z_4=a_4}} \right. \\
&\quad \left. + (\cdots)_{\substack{x_4=b_4 \\ y_4=a_4 \\ z_4=c_4}} + (\cdots)_{\substack{x_4=c_4 \\ y_4=a_4 \\ z_4=b_4}} + (\cdots)_{\substack{x_4=c_4 \\ y_4=b_4 \\ z_4=a_4}} \right] \\
&\left. + \sum_{\substack{x_4 \neq a_4 \\ a_4=b_4=c_4}} (\cdots)_{\substack{x_4=y_4=z_4 \\ a_4=b_4=c_4}} \right\}. \tag{4.8}
\end{aligned}$$

One can now plug the corresponding results of the gauge integrals over the spatial links from appendix A.2 into each of these terms. Due to the multitude and the length of the expressions, explicit calculations will not be shown for all cases, but only for two typical instances. The term highlighted in **yellow** is one of the six possible permutations of the exchange of three individual mesons (cf. fig. 4.1c). Therefore, the most simple integral eq. (A.18) appears three times, and the result (without the prefactor 2^7) is

$$\begin{aligned}
&\sum_{x_4 \neq y_4 \neq z_4} \left(\int_{\text{SU}(3)} dU U_{I,J} U_{K,L}^\dagger \right) B_{(\mathbf{x}+\hat{i},x_4),(\mathbf{x}+\hat{i},x_4);J,K} B_{(\mathbf{x},x_4),(\mathbf{x},y_4);L,M} \left(\int_{\text{SU}(3)} dU U_{M,N} U_{O,P}^\dagger \right) \\
&\quad B_{(\mathbf{x}+\hat{i},y_4),(\mathbf{x}+\hat{i},y_4);N,O} B_{(\mathbf{x},y_4),(\mathbf{x},z_4);P,Q} \left(\int_{\text{SU}(3)} dU U_{Q,R} U_{S,T}^\dagger \right) B_{(\mathbf{x}+\hat{i},z_4),(\mathbf{x}+\hat{i},z_4);R,S} \\
&\quad B_{(\mathbf{x},z_4),(\mathbf{x},x_4);T,I} \\
&= \sum_{x_4 \neq y_4 \neq z_4} \frac{1}{27} \delta_{I,L} \delta_{J,K} \delta_{M,P} \delta_{N,O} \delta_{Q,T} \delta_{R,S} \left(B_{(\mathbf{x}+\hat{i},x_4),(\mathbf{x}+\hat{i},x_4);J,K} B_{(\mathbf{x},x_4),(\mathbf{x},y_4);L,M} \right. \\
&\quad \left. B_{(\mathbf{x}+\hat{i},y_4),(\mathbf{x}+\hat{i},y_4);N,O} B_{(\mathbf{x},y_4),(\mathbf{x},z_4);P,Q} B_{(\mathbf{x}+\hat{i},z_4),(\mathbf{x}+\hat{i},z_4);R,S} B_{(\mathbf{x},z_4),(\mathbf{x},x_4);T,I} \right) \\
&= \sum_{x_4 \neq y_4 \neq z_4} \frac{1}{27} \operatorname{tr}_c(B(\mathbf{x} + \hat{i}, x_4, x_4)) \operatorname{tr}_c(B(\mathbf{x} + \hat{i}, y_4, y_4)) \operatorname{tr}_c(B(\mathbf{x} + \hat{i}, z_4, z_4)) \\
&\quad \operatorname{tr}_c(B(\mathbf{x}, x_4, y_4) B(\mathbf{x}, y_4, z_4) B(\mathbf{x}, z_4, x_4)) \tag{4.9}
\end{aligned}$$

where the shortened notation $B(\mathbf{x}, x_4, y_4) = B_{(\mathbf{x},x_4),(\mathbf{x},y_4)}$ has been introduced. This demonstrates that the gauge integrals describing an exchange of mesons yield Kronecker δ s, which in turn give traces of B after the contraction of the colour indices. The term highlighted in **blue**

encodes the separate exchange of a baryon and an antibaryon depicted in fig. 4.1d. Here, the integrals from eqs. (A.20) and (A.21) arise, leading to

$$\begin{aligned}
 & \sum_{x_4 \neq a_4} \left(\int_{\text{SU}(3)} dU U_{I,J} U_{M,N} U_{Q,R} \right) \left(\int_{\text{SU}(3)} dU U_{K,L}^\dagger U_{O,P}^\dagger U_{S,T}^\dagger \right) B_{(\mathbf{x}+\hat{i},x_4),(\mathbf{x}+\hat{i},a_4);J,K} \\
 & \quad B_{(\mathbf{x},a_4),(\mathbf{x},x_4);L,M} B_{(\mathbf{x}+\hat{i},x_4),(\mathbf{x}+\hat{i},a_4);N,O} B_{(\mathbf{x},a_4),(\mathbf{x},x_4);P,Q} B_{(\mathbf{x}+\hat{i},x_4),(\mathbf{x}+\hat{i},a_4);R,S} \\
 & \quad B_{(\mathbf{x},a_4),(\mathbf{x},x_4);T,I} \\
 & = \sum_{x_4 \neq a_4} \frac{1}{36} \epsilon_{I,M,Q} \epsilon_{J,N,R} \epsilon_{K,O,S} \epsilon_{L,P,T} \left(B_{(\mathbf{x}+\hat{i},x_4),(\mathbf{x}+\hat{i},a_4);J,K} B_{(\mathbf{x},a_4),(\mathbf{x},x_4);L,M} B_{(\mathbf{x}+\hat{i},x_4),(\mathbf{x}+\hat{i},a_4);N,O} \right. \\
 & \quad \left. B_{(\mathbf{x},a_4),(\mathbf{x},x_4);P,Q} B_{(\mathbf{x}+\hat{i},x_4),(\mathbf{x}+\hat{i},a_4);R,S} B_{(\mathbf{x},a_4),(\mathbf{x},x_4);T,I} \right) \\
 & = \sum_{x_4 \neq a_4} \det_c(B(\mathbf{x} + \hat{i}, x_4, a_4)) \det_c(B(\mathbf{x}, a_4, x_4)). \tag{4.10}
 \end{aligned}$$

It has thus been illustrated that the gauge integrals belonging to an exchange of (anti)baryons yield Levi-Civita ϵ s, which in turn give determinants of B after the contraction of the colour indices.

Proceeding like this for all the other summands in eq. (4.8), and repeating the same steps for the remaining $\mathcal{O}(\kappa^6)$ -terms in eq. (4.1), all gauge integrals over the spatial links can be evaluated. In this way, the $\mathcal{O}(\kappa^6)$ -contribution of the nearest-neighbour interaction to the kinetic quark determinant may be expressed in terms of traces and determinants of powers of B . Above derivation scheme has been automated with `Mathematica` in the context of the present thesis. The basic approach is very similar to the one employed for the calculation by hand: To begin with, the different traces of powers of \tilde{M}_{C_2} which are needed according to eq. (4.1) are written out in terms of B s, generating the suitable temporal and colour index structure. These are immediately equipped with the correct prefactors from eqs. (4.1) and (4.6) to account for the Dirac trace. In the next step, the particle configurations which are allowed by the gauge integration and their permutations are determined. This can be done purely based on the overall set of temporal indices, as each temporal index can be uniquely identified with a spatial gauge link (cf. eq. (4.7)). After having split the temporal sums in this manner, the gauge integrations have to be carried out¹. For each part of the sum, first the resulting colour δ s and ϵ s are contracted with the indices of the B s. Then, their temporal indices are contracted as dictated by the particle configuration. Afterwards, the computer program analyses the final colour index structure of the terms in order to convert the index notation to traces and determinants. Since the contraction of the temporal coordinates does not necessarily leave the ones with the lowest indices, they need to be renamed appropriately. This additionally permits the recognition of some terms that are actually identical, which would not be possible otherwise.

Ultimately, one can exploit further simplifications which are due to the summation over the spatial position \mathbf{x} . Namely, terms that transform into each other under the interchange of \mathbf{x} and $\mathbf{x} + \hat{i}$ give the same contribution. An example of this is

$$\begin{aligned}
 & \sum_{\mathbf{x}} \sum_{\tau_1 \neq \tau_2} \text{tr}_c(B(\mathbf{x} + \hat{i}, \tau_1, \tau_1)) \text{tr}_c(B(\mathbf{x} + \hat{i}, \tau_1, \tau_2) B(\mathbf{x} + \hat{i}, \tau_2, \tau_1)) \\
 & \quad \text{tr}_c(B(\mathbf{x}, \tau_1, \tau_1) B(\mathbf{x}, \tau_1, \tau_2) B(\mathbf{x}, \tau_2, \tau_1)) \\
 & = \sum_{\mathbf{x}} \sum_{\tau_1 \neq \tau_2} \text{tr}_c(B(\mathbf{x}, \tau_1, \tau_1)) \text{tr}_c(B(\mathbf{x}, \tau_1, \tau_2) B(\mathbf{x}, \tau_2, \tau_1)) \\
 & \quad \text{tr}_c(B(\mathbf{x} + \hat{i}, \tau_1, \tau_1) B(\mathbf{x} + \hat{i}, \tau_1, \tau_2) B(\mathbf{x} + \hat{i}, \tau_2, \tau_1)) \tag{4.11}
 \end{aligned}$$

¹For this purpose, a `Mathematica` worksheet provided by Jonas Scheunert is used.

4. Higher-order corrections to the nearest-neighbour fermion interaction

With the exception of terms that are already symmetric under $\mathbf{x} \leftrightarrow \mathbf{x} + \hat{i}$, this spares one from writing half of the expressions. The identification of such opportunities to shorten the final result has been automated as well.

The implementation in `Mathematica` has been tested for the $\mathcal{O}(\kappa^2)$ - and $\mathcal{O}(\kappa^4)$ -contributions, and was found to agree with the results known from [10]. Apart from this, many minor checks were performed for all the intermediary stages of the derivation. After having convinced oneself in this way that the program is indeed working properly, it has been applied to compute the complete $\mathcal{O}(\kappa^6)$ -correction to the nearest-neighbour fermion interaction before the temporal summation. The outcome is shown in appendix A.8 because of the length of the expressions.

4.3. Evaluation of the temporal sums

What remains to be done is the explicit evaluation of the sums over the temporal positions. A full automation of this has not yet been accomplished, so that at least the elementary steps have to be worked out by hand. In the following, we will go through these in detail both for traces and for determinants² of B , and explain how the last step of the summation can still be included in the `Mathematica` implementation.

4.3.1. Traces

As already mentioned in section 2.5.2, the diagonal part of B is independent of the temporal coordinate. Traces which are only made up of such diagonal parts can therefore be pulled in front of the sums and replaced by the appropriate expressions in terms of the $W_{n_1 m_1 n_2 m_2}$ s. The most simple case is

$$\mathrm{tr}(B(\mathbf{x}, \tau, \tau)) = -\frac{1}{2} W_{1111}^-(\mathbf{x}). \quad (4.12)$$

Higher powers of B need to be expanded owing to the sum in $B = B^+ - B^-$ (cf. eq. (2.47)), which results in

$$\mathrm{tr}(B(\mathbf{x}, \tau, \tau)B(\mathbf{x}, \tau, \tau)) = \frac{1}{4} \left(W_{2222}^+(\mathbf{x}) - 2W_{1111}(\mathbf{x}) \right), \quad (4.13)$$

$$\mathrm{tr}(B(\mathbf{x}, \tau, \tau)B(\mathbf{x}, \tau, \tau)B(\mathbf{x}, \tau, \tau)) = \frac{1}{8} \left(-W_{3333}^-(\mathbf{x}) + 3W_{2211}(\mathbf{x}) - 3W_{1122}(\mathbf{x}) \right). \quad (4.14)$$

If a term also contains off-diagonal parts of B , one has to split the temporal sums into all possible arrangements of the temporal coordinates, as was reasoned in section 2.5.2. The easiest case here is the one of $\mathrm{tr}(B(\mathbf{x}, \tau_1, \tau_2)B(\mathbf{x}, \tau_2, \tau_1))$, if all other traces are time-independent. Splitting the sum, plugging in the formula for the off-diagonal part of B (cf. eq. (2.48)), expanding the powers and combining the products of the fractional Wilson lines to whole Wilson lines yields

$$\begin{aligned} & \sum_{\tau_1 \neq \tau_2} \mathrm{tr}(B(\mathbf{x}, \tau_1, \tau_2)B(\mathbf{x}, \tau_2, \tau_1)) \\ &= -\frac{1}{4} \left\{ \sum_{\tau_1 < \tau_2} \left[W_{2121}^+(\mathbf{x}) + \left((2\kappa)^{2(\tau_2 - \tau_1)} + (2\kappa)^{2(N_\tau - (\tau_2 - \tau_1))} \right) W_{1010}(\mathbf{x}) \right] \right. \\ & \quad \left. + \sum_{\tau_1 > \tau_2} \left[W_{2121}^+(\mathbf{x}) + \left((2\kappa)^{2(N_\tau - (\tau_1 - \tau_2))} + (2\kappa)^{2(\tau_1 - \tau_2)} \right) W_{1010}(\mathbf{x}) \right] \right\} \end{aligned} \quad (4.15)$$

²All traces and determinants in this section are taken over colour space.

This shows that the result is the same for both parts of the sum, if in the second part τ_1 is renamed to τ_2 and vice versa. For this reason, it is sufficient to consider the first part, where the sum reads $\sum_{\tau_1 < \tau_2} = \sum_{\tau_1=0}^{N_\tau-1} \sum_{\tau_2=\tau_1+1}^{N_\tau-1}$.

The most involved computation is the one for the prefactor of $W_{1010}(\mathbf{x})$, which solely depends on the difference $\tau = \tau_2 - \tau_1 \in [1, N_\tau - 1]$. Each of these differences occurs $N_\tau - \tau$ times. For instance, there are $N_\tau - 1$ possibilities to pick two coordinates τ_1 and τ_2 with a distance of 1, $N_\tau - 2$ possibilities for a distance of 2, and so on, until only one option remains for a distance of $N_\tau - 1$. The summation can hence be written in terms of this difference, if a prefactor of $N_\tau - \tau$ is introduced in the summand:

$$\begin{aligned} \sum_{\tau_1=0}^{N_\tau-1} \sum_{\tau_2=\tau_1+1}^{N_\tau-1} \left[(2\kappa)^{2(\tau_2-\tau_1)} + (2\kappa)^{2(N_\tau-(\tau_2-\tau_1))} \right] &= \sum_{\tau=1}^{N_\tau-1} \left[(N_\tau - \tau)(2\kappa)^{2\tau} + (N_\tau - \tau)(2\kappa)^{2(N_\tau-\tau)} \right] \\ &= \sum_{\tau=1}^{N_\tau-1} (N_\tau - \tau)(2\kappa)^{2\tau} + \sum_{\tilde{\tau}=1}^{N_\tau-1} \tilde{\tau}(2\kappa)^{2\tilde{\tau}} \\ &= N_\tau \sum_{\tau=1}^{N_\tau-1} (2\kappa)^{2\tau}. \end{aligned} \quad (4.16)$$

Here, in the second summand $N_\tau - \tau = \tilde{\tau}$ has been substituted. The final result for the term in eq. (4.15) is thus

$$\sum_{\tau_1 \neq \tau_2} \text{tr}(B(\mathbf{x}, \tau_1, \tau_2)B(\mathbf{x}, \tau_2, \tau_1)) = -\frac{N_\tau(N_\tau - 1)}{4} \left(W_{2121}^+(\mathbf{x}) + \frac{2}{N_\tau - 1} \sum_{\tau=1}^{N_\tau-1} (2\kappa)^{2\tau} W_{1010}(\mathbf{x}) \right). \quad (4.17)$$

The steps leading from eq. (4.15) to eq. (4.17) can be automated if the approach is slightly adapted. For this purpose, one loops over all permutations \mathcal{P} of the temporal indices involved into the whole term in order to mimic their arrangements. Subsequently, one works on the level of individual traces and handles them independently. An expression of the type $\text{tr}(B(\mathbf{x}, \tau_1, \tau_2)B(\mathbf{x}, \tau_2, \tau_1))$ is then replaced by

$$-\frac{1}{4} \left[W_{2121}^+(\mathbf{x}) + \left((2\kappa)^{2(\tau_{\mathcal{P}(2)} - \tau_{\mathcal{P}(1)})} + (2\kappa)^{2(N_\tau - (\tau_{\mathcal{P}(2)} - \tau_{\mathcal{P}(1)})}) \right) W_{1010}(\mathbf{x}) \right]. \quad (4.18)$$

Traces over diagonal parts of B are written in terms of the $W_{n_1 m_1 n_2 m_2}$ s by means of eqs. (4.12) to (4.14). After multiplying all trace factors, the actual temporal summation is performed, depending on the number of temporal indices contained in the entire term. If only one coordinate is involved, the term merely needs to be multiplied by an overall factor of N_τ . This is because only diagonal parts of B can occur under this condition. For two distinct coordinates, one replaces the difference $\tau_{\mathcal{P}(2)} - \tau_{\mathcal{P}(1)} \rightarrow \tau$ and then sums over it according to $\sum_{\tau=1}^{N_\tau-1} (N_\tau - \tau)$. This includes the correcting prefactor from eq. (4.16). In the end, one has to sum over all permutations \mathcal{P} of the temporal indices.

For the example discussed above, where $\text{tr}(B(\mathbf{x}, \tau_1, \tau_2)B(\mathbf{x}, \tau_2, \tau_1))$ is only multiplied by time-independent traces, this process yields

$$-\frac{1}{2} \sum_{\tau=1}^{N_\tau-1} (N_\tau - \tau) \left[W_{2121}^+(\mathbf{x}) + \left((2\kappa)^{2\tau} + (2\kappa)^{2(N_\tau-\tau)} \right) W_{1010}(\mathbf{x}) \right], \quad (4.19)$$

since the contributions from both permutations are equal (cf. eq. (4.15)). Upon comparison of eqs. (4.16) and (4.17) with eq. (4.19), it becomes apparent that both methods are equivalent.

4. Higher-order corrections to the nearest-neighbour fermion interaction

This statement holds for higher powers of eq. (4.18) as well. As a consequence, it suffices to expand the powers of B and figure out the products of the fractional Wilson lines for each trace by hand. This corresponds to the derivation of eq. (4.15) in the case of $\text{tr}(B(\mathbf{x}, \tau_1, \tau_2)B(\mathbf{x}, \tau_2, \tau_1))$. The multiplication of different trace factors and the final temporal summation can be carried out by the computer.

Another term incorporating two temporal indices which appears in the $\mathcal{O}(\kappa^6)$ -contribution is $\text{tr}(B(\mathbf{x}, \tau_1, \tau_1)B(\mathbf{x}, \tau_1, \tau_2)B(\mathbf{x}, \tau_2, \tau_1))$. Compared to the term studied above, one only needs to multiply another diagonal part of B inside the trace. In the approach employed for the automation, such a term is hence replaced by

$$\frac{1}{8} \left[W_{3232}^-(\mathbf{x}) + W_{1121}(\mathbf{x}) - W_{2111}(\mathbf{x}) + \left((2\kappa)^{2(\tau_{\mathcal{P}(2)} - \tau_{\mathcal{P}(1)})} + (2\kappa)^{2(N_\tau - (\tau_{\mathcal{P}(2)} - \tau_{\mathcal{P}(1)}))} \right) (W_{2110}(\mathbf{x}) - W_{1021}(\mathbf{x})) \right] \quad (4.20)$$

If there are three distinct temporal indices, the sum has to be split into six parts, corresponding to all possible arrangements:

$$\sum_{\tau_1 \neq \tau_2 \neq \tau_3} = \sum_{\tau_1 < \tau_2 < \tau_3} + \sum_{\tau_1 < \tau_3 < \tau_2} + \sum_{\tau_2 < \tau_3 < \tau_1} + \sum_{\tau_2 < \tau_1 < \tau_3} + \sum_{\tau_3 < \tau_1 < \tau_2} + \sum_{\tau_3 < \tau_2 < \tau_1} . \quad (4.21)$$

Here, the number of descents in $(\tau_1, \tau_2, \tau_3, \tau_1)$ can be either one or two, depending on the sign of the permutation. This leads to two distinguishable results for a trace containing three temporal indices. For a positive permutation of $\{\tau_1, \tau_2, \tau_3\}$, one has for example

$$\begin{aligned} & \sum_{\tau_1 < \tau_2 < \tau_3} \text{tr}(B(\mathbf{x}, \tau_1, \tau_2)B(\mathbf{x}, \tau_2, \tau_3)B(\mathbf{x}, \tau_3, \tau_1)) \\ &= -\frac{1}{8} \sum_{\tau_1 < \tau_2 < \tau_3} \left[W_{3100}(\mathbf{x}) + W_{0032}(\mathbf{x}) + \left((2\kappa)^{2(\tau_3 - \tau_1)} + (2\kappa)^{2(N_\tau - (\tau_3 - \tau_2))} + (2\kappa)^{2(N_\tau - (\tau_2 - \tau_1))} \right) W_{2010}(\mathbf{x}) \right. \\ & \quad \left. + \left((2\kappa)^{2(N_\tau - (\tau_3 - \tau_1))} + (2\kappa)^{2(\tau_2 - \tau_1)} + (2\kappa)^{2(\tau_3 - \tau_2)} \right) W_{1021}(\mathbf{x}) \right] \end{aligned} \quad (4.22)$$

and for a negative permutation

$$\begin{aligned} & \sum_{\tau_1 < \tau_3 < \tau_2} \text{tr}(B(\mathbf{x}, \tau_1, \tau_2)B(\mathbf{x}, \tau_2, \tau_3)B(\mathbf{x}, \tau_3, \tau_1)) \\ &= \frac{1}{8} \sum_{\tau_1 < \tau_3 < \tau_2} \left[W_{3200}(\mathbf{x}) + W_{0031}(\mathbf{x}) + \left((2\kappa)^{2(N_\tau - (\tau_3 - \tau_1))} + (2\kappa)^{2(\tau_2 - \tau_1)} + (2\kappa)^{2(N_\tau - (\tau_2 - \tau_3))} \right) W_{1020}(\mathbf{x}) \right. \\ & \quad \left. + \left((2\kappa)^{2(\tau_3 - \tau_1)} + (2\kappa)^{2(\tau_2 - \tau_3)} + (2\kappa)^{2(N_\tau - (\tau_2 - \tau_1))} \right) W_{2110}(\mathbf{x}) \right] \end{aligned} \quad (4.23)$$

For the remaining permutations from eq. (4.21) these relations also apply, with the temporal coordinates renamed appropriately.

The most difficult computations are again the ones for the prefactors consisting of powers of 2κ . For the purpose of writing the sums in terms of the differences $\tau = \tau_2 - \tau_1$ and $\tau' = \tau_3 - \tau_2$ (for $\tau_1 < \tau_2 < \tau_3$), one needs to introduce a prefactor of $N_\tau - \tau - \tau'$ in the summand. It accounts for the different number of possibilities to choose three temporal indices with the

specified distances. The prefactor of $W_{2010}(\mathbf{x})$ in eq. (4.22) then becomes

$$\begin{aligned}
 & \sum_{\tau=1}^{N_\tau-2} \sum_{\tau'=1}^{N_\tau-\tau-1} (N_\tau - \tau - \tau') \left((2\kappa)^{2(\tau+\tau')} + (2\kappa)^{2(N_\tau-\tau')} + (2\kappa)^{2(N_\tau-\tau)} \right) \\
 &= \sum_{\tau=1}^{N_\tau-2} \sum_{\tilde{\tau}=1}^{N_\tau-\tau-1} \tilde{\tau} (2\kappa)^{2(N_\tau-\tilde{\tau})} + \sum_{\tau=1}^{N_\tau-2} \sum_{\tau'=1}^{N_\tau-\tau-1} (N_\tau - \tau - \tau') (2\kappa)^{2(N_\tau-\tau')} \\
 & \quad + \sum_{\tau=1}^{N_\tau-2} \sum_{\tau'=1}^{N_\tau-\tau-1} (N_\tau - \tau - \tau') (2\kappa)^{2(N_\tau-\tau)} \\
 &= \sum_{\tau=1}^{N_\tau-2} \sum_{\tau'=1}^{N_\tau-\tau-1} (N_\tau - \tau) (2\kappa)^{2(N_\tau-\tau')} + \sum_{\tau=1}^{N_\tau-2} \sum_{\tau'=1}^{N_\tau-\tau-1} (N_\tau - \tau - \tau') (2\kappa)^{2(N_\tau-\tau)} \\
 &= \sum_{\tau=1}^{N_\tau-2} \sum_{\tilde{\tau}=\tau+1}^{N_\tau-1} (N_\tau - \tau) (2\kappa)^{2\tilde{\tau}} + \sum_{\tilde{\tau}=2}^{N_\tau-1} \sum_{\tau'=1}^{\tilde{\tau}-1} (\tilde{\tau} - \tau') (2\kappa)^{2\tilde{\tau}} \\
 &= \sum_{\tilde{\tau}=2}^{N_\tau-1} \sum_{\tau=1}^{\tilde{\tau}-1} (N_\tau - \tau) (2\kappa)^{2\tilde{\tau}} + \sum_{\tilde{\tau}=2}^{N_\tau-1} \sum_{\tau'=1}^{\tilde{\tau}-1} (\tilde{\tau} - \tau') (2\kappa)^{2\tilde{\tau}} = N_\tau \sum_{\tau=2}^{N_\tau-1} (\tau - 1) (2\kappa)^{2\tau}. \quad (4.24)
 \end{aligned}$$

From the first to the second line, $\tilde{\tau} = N_\tau - \tau - \tau'$ has been substituted in the first summand. From the third to the fourth line, $\tilde{\tau} = N_\tau - \tau'$ has been substituted in the term at the front, and $\tilde{\tau} = N_\tau - \tau$ in the term at the back. A similar calculation can be performed for the prefactor of $W_{1021}(\mathbf{x})$ in eq. (4.22):

$$\begin{aligned}
 & \sum_{\tau=1}^{N_\tau-2} \sum_{\tau'=1}^{N_\tau-\tau-1} (N_\tau - \tau - \tau') \left((2\kappa)^{2(N_\tau-\tau-\tau')} + (2\kappa)^{2\tau} + (2\kappa)^{2\tau'} \right) \\
 &= \sum_{\tau=1}^{N_\tau-2} \sum_{\tilde{\tau}=1}^{N_\tau-\tau-1} \tilde{\tau} (2\kappa)^{2\tilde{\tau}} + \sum_{\tau=1}^{N_\tau-2} \sum_{\tau'=1}^{N_\tau-\tau-1} (N_\tau - \tau - \tau') (2\kappa)^{2\tau} \\
 & \quad + \sum_{\tau=1}^{N_\tau-2} \sum_{\tau'=1}^{N_\tau-\tau-1} (N_\tau - \tau - \tau') (2\kappa)^{2\tau'} \\
 &= \sum_{\tau=1}^{N_\tau-2} \sum_{\tau'=1}^{N_\tau-\tau-1} (N_\tau - \tau - \tau') (2\kappa)^{2\tau} + \sum_{\tau=1}^{N_\tau-2} \sum_{\tau'=1}^{N_\tau-\tau-1} (N_\tau - \tau) (2\kappa)^{2\tau'} \\
 &= \sum_{\tau=1}^{N_\tau-2} \sum_{\tau'=1}^{N_\tau-\tau-1} (N_\tau - \tau - \tau') (2\kappa)^{2\tau} + \sum_{\tau'=1}^{N_\tau-2} \sum_{\tau=1}^{N_\tau-\tau'-1} (N_\tau - \tau) (2\kappa)^{2\tau'} \\
 &= N_\tau \sum_{\tau=1}^{N_\tau-2} (N_\tau - \tau - 1) (2\kappa)^{2\tau}. \quad (4.25)
 \end{aligned}$$

Here, the same substitution as above has been employed from the first to the second line, namely $\tilde{\tau} = N_\tau - \tau - \tau'$ in the summand at the front. For the negative permutations of the temporal indices (cf. eq. (4.23)), identical prefactors emerge, if the temporal distances τ and τ' are aptly defined. The final result for $\text{tr}(B(\mathbf{x}, \tau_1, \tau_2)B(\mathbf{x}, \tau_2, \tau_3)B(\mathbf{x}, \tau_3, \tau_1))$ is thus, if it is only

4. Higher-order corrections to the nearest-neighbour fermion interaction

multiplied by time-independent traces,

$$\begin{aligned}
& \sum_{\tau_1 \neq \tau_2 \neq \tau_3} \text{tr}(B(\mathbf{x}, \tau_1, \tau_2)B(\mathbf{x}, \tau_2, \tau_3)B(\mathbf{x}, \tau_3, \tau_1)) \\
&= -\frac{N_\tau(N_\tau - 1)(N_\tau - 2)}{16} \left\{ W_{3131}^-(\mathbf{x}) - W_{3232}^-(\mathbf{x}) \right. \\
&\quad \left. + \frac{6}{(N_\tau - 1)(N_\tau - 2)} \left[\sum_{\tau=2}^{N_\tau-1} (\tau - 1)(2\kappa)^{2\tau} (W_{2010}(\mathbf{x}) - W_{1020}(\mathbf{x})) \right. \right. \\
&\quad \left. \left. + \sum_{\tau=1}^{N_\tau-2} (N_\tau - \tau - 1)(2\kappa)^{2\tau} (W_{1021}(\mathbf{x}) - W_{2110}(\mathbf{x})) \right] \right\} \quad (4.26)
\end{aligned}$$

The summation over three temporal coordinates can be incorporated in the `Mathematica` implementation in a similar way to the one over two indices. To that end, expressions of the form $\text{tr}(B(\mathbf{x}, \tau_1, \tau_2)B(\mathbf{x}, \tau_2, \tau_3)B(\mathbf{x}, \tau_3, \tau_1))$ are replaced by

$$\begin{aligned}
& -\frac{1}{8} \left[W_{3100}(\mathbf{x}) + W_{0032}(\mathbf{x}) \right. \\
&\quad \left. + \left((2\kappa)^{2(\tau_{\mathcal{P}(3)} - \tau_{\mathcal{P}(1)})} + (2\kappa)^{2(N_\tau - (\tau_{\mathcal{P}(3)} - \tau_{\mathcal{P}(2)}))} + (2\kappa)^{2(N_\tau - (\tau_{\mathcal{P}(2)} - \tau_{\mathcal{P}(1)}))} \right) W_{2010}(\mathbf{x}) \right. \\
&\quad \left. + \left((2\kappa)^{2(N_\tau - (\tau_{\mathcal{P}(3)} - \tau_{\mathcal{P}(1)}))} + (2\kappa)^{2(\tau_{\mathcal{P}(2)} - \tau_{\mathcal{P}(1)})} + (2\kappa)^{2(\tau_{\mathcal{P}(3)} - \tau_{\mathcal{P}(2)})} \right) W_{1021}(\mathbf{x}) \right], \quad (4.27)
\end{aligned}$$

if the permutation sign of $(\tau_{\mathcal{P}(1)}, \tau_{\mathcal{P}(2)}, \tau_{\mathcal{P}(3)})$ is positive, and by

$$\begin{aligned}
& \frac{1}{8} \left[W_{3200}(\mathbf{x}) + W_{0031}(\mathbf{x}) \right. \\
&\quad \left. + \left((2\kappa)^{2(N_\tau - (\tau_{\mathcal{P}(2)} - \tau_{\mathcal{P}(1)}))} + (2\kappa)^{2(\tau_{\mathcal{P}(3)} - \tau_{\mathcal{P}(1)})} + (2\kappa)^{2(N_\tau - (\tau_{\mathcal{P}(3)} - \tau_{\mathcal{P}(2)}))} \right) W_{1020}(\mathbf{x}) \right. \\
&\quad \left. + \left((2\kappa)^{2(\tau_{\mathcal{P}(2)} - \tau_{\mathcal{P}(1)})} + (2\kappa)^{2(\tau_{\mathcal{P}(3)} - \tau_{\mathcal{P}(2)})} + (2\kappa)^{2(N_\tau - (\tau_{\mathcal{P}(3)} - \tau_{\mathcal{P}(1)}))} \right) W_{2110}(\mathbf{x}) \right], \quad (4.28)
\end{aligned}$$

if the permutation sign of $(\tau_{\mathcal{P}(1)}, \tau_{\mathcal{P}(2)}, \tau_{\mathcal{P}(3)})$ is negative. Note that in the latter case, $\tau_{\mathcal{P}(3)}$ plays the role of τ_2 and $\tau_{\mathcal{P}(2)}$ the role of τ_3 in comparison with eq. (4.23). This is due to the fact that the order of τ_2 and τ_3 has already been interchanged there, which is achieved by the permutation \mathcal{P} in the automated version. After the multiplication of all trace factors, the temporal summation has to be carried out. For terms including three distinct temporal indices, the distances are replaced according to $\tau_{\mathcal{P}(2)} - \tau_{\mathcal{P}(1)} \rightarrow \tau$ and $\tau_{\mathcal{P}(3)} - \tau_{\mathcal{P}(2)} \rightarrow \tau'$, and then summed over by $\sum_{\tau=1}^{N_\tau-2} \sum_{\tau'=1}^{N_\tau-\tau-1} (N_\tau - \tau - \tau')$. This contains the prefactor which accounts for the transformation of the temporal sums to the differences τ and τ' .

With this automation at our disposal, we can hence evaluate the temporal sums over all terms comprising exclusively traces which are relevant up to $\mathcal{O}(\kappa^6)$. It suffices to derive the elementary traces by hand, as attained with eqs. (4.12) to (4.14), (4.18), (4.20), (4.27) and (4.28). The multiplication of these factors and the final temporal summation are dealt with by the computer.

4.3.2. Determinants

The last topic that needs to be discussed are terms involving determinants of B . Because of the multiplicativity of the determinant, it is sufficient to distinguish two cases here: one for the

part of B which is diagonal in temporal space, and one for the off-diagonal part. Determinants of more intricate products of these can always be written as products of determinants of one single B -matrix.

Diagonal part of B

The determinant of the diagonal part of B can be formulated in terms of traces over Wilson lines W by adopting the relation (A.31) for the determinant of a 3×3 -matrix. Prior to that, one has to factor out the first summand, which stems from B^+ :

$$\begin{aligned} \det(B(\mathbf{x}, \tau, \tau)) &= \det \left(-\frac{1}{2} \frac{h_1 W_{\mathbf{x}}}{\mathbb{1} + h_1 W_{\mathbf{x}}} + \frac{1}{2} \frac{\bar{h}_1 W_{\mathbf{x}}^\dagger}{\mathbb{1} + \bar{h}_1 W_{\mathbf{x}}^\dagger} \right) \\ &= \det \left(-\frac{1}{2} \frac{h_1 W_{\mathbf{x}}}{\mathbb{1} + h_1 W_{\mathbf{x}}} \right) \det \left(\mathbb{1} - \frac{\bar{h}_1 W_{\mathbf{x}}^\dagger \mathbb{1} + h_1 W_{\mathbf{x}}}{h_1 W_{\mathbf{x}} \mathbb{1} + \bar{h}_1 W_{\mathbf{x}}^\dagger} \right) \\ &= -\frac{1}{8} \frac{h_1^3}{1 + h_1 L_{\mathbf{x}} + h_1^2 L_{\mathbf{x}}^\dagger + h_1^3} \det \left(\mathbb{1} - e^{-2N_\tau a\mu} (W_{\mathbf{x}}^\dagger)^2 \frac{\mathbb{1} + h_1 W_{\mathbf{x}}}{\mathbb{1} + \bar{h}_1 W_{\mathbf{x}}^\dagger} \right). \end{aligned} \quad (4.29)$$

Here, eq. (A.32) has been employed to express the determinant of $\mathbb{1} + h_1 W_{\mathbf{x}}$ in terms of Polyakov loops. Moreover, it has been exploited that $W_{\mathbf{x}} \in \text{SU}(3)$ and therefore possesses determinant 1 and inverse $W_{\mathbf{x}}^\dagger$. Applying now eq. (A.31) to the determinant in the last line of eq. (4.29) and using that the adjugate of an invertible square matrix A is given by $\text{adj}(A) = A^{-1} \det(A)$ (cf. eq. (2.66)) leads to

$$\begin{aligned} &\det \left(\mathbb{1} - e^{-2N_\tau a\mu} (W_{\mathbf{x}}^\dagger)^2 \frac{\mathbb{1} + h_1 W_{\mathbf{x}}}{\mathbb{1} + \bar{h}_1 W_{\mathbf{x}}^\dagger} \right) \\ &= 1 - e^{-2N_\tau a\mu} \text{tr} \left((W_{\mathbf{x}}^\dagger)^2 \frac{\mathbb{1} + h_1 W_{\mathbf{x}}}{\mathbb{1} + \bar{h}_1 W_{\mathbf{x}}^\dagger} \right) \\ &\quad + e^{-4N_\tau a\mu} \text{tr} \left(\frac{\mathbb{1} + \bar{h}_1 W_{\mathbf{x}}^\dagger}{\mathbb{1} + h_1 W_{\mathbf{x}}} (W_{\mathbf{x}}) \right)^2 \det \left((W_{\mathbf{x}}^\dagger)^2 \frac{\mathbb{1} + h_1 W_{\mathbf{x}}}{\mathbb{1} + \bar{h}_1 W_{\mathbf{x}}^\dagger} \right) \\ &\quad - e^{-6N_\tau a\mu} \det \left((W_{\mathbf{x}}^\dagger)^2 \frac{\mathbb{1} + h_1 W_{\mathbf{x}}}{\mathbb{1} + \bar{h}_1 W_{\mathbf{x}}^\dagger} \right) \\ &= 1 - (2\kappa)^{-2N_\tau} (W_{0012}(\mathbf{x}) + W_{0112}(\mathbf{x})) \\ &\quad + e^{-6N_\tau a\mu} \left[(2\kappa)^{-2N_\tau} (W_{1200}(\mathbf{x}) + W_{1201}(\mathbf{x})) - 1 \right] \frac{1 + h_1 L_{\mathbf{x}} + h_1^2 L_{\mathbf{x}}^\dagger + h_1^3}{1 + \bar{h}_1 L_{\mathbf{x}}^\dagger + \bar{h}_1^2 L_{\mathbf{x}} + \bar{h}_1^3} \end{aligned} \quad (4.30)$$

Accordingly, the final result for the determinant of the part of B which is diagonal in temporal space is

$$\begin{aligned} \det(B(\mathbf{x}, \tau, \tau)) &= -\frac{h_1^3}{8} \left[\frac{1 - (2\kappa)^{-2N_\tau} (W_{0012}(\mathbf{x}) + W_{0112}(\mathbf{x}))}{1 + h_1 L_{\mathbf{x}} + h_1^2 L_{\mathbf{x}}^\dagger + h_1^3} \right. \\ &\quad \left. + e^{-6N_\tau a\mu} \frac{(2\kappa)^{-2N_\tau} (W_{1200}(\mathbf{x}) + W_{1201}(\mathbf{x})) - 1}{1 + \bar{h}_1 L_{\mathbf{x}}^\dagger + \bar{h}_1^2 L_{\mathbf{x}} + \bar{h}_1^3} \right]. \end{aligned} \quad (4.31)$$

This is independent of the temporal coordinate, rendering the summation over it trivial.

Off-diagonal part of B

For the off-diagonal part of B , one needs to further discriminate between the two possible arrangements of its temporal indices. In order to facilitate the evaluation of the temporal sums, the determinant is converted to traces in a similar fashion to above:

$$\begin{aligned}
 \det(B(\mathbf{x}, \tau_1, \tau_2))|_{\tau_1 < \tau_2} &= \det \left(\frac{1}{2} h_1^{\frac{\tau_2 - \tau_1}{N_\tau}} \frac{W_{\mathbf{x}}(\tau_1, \tau_2)}{\mathbb{1} + h_1 W_{\mathbf{x}}} + \frac{1}{2} h_1^{1 + \frac{\tau_1 - \tau_2}{N_\tau}} \frac{W_{\mathbf{x}}^\dagger(\tau_1, \tau_2)}{\mathbb{1} + \bar{h}_1 W_{\mathbf{x}}^\dagger} \right) \\
 &= \frac{1}{8} \frac{h_1^{\frac{3(\tau_2 - \tau_1)}{N_\tau}}}{1 + h_1 L_{\mathbf{x}} + h_1^2 L_{\mathbf{x}}^\dagger + h_1^3} \det \left(\mathbb{1} + (2\kappa)^{2(\tau_1 - \tau_2)} (\mathbb{1} + h_1 W_{\mathbf{x}}) \frac{\bar{h}_1 W_{\mathbf{x}}^\dagger}{\mathbb{1} + \bar{h}_1 W_{\mathbf{x}}^\dagger} \right) \\
 &= \frac{h_1^{\frac{3(\tau_2 - \tau_1)}{N_\tau}}}{8} \left[\frac{1 + (2\kappa)^{2(\tau_1 - \tau_2)} (W_{0011}(\mathbf{x}) + W_{0111}(\mathbf{x}))}{1 + h_1 L_{\mathbf{x}} + h_1^2 L_{\mathbf{x}}^\dagger + h_1^3} \right. \\
 &\quad \left. + \bar{h}_1^3 (2\kappa)^{4(\tau_1 - \tau_2)} \frac{(2\kappa)^{-2N_\tau} (W_{1100}(\mathbf{x}) + W_{1101}(\mathbf{x})) + (2\kappa)^{2(\tau_1 - \tau_2)}}{1 + \bar{h}_1 L_{\mathbf{x}}^\dagger + \bar{h}_1^2 L_{\mathbf{x}} + \bar{h}_1^3} \right] \tag{4.32}
 \end{aligned}$$

and

$$\begin{aligned}
 \det(B(\mathbf{x}, \tau_1, \tau_2))|_{\tau_1 > \tau_2} &= \det \left(-\frac{1}{2} h_1^{1 + \frac{\tau_2 - \tau_1}{N_\tau}} \frac{W_{\mathbf{x}}(\tau_1, \tau_2)}{\mathbb{1} + h_1 W_{\mathbf{x}}} - \frac{1}{2} h_1^{\frac{\tau_1 - \tau_2}{N_\tau}} \frac{W_{\mathbf{x}}^\dagger(\tau_1, \tau_2)}{\mathbb{1} + \bar{h}_1 W_{\mathbf{x}}^\dagger} \right) \\
 &= -\frac{1}{8} \frac{h_1^{3(1 + \frac{\tau_2 - \tau_1}{N_\tau})}}{1 + h_1 L_{\mathbf{x}} + h_1^2 L_{\mathbf{x}}^\dagger + h_1^3} \\
 &\quad \det \left(\mathbb{1} + (2\kappa)^{2(\tau_1 - \tau_2 - N_\tau)} (\mathbb{1} + h_1 W_{\mathbf{x}}) \frac{\bar{h}_1 W_{\mathbf{x}}^\dagger}{\mathbb{1} + \bar{h}_1 W_{\mathbf{x}}^\dagger} \right) \\
 &= -\frac{h_1^{3(1 + \frac{\tau_2 - \tau_1}{N_\tau})}}{8} \left[\frac{1 + (2\kappa)^{2(\tau_1 - \tau_2 - N_\tau)} (W_{0011}(\mathbf{x}) + W_{0111}(\mathbf{x}))}{1 + h_1 L_{\mathbf{x}} + h_1^2 L_{\mathbf{x}}^\dagger + h_1^3} \right. \\
 &\quad \left. + \bar{h}_1^3 (2\kappa)^{4(\tau_1 - \tau_2 - N_\tau)} \frac{(2\kappa)^{-2N_\tau} (W_{1100}(\mathbf{x}) + W_{1101}(\mathbf{x})) + (2\kappa)^{2(\tau_1 - \tau_2 - N_\tau)}}{1 + \bar{h}_1 L_{\mathbf{x}}^\dagger + \bar{h}_1^2 L_{\mathbf{x}} + \bar{h}_1^3} \right] \tag{4.33}
 \end{aligned}$$

This proves that also the determinants are gauge invariant under all circumstances: Owing to the fact that $\det W_{\mathbf{x}}(\tau_1, \tau_2) = 1$, only whole Wilson lines remain, which form closed loops in temporal direction.

These results can be integrated into the `Mathematica` implementation in the following way: Terms of the type $\det(B(\mathbf{x}, \tau_1, \tau_2))$ are replaced by eq. (4.32) if $\tau_{\mathcal{P}(1)} < \tau_{\mathcal{P}(2)}$, that is if the permutation sign of $(\tau_{\mathcal{P}(1)}, \tau_{\mathcal{P}(2)})$ is positive. If it is negative, which means $\tau_{\mathcal{P}(1)} > \tau_{\mathcal{P}(2)}$, such terms are replaced by eq. (4.33). It is worth emphasising that here, in contrast to the traces, one has to use τ_1 and τ_2 in the inserted expressions, not $\tau_{\mathcal{P}(1)}$ and $\tau_{\mathcal{P}(2)}$. The reason for this is that in the case of the traces, multiple arrangements of the temporal coordinates are treated at once by means of the permutation \mathcal{P} . This does not work out correctly for the determinants, which is why the two arrangements have to be handled individually. The permutation \mathcal{P} merely serves to differentiate between them.

The automation again spares us from calculating products of eqs. (4.32) and (4.33), as well as from carrying out the actual temporal sums by hand. These tasks are accomplished by

the computer. Since the final results become extremely lengthy and cumbersome, they are not displayed within this thesis. On the same grounds, and because only the contribution to the nearest-neighbour interaction has been obtained so far, the $\mathcal{O}(\kappa^6)$ -corrections were not implemented in the numerical simulation of chapter 3. On the other hand, the derivation scheme worked out in the present chapter smooths the path for the computation of even higher corrections ordered by the interaction range. In addition, it enables further analytical investigations of the effective theory.

4.4. Ladder resummation

As an example of the application of analytical techniques, a resummation scheme which is specific to the nearest-neighbour interaction shall be discussed. This so-called ladder resummation was introduced in [24]. The underlying idea is to study a particular subset of all terms in the nearest-neighbour interaction eq. (4.1), namely the single-trace terms $\text{tr}_{c,d,t}(\tilde{M}_{C_2}^k)$. These still contain a wide variety of graphs, which necessitate the calculation of more and more complicated gauge integrals. Thus, the subset of terms under consideration is further shrunk to those where always consecutive hops are paired with each other for the gauge integration. This is one possible permutation of the particle configuration where individual mesons are exchanged between the two spatial lattice sites (cf. fig. 4.1c). As a consequence, only the most simple gauge integral eq. (A.18) is required.

In order to simplify the analysis, we will restrict ourselves to the dense regime, where the thermodynamics is dominated by quarks, not antiquarks. We will hence neglect all terms involving antiquarks, which are mathematically encoded by \bar{h}_1 . In [24] it has been proved that the gauge integration for aforementioned terms leads in this case to

$$\mathcal{A}_k = \frac{1}{k} \left(\frac{2\kappa^2}{N_c} \right)^k \sum_{\tau_1 \neq \tau_2 \neq \dots \neq \tau_k} \text{tr}_c(B(\mathbf{x}, \tau_1, \tau_2)B(\mathbf{x}, \tau_2, \tau_3) \cdots B(\mathbf{x}, \tau_k, \tau_1)) \left(\frac{1}{2} W_{1100}(\mathbf{x} + \hat{i}) \right)^k \quad (4.34)$$

for the embedding of the ladder which describes the interaction between two adjacent spatial lattice sites. Here, the sum over the temporal indices has to be restricted to the subset where none of them are equal³. This guarantees that the meson hops all happen at distinct times, so that the gauge integrals factorise. For $k = 3$, for instance, the term which enters into the ladder resummation is given by eq. (4.9) (where the prefactor $(2\kappa^2)^3/3$ is omitted).

The remaining task is to evaluate the colour trace in eq. (4.34) for all possible arrangements of the temporal coordinates. From the structure of B in temporal space it is clear that the result can only depend on the ordering of τ_1, \dots, τ_k , not on their precise values. This becomes particularly conspicuous if one adopts the temporal gauge. On the lattice, this corresponds to setting all temporal gauge links to $\mathbb{1}$ [4]. Because our lattice does not have infinite temporal extent, the gauge fixing is only allowed for all temporal links but one. Here, the links $U_4(\mathbf{x}, N_\tau - 1)$, that is the ones which cross the temporal boundary of the lattice, are

³Many thanks to Jonas Scheunert for pointing this out.

4. Higher-order corrections to the nearest-neighbour fermion interaction

kept at a non-trivial value $W_{\mathbf{x}}$. The temporal structure of B then looks like

$$B_{\mathbf{x}} = \frac{1}{2} \begin{pmatrix} -h_1 W_{\mathbf{x}} & h_1^{\frac{1}{N_\tau}} \mathbb{1} & h_1^{\frac{2}{N_\tau}} \mathbb{1} & h_1^{\frac{3}{N_\tau}} \mathbb{1} & \dots \\ -h_1^{\frac{N_\tau-1}{N_\tau}} W_{\mathbf{x}} & -h_1 W_{\mathbf{x}} & h_1^{\frac{1}{N_\tau}} \mathbb{1} & h_1^{\frac{2}{N_\tau}} \mathbb{1} & \\ -h_1^{\frac{N_\tau-2}{N_\tau}} W_{\mathbf{x}} & -h_1^{\frac{N_\tau-1}{N_\tau}} W_{\mathbf{x}} & -h_1 W_{\mathbf{x}} & h_1^{\frac{1}{N_\tau}} \mathbb{1} & \\ -h_1^{\frac{N_\tau-3}{N_\tau}} W_{\mathbf{x}} & -h_1^{\frac{N_\tau-2}{N_\tau}} W_{\mathbf{x}} & -h_1^{\frac{N_\tau-1}{N_\tau}} W_{\mathbf{x}} & -h_1 W_{\mathbf{x}} & \\ \vdots & & & & \ddots \end{pmatrix} (\mathbb{1} + h_1 W_{\mathbf{x}})^{-1}. \quad (4.35)$$

For each crossing of the antiperiodic boundary one obtains a factor of $-W_{\mathbf{x}}$. Note that consequently $W_{\mathbf{x}}$ is the value of the Wilson line in temporal gauge, which can be used to generalise the outcomes of the computation to an arbitrary gauge.

In the colour trace from eq. (4.34), such a crossing of the temporal boundary occurs once for each descent in the permutation $(\tau_1, \tau_2, \dots, \tau_k, \tau_1)$. At least one descent arises from returning to the starting point; the maximal number of descents is $k - 1$. Owing to the cyclic property of the construction, each cyclic permutation of $\{\tau_1, \dots, \tau_k\}$ yields the same number of descents in $(\tau_1, \dots, \tau_k, \tau_1)$. This introduces an overall prefactor of k . Apart from that, it implies that it is sufficient to consider such permutations of $\{\tau_1, \dots, \tau_k\}$ where $\tau_k \rightarrow \tau_1$ is a descent: It is always possible to rotate (τ_1, \dots, τ_k) in such a way that this is the case. Accordingly, the number of permutations of $\{\tau_1, \dots, \tau_k\}$ with l descents in $(\tau_1, \dots, \tau_k, \tau_1)$ is k multiplied by the number of not cyclically identical permutations of $\{\tau_1, \dots, \tau_k\}$ with $l - 1$ descents.

The not cyclically identical permutations of k indices are most easily determined by switching to the cycle notation. It describes the effect of repeatedly applying a permutation on the elements of the set. The permutations sought-after are then those where a specified element is kept fixed. Without loss of generality, this can be selected to be the first one. Besides, this choice ensures that $\tau_k \rightarrow \tau_1$ is a descent, as required. The descents inside $(\tau_1, \tau_2, \dots, \tau_k)$ all take place in (τ_2, \dots, τ_k) , since the first – and thus smallest – element has been kept fixed. The not cyclically identical permutations of k indices can hence be mapped onto all permutations of $k - 1$ indices by removing the cycle (1) and reducing each number which appears in the other cycles by 1. Following the above argumentation, this leaves the number of descents in the corresponding list notations unchanged. For example, the not cyclically identical permutations of three indices are (1, 2, 3) and (1, 3, 2), having zero and one descents and cycle notations (1)(2)(3) and (1)(23), respectively. Implementing aforementioned procedure leads to (1)(2) and (12), which represent all possible permutations of two indices and also have zero and one descents, respectively.

Therefore, the number of not cyclically identical permutations of k indices with $l - 1$ descents is the same as the number of all permutations of $k - 1$ indices with $l - 1$ descents. This is known as Eulerian number $\left\langle \begin{smallmatrix} k-1 \\ l-1 \end{smallmatrix} \right\rangle$ [25]⁴.

Putting it all together, the colour trace from eq. (4.34) consists of expressions of the type $(-h_1 W_{\mathbf{x}})^l$, where l runs from 1 to $k - 1$. Due to the trace, the prefactors of h_1 from eq. (4.35) combine in such a way that the final power of h_1 matches the one of $W_{\mathbf{x}}$. In addition to that, the trace renders the result gauge invariant, so that $W_{\mathbf{x}}$ can be identified with the temporal Wilson line. The degeneracy factor for each l is $k \left\langle \begin{smallmatrix} k-1 \\ l-1 \end{smallmatrix} \right\rangle$, as derived above. Performing the temporal summation gives a factor of $1/k! \cdot (N_\tau)_k$ for each permutation of the temporal coordinates,

⁴To identify this with the notation in [25], one has to set $A_{n,s} = \left\langle \begin{smallmatrix} n \\ s-1 \end{smallmatrix} \right\rangle$.

because the rest of the term is time-independent. Here, $(N_\tau)_k = N_\tau(N_\tau - 1) \cdots (N_\tau - (k - 1))$ is the falling factorial of N_τ . In total, one arrives at

$$\begin{aligned}
 & \sum_{\tau_1 \neq \tau_2 \neq \dots \neq \tau_k} \text{tr}_c(B(\mathbf{x}, \tau_1, \tau_2)B(\mathbf{x}, \tau_2, \tau_3) \cdots B(\mathbf{x}, \tau_k, \tau_1)) \\
 &= \frac{1}{2^k} \frac{(N_\tau)_k}{(k-1)!} \sum_{l=1}^{k-1} \left\langle \begin{matrix} k-1 \\ l-1 \end{matrix} \right\rangle \text{tr}_c \left((-h_1 W_{\mathbf{x}})^l (\mathbb{1} + h_1 W_{\mathbf{x}})^{-k} \right) \\
 &= \frac{1}{2^k} \frac{(N_\tau)_k}{(k-1)!} \sum_{l=1}^{k-1} (-1)^l \left\langle \begin{matrix} k-1 \\ l-1 \end{matrix} \right\rangle W_{kl00}(\mathbf{x}) \\
 &= \frac{1}{2^k} \frac{(N_\tau)_k}{(k-1)!} \text{tr}_c \left(\sum_{l=1}^{k-1} \left\langle \begin{matrix} k-1 \\ l-1 \end{matrix} \right\rangle (-h_1 W_{\mathbf{x}})^l (\mathbb{1} + h_1 W_{\mathbf{x}})^{-k} \right) \\
 &= \frac{1}{2^k} \frac{(N_\tau)_k}{(k-1)!} \text{tr}_c(\text{Li}_{1-k}(-h_1 W_{\mathbf{x}})), \tag{4.36}
 \end{aligned}$$

where in the last line the sum over l has been written in terms of a mathematically well-known function, the polylogarithm [26]. For the term in eq. (4.34) this means that

$$\begin{aligned}
 \mathcal{A}_k &= \frac{1}{2^k} \left(\frac{\kappa^2}{N_c} \right)^k \frac{(N_\tau)_k}{k!} \text{tr}_c(\text{Li}_{1-k}(-h_1 W_{\mathbf{x}}))(W_{1100}(\mathbf{x} + \hat{i}))^k \\
 &= \frac{1}{2^k} \left(\frac{\kappa^2}{N_c} \right)^k \binom{N_\tau}{k} \text{tr}_c(\text{Li}_{1-k}(-h_1 W_{\mathbf{x}}))(W_{1100}(\mathbf{x} + \hat{i}))^k. \tag{4.37}
 \end{aligned}$$

The conjecture made in [24] that the prefactor of $W_{kl00}(\mathbf{x})$ in \mathcal{A}_k might be independent of k or inversely proportional to k has hence been disproved. The more involved k -dependence, however, comes at the price that no closed expression for $\sum_k \mathcal{A}_k$ could be found.

To give some examples, the colour trace for $k = 3$ yields

$$\sum_{\tau_1 \neq \tau_2 \neq \tau_3} \text{tr}_c(B(\mathbf{x}, \tau_1, \tau_2)B(\mathbf{x}, \tau_2, \tau_3)B(\mathbf{x}, \tau_3, \tau_1)) = -\frac{(N_\tau)_3}{16} (W_{3100}(\mathbf{x}) - W_{3200}(\mathbf{x})), \tag{4.38}$$

which agrees with the full expression from eq. (4.26) if one sets $\bar{h}_1 = 0$ there. The complete contribution of $k = 3$ to the ladder is thus

$$\mathcal{A}_3 = -\frac{1}{48} \left(\frac{\kappa^2}{N_c} \right)^3 (N_\tau)_3 (W_{3100}(\mathbf{x}) - W_{3200}(\mathbf{x}))(W_{1100}(\mathbf{x} + \hat{i}))^3, \tag{4.39}$$

and $k = 4$ results in

$$\mathcal{A}_4 = -\frac{1}{384} \left(\frac{\kappa^2}{N_c} \right)^4 (N_\tau)_4 (W_{4100}(\mathbf{x}) - 4W_{4200}(\mathbf{x}) + W_{4300}(\mathbf{x}))(W_{1100}(\mathbf{x} + \hat{i}))^4. \tag{4.40}$$

This demonstrates how certain kinds of terms can be evaluated relatively easily and for a general order in κ if some further approximations are applied.

5. Conclusions and outlook

In this thesis, the effective theory for Lattice QCD in the strong coupling and heavy quark regime was studied with a numerical Monte Carlo simulation. Accordingly, we developed a Metropolis algorithm with adaptive stepsize in C++. The effective action was implemented up to $\mathcal{O}(\kappa^4)$, where all terms which contribute to the change of the action induced by a local update were taken into account. In addition, a parallel version of the simulation code was designed with MPI. This computer program was then used to measure the phase diagram of the effective theory at zero chemical potential. In particular, we determined the phase boundary of the deconfinement transition from the expectation value of the Polyakov loop. Likewise, we located the critical end point, where the type of the transition changes from first order to crossover. To that end, a finite size scaling analysis of the kurtosis was employed. The results for static quarks could be checked successfully against the ones from the literature, thus verifying our implementation of this part of the action, as well as the algorithm and the data analysis procedure.

The investigation of the ‘full’ $\mathcal{O}(\kappa^4)$ -action with one flavour revealed that the $\mathcal{O}(\kappa^4)$ -corrections weaken the influence of fermions, as $\lambda_{1,\text{pc}}$ and $h_{1,c}$ increased compared to the static case. Nevertheless, the shift was small enough to justify the approximations made in the derivation of the effective theory. The temperature at the critical end point turned out to be in the same range as the deconfinement temperature of pure gauge theory at the respective values of N_τ . This corroborates above statement that the physics is not strongly dependent on the inclusion of fermionic terms or higher corrections to them. The underlying reason is that the effective theory expands around heavy quarks. The comparison of the results for $N_\tau = 4$ and $N_\tau = 6$ showed that $\lambda_{1,\text{pc}}$ is larger in the latter case, leading to a smaller lattice spacing. This allows the physical temperature to be (roughly) the same for both values of N_τ , which is consistent with the literature. Similarly, we found that $\kappa_c(N_\tau=6)/\kappa_c(N_\tau=4) \approx 1.43$, which indicates as well that the temperature at the critical end point is approximately constant.

In the physically more interesting case of two degenerate quark flavours, the fermionic couplings at the critical end point ($h_{1,c}$ and κ_c) were lower than for one flavour. This could be explained by the existence of an additional symmetry breaking field. The critical gauge couplings ($\lambda_{1,c}$ and β_c) and the critical temperature T_c , on the other hand, were very close to their one-flavour values. Moreover, the analysis of two degenerate quark flavours permitted us to compare our results to the ones obtained from a similar effective theory in [22]. The arising disagreement could be accounted for by the effect of the $\mathcal{O}(\kappa^4)$ -corrections, which are not included in the expansion in [22]. A comparison with the critical point of full Lattice QCD, however, disclosed that κ_c should actually decrease with growing order in the hopping expansion. Consequently, the effective theory truncated at $\mathcal{O}(\kappa^4)$ does not seem to be sufficient to establish the critical point of QCD with two degenerate quark flavours. As for the one-flavour theory, the ratio of the critical hopping parameters at the two different choices of N_τ was compatible with $3/2$. This suggests that also for the effective theory with two degenerate quark flavours the temperature at the critical end point is almost unchanged between $N_\tau = 4$ and $N_\tau = 6$.

Besides, the range of validity of the large- N_τ approximation at constant temperature, baryon mass and baryon chemical potential was assessed. For this purpose, the maximal contributions of the various parts of the $\mathcal{O}(\kappa^4)$ -terms in the effective action were weighed against each other. The corresponding expressions were evaluated for 1000 randomly selected SU(3)-matrices W . It turned out that not all terms which are of parametrically subleading order in N_τ become irrelevant in the continuum limit. The reason for this is that h_1 and \bar{h}_1 tend to zero exponentially as $N_\tau \rightarrow \infty$ if the temperature and the baryon mass are kept fixed. Only the two-point interactions behave in the naively expected way, because the Dirac trace only leaves B s there. The problematic terms of subleading order in N_τ , by contrast, were demonstrated to stem from A s. Nevertheless, the negligence of such contributions was shown to be justified only for $N_\tau \gtrsim 30$ to 50, so certainly not for the N_τ -values used for the simulations in this thesis. We identified two main limitations to these statements: First of all, the impact of additional gauge corrections to the formula for h_1 remains unclear, but they are supposed to further soften the exponential decay with N_τ . A second point is that the function employed to compute β from the lattice spacing is not valid for $N_\tau \geq 14$ at the chosen temperature, and substitutes are difficult to obtain.

After completing the numerical studies, we turned to the derivation of the $\mathcal{O}(\kappa^6)$ -corrections to the nearest-neighbour fermion interaction. The Dirac trace could be evaluated in general for the nearest-neighbour interaction; the spatial link integration was automated with `Mathematica` for the contributions up to $\mathcal{O}(\kappa^6)$. No full automation could be attained so far for the temporal summation. Therefore, the splitting of the sums, the expansion of the powers and the combination of the products of the fractional Wilson lines were carried out by hand for all terms which are relevant up to $\mathcal{O}(\kappa^6)$. The multiplication of different traces or determinants and the final temporal summation were integrated into aforementioned `Mathematica` program. Additionally, we expressed the appearing determinants in terms of traces in order to prove their gauge invariance and to facilitate the temporal summation.

Furthermore, a resummation scheme which is specific to the nearest-neighbour interaction, the so-called ladder resummation, was investigated. Notably, we performed the temporal sums with the correct restriction, namely that the temporal indices are all distinct. In this way, we illustrated how one can calculate single-trace terms with paired consecutive hops in the dense limit to an arbitrary order in κ . This is a perfect example of the progress that can be achieved in the derivation by the application of analytical techniques like resummation and certain approximations.

In the future, it will be of great interest to extend the exploration of the phase diagram of the effective theory with the $\mathcal{O}(\kappa^4)$ -corrections to finite chemical potential. As the sign problem inhibits a direct access to the region with finite real μ , one will need to rely on methods such as sign reweighting to circumvent this complication in a Monte Carlo simulation. On the analytical side, possible research perspectives lie in the derivation of the full $\mathcal{O}(\kappa^6)$ -contribution to the effective action and its numerical implementation. To avoid the huge expressions originating from the temporal summation, one could include this step in the simulation code. However, one would then forfeit the dimensional reduction of the theory, making the runtime N_τ -dependent. In any case, a simulation with the $\mathcal{O}(\kappa^6)$ -corrections would allow a determination of the radius of convergence of the $\mathcal{O}(\kappa^4)$ -action and a clarification of the trend in κ_c . Due to that, it might be sensible to continue investigations in this direction.

Acknowledgements

Finally, I want to thank Prof. Dr. Owe Philipsen for giving me the chance to join his working group and the opportunity to write this Master's Thesis. I am also very grateful for numerous pieces of advice and assistance, as well as many inspirational discussions. Moreover, I am indebted to my colleagues in his working group, in particular to Jonas Scheunert, Dr. Jangho Kim, Anh Quang Pham, Alena Zmarsly, Christoph Konrad and Reinhold Kaiser. They always stood by me with help and guidance, and provided me with plenty of valuable tips and tools. Special thanks are equally due to my parents and my family, who accompanied me on my way through my studies and beyond, and supported me like no one else.

A. Appendix

A.1. Series expansions for the effective couplings

Here, we collect the series expansions for the effective couplings as they are used for the numerical implementation in chapter 3.

For SU(3), the expansion coefficient of the fundamental character in the character expansion eq. (2.29) cannot be expressed in a simple way in terms of special functions. There exists, however, the following series representation [3]:

$$u = a_f(\beta) = \frac{1}{3} \frac{c_3(\beta)}{c_1(\beta)}, \quad (\text{A.1})$$

$$\begin{aligned} c_3(\beta) = & \frac{1}{6}\beta + \frac{1}{72}\beta^2 + \frac{1}{216}\beta^3 + \frac{5}{10368}\beta^4 + \frac{13}{186624}\beta^5 + \frac{77}{11197440}\beta^6 + \frac{139}{201553920}\beta^7 \\ & + \frac{19}{322486272}\beta^8 + \frac{23}{4837294080}\beta^9 + \frac{319}{914248581120}\beta^{10} + \frac{2629}{109709829734400}\beta^{11} \\ & + \frac{16133}{10532143654502400}\beta^{12} + \frac{17449}{189578585781043200}\beta^{13} \\ & + \frac{35531}{6824829088117555200}\beta^{14} + \mathcal{O}(\beta^{15}), \end{aligned} \quad (\text{A.2})$$

$$\begin{aligned} c_1(\beta) = & 1 + \frac{1}{36}\beta^2 + \frac{1}{648}\beta^3 + \frac{1}{2592}\beta^4 + \frac{1}{31104}\beta^5 + \frac{13}{3359232}\beta^6 + \frac{11}{33592320}\beta^7 \\ & + \frac{139}{4837294080}\beta^8 + \frac{19}{8707129344}\beta^9 + \frac{23}{145118822400}\beta^{10} + \frac{29}{2742745743360}\beta^{11} \\ & + \frac{2629}{3949553870438400}\beta^{12} + \frac{1241}{31596430963507200}\beta^{13} \\ & + \frac{17449}{7962300602803814400}\beta^{14} + \mathcal{O}(\beta^{15}). \end{aligned} \quad (\text{A.3})$$

The effective couplings of the gauge interactions can be expanded in a strong coupling series in u . For the nearest-neighbour coupling in the fundamental representation, the result is [8]

$$\lambda_1(u) = u^{N_\tau} \cdot \begin{cases} \exp \left[2 \left(4u^4 + 12u^5 - 18u^6 - 36u^7 + \frac{219}{2}u^8 + \frac{1791}{10}u^9 + \frac{830517}{5120}u^{10} \right) \right], & N_\tau = 2 \\ \exp \left[4 \left(4u^4 + 12u^5 - 14u^6 - 36u^7 + \frac{295}{2}u^8 + \frac{1851}{10}u^9 + \frac{1035317}{5120}u^{10} \right) \right], & N_\tau = 4 \\ \exp \left[N_\tau \left(4u^4 + 12u^5 - 14u^6 - 36u^7 + \frac{295}{2}u^8 + \frac{1851}{10}u^9 + \frac{1055797}{5120}u^{10} \right) \right], & N_\tau \geq 6 \end{cases} \quad (\text{A.4})$$

and for the next-to-nearest neighbour coupling

$$\lambda_2(u) = u^{2N_\tau} \cdot \begin{cases} 2u^2 + 6u^4 + 31u^6, & N_\tau = 2 \\ 12u^2 + 26u^4 + 364u^6, & N_\tau = 4 \\ 30u^2 + 66u^4, & N_\tau = 6 \\ N_\tau(N_\tau - 1)u^2, & N_\tau \geq 8 \end{cases}. \quad (\text{A.5})$$

A. Appendix

The first terms of the strong coupling series for the nearest-neighbour coupling in the adjoint representation are (for $N_\tau \geq 2$)

$$\lambda_a(u) = v^{N_\tau-1} \left(v + N_\tau \frac{3}{2} u^6 + \dots \right), \quad v = \frac{9}{8} u^2 - \frac{9}{8} u^3 + \frac{81}{32} u^4 + \dots \quad (\text{A.6})$$

The effective couplings of the fermion interactions receive gauge corrections when moving away from the limit $\beta = 0$, as explained in section 2.6. These can also be expanded in series in u [7]. For the quark coupling h_1 from eq. (2.41), the first terms are (for $N_\tau \geq 3$)

$$h_1(\kappa, u) = \exp[N_\tau(a\mu + \ln(2\kappa))] \exp \left[6N_\tau \kappa^2 u \left(\frac{1 - u^{N_\tau-1}}{1 - u} + 4u^4 - 12\kappa^2 + 9\kappa^2 u + 4\kappa^2 u^2 - 4\kappa^4 \right) \right]. \quad (\text{A.7})$$

The antiquark coupling \bar{h}_1 from eq. (2.42) receives the same corrections. For the coupling of the $\mathcal{O}(\kappa^2)$ -action, the result is

$$h_2(\kappa, u) = \frac{\kappa^2 N_\tau}{N_c} \left(1 + 2 \frac{u - u^{N_\tau}}{1 - u} + 8u^5 + 16\kappa^3 u^4 \right). \quad (\text{A.8})$$

For the $\mathcal{O}(\kappa^4)$ -terms, one has to distinguish between four couplings with different gauge corrections:

$$h_{3_1}(\kappa, u) = \frac{N_\tau(N_\tau - 1)\kappa^4}{N_c^2} \cdot \begin{cases} 1, & N_\tau = 2 \\ 1 + \frac{8}{3}(u + u^2 + 4u^5 + 8\kappa^3 u^4), & N_\tau = 4 \\ 1 + \frac{2}{5}(8u + 12u^2 + 12u^3 + 8u^4 + 32u^5 + 64\kappa^3 u^4), & N_\tau = 6, \\ 1 + \frac{8}{7}(3u + 5u^2 + 6u^3 + 6u^4 + 17u^5 + 24\kappa^3 u^4), & N_\tau = 8 \\ 1 + \frac{4u(2 - N_\tau + N_\tau u)}{(N_\tau - 1)(u - 1)^3} + \frac{20(N_\tau - 6)}{N_\tau - 1} u^5 + \frac{40(N_\tau - 6)}{N_\tau - 1} \kappa^3 u^4, & N_\tau > 8 \end{cases} \quad (\text{A.9})$$

$$h_{3_2}(\kappa, u) = \frac{\kappa^4 N_\tau}{N_c^2} \left(1 + 4 \frac{u - u^{N_\tau}}{1 - u} + 16u^5 + 32\kappa^3 u^4 \right), \quad (\text{A.10})$$

$$h_{3_3}(\kappa, u) = \frac{\kappa^4 N_\tau^2}{N_c^2} \left(1 + 4 \frac{(1 - u^{N_\tau})(u - u^{N_\tau})}{(1 - u)^2} + 16u^5 + 32\kappa^3 u^4 \right), \quad (\text{A.11})$$

$$h_{3_4}(\kappa, u) = \frac{1}{2} \frac{\kappa^4 u N_\tau}{N_c^3} \left(1 + 4u^4 + 16u^3 \kappa^3 \right), \quad (\text{A.12})$$

where the relations for $h_{3_{2,3,4}}$ are valid for $N_\tau \geq 2$.

A.2. Gauge integrals

For the integration over the spatial gauge links, integrals of the type (2.57) need to be solved. In the literature, various methods for doing so have been proposed and successfully applied [12, 27–30]. The one which probably yields the easiest results to interpret and employ in the context of the effective theory is based on a generating function. Here, one first solves group integrals of the form

$$Z_G(m, m^\dagger) = \int_G dg e^{\text{tr}(gm^\dagger + g^\dagger m)} \quad (\text{A.13})$$

over the group G . The integral of interest can then be obtained by deriving Z with respect to the sources m and m^\dagger :

$$\int_{\text{SU}(N_c)} dU \prod_{\alpha=1}^a U_{I_\alpha, J_\alpha} \prod_{\beta=1}^b U_{K_\beta, L_\beta}^\dagger = \prod_{\alpha=1}^a \frac{\partial}{\partial m_{J_\alpha, I_\alpha}^\dagger} \prod_{\beta=1}^b \frac{\partial}{\partial m_{L_\beta, K_\beta}} Z_{\text{SU}(N_c)}(m, m^\dagger) \Big|_{m=m^\dagger=0}. \quad (\text{A.14})$$

The generating function for the group $\text{SU}(3)$ has been calculated in [28]¹:

$$Z_{\text{SU}(3)}(m, m^\dagger) = 2 \sum_{j,k,l,n=0}^{\infty} \frac{1}{(j+2k+3l+n+2)!(k+2l+n+1)!} \frac{X^j Y^k Z^l \Delta^n}{j! k! l! n!}, \quad (\text{A.15})$$

where

$$\begin{aligned} X &= \text{tr}(mm^\dagger), \\ Y &= \frac{1}{2} \text{tr}^2(mm^\dagger) - \frac{1}{2} \text{tr}((mm^\dagger)^2), \\ Z &= \det(mm^\dagger), \\ \Delta &= \det(m) + \det(m^\dagger). \end{aligned} \quad (\text{A.16})$$

Here, the occurring determinants may be expressed as

$$\det(m) = \frac{1}{N_c!} \epsilon_{K_1, \dots, K_{N_c}} \epsilon_{L_1, \dots, L_{N_c}} \prod_{i=1}^{N_c} m_{K_i, L_i}. \quad (\text{A.17})$$

With these relations at hand, the calculation of the gauge integrals for arbitrary values of a and b can be automated². Besides, the constraint cited below eq. (2.57) now becomes evident: For eq. (A.14) not to vanish, all m s and m^\dagger s in eq. (A.15) must be matched by a derivative. The only term which can introduce an imbalance between m s and m^\dagger s is Δ . It consists of determinants, which bring, according to eq. (A.17), elements of the source matrix always in groups of $N_c = 3$. All other terms in eq. (A.15) come with equal numbers of m s and m^\dagger s. Accordingly, the integral in eq. (A.14) can only be non-zero if $a = b \pmod{N_c}$.

The results used in the present thesis are the ones with $a, b \leq 3$, which are listed subsequently.

$$\int_{\text{SU}(3)} dU U_{I,J} U_{K,L}^\dagger = \frac{1}{3} \delta_{I,L} \delta_{J,K} \quad (\text{A.18})$$

$$\begin{aligned} \int_{\text{SU}(3)} dU U_{I_1, J_1} U_{I_2, J_2} U_{K_1, L_1}^\dagger U_{K_2, L_2}^\dagger &= \frac{1}{8} (\delta_{I_1, L_1} \delta_{I_2, L_2} \delta_{J_1, K_1} \delta_{J_2, K_2} + \delta_{I_1, L_2} \delta_{I_2, L_1} \delta_{J_1, K_2} \delta_{J_2, K_1}) \\ &\quad - \frac{1}{24} (\delta_{I_1, L_2} \delta_{I_2, L_1} \delta_{J_1, K_1} \delta_{J_2, K_2} + \delta_{I_1, L_1} \delta_{I_2, L_2} \delta_{J_1, K_2} \delta_{J_2, K_1}) \end{aligned} \quad (\text{A.19})$$

$$\int_{\text{SU}(3)} dU U_{I_1, J_1} U_{I_2, J_2} U_{I_3, J_3} = \frac{1}{6} \epsilon_{I_1, I_2, I_3} \epsilon_{J_1, J_2, J_3} \quad (\text{A.20})$$

$$\int_{\text{SU}(3)} dU U_{K_1, L_1}^\dagger U_{K_2, L_2}^\dagger U_{K_3, L_3}^\dagger = \frac{1}{6} \epsilon_{K_1, K_2, K_3} \epsilon_{L_1, L_2, L_3} \quad (\text{A.21})$$

¹The missing factor of $1/2$ in front of the second trace in Y has been amended.

²Many thanks to Jonas Scheunert for providing his `Mathematica` worksheet on this.

A. Appendix

$$\begin{aligned}
& \int_{\text{SU}(3)} dU U_{I_1, J_1} U_{I_2, J_2} U_{I_3, J_3} U_{K_1, L_1}^\dagger U_{K_2, L_2}^\dagger U_{K_3, L_3}^\dagger \\
&= \frac{1}{24} (\delta_{I_1, L_1} \delta_{I_2, L_2} \delta_{I_3, L_3} \delta_{J_1, K_1} \delta_{J_2, K_2} \delta_{J_3, K_3} + \delta_{I_1, L_2} \delta_{I_2, L_1} \delta_{I_3, L_3} \delta_{J_1, K_2} \delta_{J_2, K_1} \delta_{J_3, K_3} \\
&\quad + \delta_{I_1, L_3} \delta_{I_2, L_2} \delta_{I_3, L_1} \delta_{J_1, K_3} \delta_{J_2, K_2} \delta_{J_3, K_1} + \delta_{I_1, L_1} \delta_{I_2, L_3} \delta_{I_3, L_2} \delta_{J_1, K_1} \delta_{J_2, K_3} \delta_{J_3, K_2} \\
&\quad + \delta_{I_1, L_2} \delta_{I_2, L_3} \delta_{I_3, L_1} \delta_{J_1, K_2} \delta_{J_2, K_3} \delta_{J_3, K_1} + \delta_{I_1, L_3} \delta_{I_2, L_1} \delta_{I_3, L_2} \delta_{J_1, K_3} \delta_{J_2, K_1} \delta_{J_3, K_2}) \\
&- \frac{1}{120} (\delta_{I_1, L_1} \delta_{I_2, L_2} \delta_{I_3, L_3} \delta_{J_1, K_2} \delta_{J_2, K_1} \delta_{J_3, K_3} + \delta_{I_1, L_3} \delta_{I_2, L_1} \delta_{I_3, L_2} \delta_{J_1, K_3} \delta_{J_2, K_2} \delta_{J_3, K_1} \\
&\quad + \delta_{I_1, L_2} \delta_{I_2, L_3} \delta_{I_3, L_1} \delta_{J_1, K_1} \delta_{J_2, K_3} \delta_{J_3, K_2} + \delta_{I_1, L_2} \delta_{I_2, L_1} \delta_{I_3, L_3} \delta_{J_1, K_1} \delta_{J_2, K_2} \delta_{J_3, K_3} \\
&\quad + \delta_{I_1, L_3} \delta_{I_2, L_2} \delta_{I_3, L_1} \delta_{J_1, K_3} \delta_{J_2, K_1} \delta_{J_3, K_2} + \delta_{I_1, L_1} \delta_{I_2, L_3} \delta_{I_3, L_2} \delta_{J_1, K_2} \delta_{J_2, K_3} \delta_{J_3, K_1} \\
&\quad + \delta_{I_1, L_1} \delta_{I_2, L_2} \delta_{I_3, L_3} \delta_{J_1, K_3} \delta_{J_2, K_2} \delta_{J_3, K_1} + \delta_{I_1, L_2} \delta_{I_2, L_3} \delta_{I_3, L_1} \delta_{J_1, K_2} \delta_{J_2, K_1} \delta_{J_3, K_3} \\
&\quad + \delta_{I_1, L_3} \delta_{I_2, L_1} \delta_{I_3, L_2} \delta_{J_1, K_1} \delta_{J_2, K_3} \delta_{J_3, K_2} + \delta_{I_1, L_1} \delta_{I_2, L_3} \delta_{I_3, L_2} \delta_{J_1, K_3} \delta_{J_2, K_1} \delta_{J_3, K_2} \\
&\quad + \delta_{I_1, L_3} \delta_{I_2, L_2} \delta_{I_3, L_1} \delta_{J_1, K_1} \delta_{J_2, K_2} \delta_{J_3, K_3} + \delta_{I_1, L_2} \delta_{I_2, L_1} \delta_{I_3, L_3} \delta_{J_1, K_2} \delta_{J_2, K_3} \delta_{J_3, K_1} \\
&\quad + \delta_{I_1, L_1} \delta_{I_2, L_2} \delta_{I_3, L_3} \delta_{J_1, K_1} \delta_{J_2, K_3} \delta_{J_3, K_2} + \delta_{I_1, L_2} \delta_{I_2, L_3} \delta_{I_3, L_1} \delta_{J_1, K_3} \delta_{J_2, K_2} \delta_{J_3, K_1} \\
&\quad + \delta_{I_1, L_3} \delta_{I_2, L_1} \delta_{I_3, L_2} \delta_{J_1, K_2} \delta_{J_2, K_1} \delta_{J_3, K_3} + \delta_{I_1, L_1} \delta_{I_2, L_3} \delta_{I_3, L_2} \delta_{J_1, K_1} \delta_{J_2, K_2} \delta_{J_3, K_3} \\
&\quad + \delta_{I_1, L_3} \delta_{I_2, L_2} \delta_{I_3, L_1} \delta_{J_1, K_2} \delta_{J_2, K_3} \delta_{J_3, K_1} + \delta_{I_1, L_2} \delta_{I_2, L_1} \delta_{I_3, L_3} \delta_{J_1, K_3} \delta_{J_2, K_1} \delta_{J_3, K_2}) \\
&+ \frac{1}{60} \epsilon_{I_1, I_2, I_3} \epsilon_{J_1, J_2, J_3} \epsilon_{K_1, K_2, K_3} \epsilon_{L_1, L_2, L_3} \tag{A.22}
\end{aligned}$$

All other combinations vanish due to the constraint explained above.

A.3. Additional analytical calculations for SU(3)-matrices

In this appendix, some analytical results for SU(3)-matrices which were used in the main part of the thesis are derived.

A.3.1. Application of the Cayley-Hamilton theorem for SU(3)-matrices

The Cayley-Hamilton theorem eq. (2.64) reads for the special case of a matrix $W \in \text{SU}(3)$:

$$-\mathbb{1} + c_1(W)W + c_2(W)W^2 + W^3 = 0. \tag{A.23}$$

Multiplying this by the inverse $W^{-1} = W^\dagger$, one can relate W^2 to the coefficients $c_{1,2}(W)$, the matrix W and its inverse:

$$-W^\dagger + c_1(W)\mathbb{1} + c_2(W)W + W^2 = 0 \Rightarrow W^2 = -c_1(W)\mathbb{1} - c_2(W)W + W^\dagger. \tag{A.24}$$

The coefficients of the characteristic polynomial can be obtained from the LeVerrier-Fadeev algorithm eq. (2.55):

$$c_2(W) = -\text{tr}(W), \quad c_1(W) = \frac{1}{2} \left(\text{tr}^2(W) - \text{tr}(W^2) \right). \tag{A.25}$$

Plugging this into the relation for W^2 from eq. (A.24) and taking the trace yields

$$\text{tr}(W^2) = -\frac{3}{2} \left(\text{tr}^2(W) - \text{tr}(W^2) \right) + \text{tr}^2(W) + \text{tr}(W^\dagger) \tag{A.26}$$

and hence

$$\mathrm{tr}(W^2) = \mathrm{tr}^2(W) - 2 \mathrm{tr}(W^\dagger) \Rightarrow c_1(W) = \mathrm{tr}(W^\dagger). \quad (\text{A.27})$$

With eq. (A.24), one can then reduce W^2 to W and W^\dagger :

$$W^2 = -\mathrm{tr}(W^\dagger)\mathbb{1} + \mathrm{tr}(W)W + W^\dagger. \quad (\text{A.28})$$

By multiplying eq. (A.24) once again with W^\dagger , one arrives at a similar reduction formula for the square of the inverse:

$$(W^\dagger)^2 = c_2(W)\mathbb{1} + W + c_1(W)W^\dagger = -\mathrm{tr}(W)\mathbb{1} + W + \mathrm{tr}(W^\dagger)W^\dagger. \quad (\text{A.29})$$

This is the same as eq. (A.28) with W and W^\dagger interchanged, as required by self-consistency.

A.3.2. Determinants of 3×3 -matrices

For a general three-dimensional square matrix $A \in \mathbb{C}^{3 \times 3}$ and $\alpha \in \mathbb{C}$, the following determinant can be expressed in terms of the characteristic polynomial of A :

$$\begin{aligned} \det(\mathbb{1} + \alpha A) &= -\alpha^3 \det(-\alpha^{-1}\mathbb{1} - A) = -\alpha^3 \chi_A(-\alpha^{-1}) \\ &= -\alpha^3(c_0(A) - \alpha^{-1}c_1(A) + \alpha^{-2}c_2(A) - \alpha^{-3}). \end{aligned} \quad (\text{A.30})$$

Here, $c_0(A) = -\det(A)$ (cf. eq. (2.65)) and the other two coefficients $c_{1,2}(A)$ are given by eq. (A.25). With eq. (2.67), the first coefficient may also be written in terms of the adjugate of A , $c_1(A) = \mathrm{tr}(B_3(A)) = \mathrm{tr}(\mathrm{adj}(A))$. The determinant from eq. (A.30) thus reads:

$$\det(\mathbb{1} + \alpha A) = 1 + \alpha \mathrm{tr}(A) + \alpha^2 \mathrm{tr}(\mathrm{adj}(A)) + \alpha^3 \det(A). \quad (\text{A.31})$$

In the special case that $A \in \mathrm{SU}(3)$, $\det(A) = 1$ and the adjugate is identical to the inverse (or, equivalently, adjoint) matrix (cf. eq. (2.66)). As a consequence, the identity (A.31) simplifies to

$$\det(\mathbb{1} + \alpha A) = 1 + \alpha \mathrm{tr}(A) + \alpha^2 \mathrm{tr}(A^\dagger) + \alpha^3 \quad (A \in \mathrm{SU}(3)). \quad (\text{A.32})$$

A.4. Results for the kinetic quark determinant up to $\mathcal{O}(\kappa^4)$

This appendix lists the results for the kinetic quark determinant in the effective theory up to $\mathcal{O}(\kappa^4)$ as they have been obtained in [7, 10]³. They are ordered by their interaction range.

A.4.1. Two-point interaction

The leading-order contribution to the two-point interaction is of $\mathcal{O}(\kappa^2)$:

$$\begin{aligned} & -N_f \kappa^2 \sum_{\{C_2\}} \int [dU_i] \mathrm{tr}_{c,d,t} (\tilde{M}_{C_2}) \\ &= -N_f \kappa^2 \sum_{\mathbf{x}, \hat{i}} \int [dU_i] \mathrm{tr}_{c,d,t} \left[S_{\mathbf{x}, \mathbf{x} + \hat{i}}^+ (\mathbb{1} - \kappa T)_{\mathbf{x} + \hat{i}}^{-1} S_{\mathbf{x} + \hat{i}, \mathbf{x}}^- (\mathbb{1} - \kappa T)_{\mathbf{x}}^{-1} \right] \\ &= -2N_f h_2 \sum_{\mathbf{x}, \hat{i}} W_{1111}^-(\mathbf{x}) W_{1111}^-(\mathbf{x} + \hat{i}). \end{aligned} \quad (\text{A.33})$$

³Some typos in the final results have been corrected.

A. Appendix

For the $\mathcal{O}(\kappa^4)$ -correction, there are two distinct contributions. The first one has a square inside the trace over the loop matrix:

$$\begin{aligned}
& -\frac{N_f}{2}\kappa^4 \sum_{\{C_2\}} \int [dU_i] \text{tr}_{c,d,t} \left(\tilde{M}_{C_2}^2 \right) \\
& = -\frac{N_f}{2}\kappa^4 \sum_{\mathbf{x},i} \int [dU_i] \text{tr}_{c,d,t} \left[S_{\mathbf{x},\mathbf{x}+\hat{i}}^+ (\mathbb{1} - \kappa T)_{\mathbf{x}+\hat{i}}^{-1} S_{\mathbf{x}+\hat{i},\mathbf{x}}^- (\mathbb{1} - \kappa T)_{\mathbf{x}}^{-1} S_{\mathbf{x},\mathbf{x}+\hat{i}}^+ (\mathbb{1} - \kappa T)_{\mathbf{x}+\hat{i}}^{-1} \right. \\
& \quad \left. S_{\mathbf{x}+\hat{i},\mathbf{x}}^- (\mathbb{1} - \kappa T)_{\mathbf{x}}^{-1} \right] \\
& = N_f h_{31} \sum_{\mathbf{x},i} \left[\left(W_{2121}^+(\mathbf{x}) + 2 \frac{1}{N_\tau - 1} \sum_{\tau=1}^{N_\tau-1} (2\kappa)^{2\tau} W_{1010}(\mathbf{x}) \right) \left(W_{1111}^-(\mathbf{x} + \hat{i}) \right)^2 \right. \\
& \quad \left. + \left(W_{1111}^-(\mathbf{x}) \right)^2 \left(W_{2121}^+(\mathbf{x} + \hat{i}) + 2 \frac{1}{N_\tau - 1} \sum_{\tau=1}^{N_\tau-1} (2\kappa)^{2\tau} W_{1010}(\mathbf{x} + \hat{i}) \right) \right] \\
& - N_f h_{32} \frac{N_c^2}{N_c^2 - 1} \sum_{\mathbf{x},i} \left[\left(W_{2222}^+(\mathbf{x}) - 2W_{1111}(\mathbf{x}) \right) \left(W_{1111}^-(\mathbf{x} + \hat{i}) \right)^2 \right. \\
& \quad \left. + \left(W_{1111}^-(\mathbf{x}) \right)^2 \left(W_{2222}^+(\mathbf{x} + \hat{i}) - 2W_{1111}(\mathbf{x} + \hat{i}) \right) \right] \\
& + N_f h_{32} \frac{N_c}{N_c^2 - 1} \sum_{\mathbf{x},i} \left[\left(W_{2222}^+(\mathbf{x}) - 2W_{1111}(\mathbf{x}) \right) \left(W_{2222}^+(\mathbf{x} + \hat{i}) - 2W_{1111}(\mathbf{x} + \hat{i}) \right) \right. \\
& \quad \left. + \left(W_{1111}^-(\mathbf{x}) \right)^2 \left(W_{1111}^-(\mathbf{x} + \hat{i}) \right)^2 \right] \tag{A.34}
\end{aligned}$$

The second one comes from $\text{tr}_{c,d,t}^2 \left(\tilde{M}_{C_2} \right)$ in the case that both spatial loops are identical:

$$\begin{aligned}
& \frac{N_f^2}{2}\kappa^4 \sum_{\mathbf{x},i} \int [dU_i] \text{tr}_{c,d,t} \left[S_{\mathbf{x},\mathbf{x}+\hat{i}}^+ (\mathbb{1} - \kappa T)_{\mathbf{x}+\hat{i}}^{-1} S_{\mathbf{x}+\hat{i},\mathbf{x}}^- (\mathbb{1} - \kappa T)_{\mathbf{x}}^{-1} \right] \\
& \quad \text{tr}_{c,d,t} \left[S_{\mathbf{x},\mathbf{x}+\hat{i}}^+ (\mathbb{1} - \kappa T)_{\mathbf{x}+\hat{i}}^{-1} S_{\mathbf{x}+\hat{i},\mathbf{x}}^- (\mathbb{1} - \kappa T)_{\mathbf{x}}^{-1} \right] \\
& = 2N_f^2 h_{31} \sum_{\mathbf{x},i} \left[\left(W_{1111}^-(\mathbf{x}) \right)^2 \left(W_{1111}^-(\mathbf{x} + \hat{i}) \right)^2 + W_{2121}^+(\mathbf{x}) W_{2121}^+(\mathbf{x} + \hat{i}) \right. \\
& \quad + 2W_{2121}^+(\mathbf{x}) \frac{1}{N_\tau - 1} \sum_{\tau=1}^{N_\tau-1} (2\kappa)^{2\tau} W_{1010}(\mathbf{x} + \hat{i}) \\
& \quad + 2 \frac{1}{N_\tau - 1} \sum_{\tau=1}^{N_\tau-1} (2\kappa)^{2\tau} W_{1010}(\mathbf{x}) W_{2121}^+(\mathbf{x} + \hat{i}) \\
& \quad + 2 \frac{1}{N_\tau - 1} \sum_{\tau=1}^{N_\tau-1} (2\kappa)^{4\tau} W_{1010}(\mathbf{x}) W_{1010}(\mathbf{x} + \hat{i}) \\
& \quad \left. + 2(2\kappa)^{2N_\tau} W_{1010}(\mathbf{x}) W_{1010}(\mathbf{x} + \hat{i}) \right] \\
& + 2N_f^2 h_{32} \frac{N_c^2}{N_c^2 - 1} \sum_{\mathbf{x},i} \left[\left(W_{1111}^-(\mathbf{x}) \right)^2 \left(W_{1111}^-(\mathbf{x} + \hat{i}) \right)^2 \right. \\
& \quad \left. + \left(W_{2222}^+(\mathbf{x}) - 2W_{1111}(\mathbf{x}) \right) \left(W_{2222}^+(\mathbf{x} + \hat{i}) - 2W_{1111}(\mathbf{x} + \hat{i}) \right) \right] \\
& - 2N_f^2 h_{32} \frac{N_c}{N_c^2 - 1} \sum_{\mathbf{x},i} \left[\left(W_{2222}^+(\mathbf{x}) - 2W_{1111}(\mathbf{x}) \right) \left(W_{1111}^-(\mathbf{x} + \hat{i}) \right)^2 \right. \\
& \quad \left. + \left(W_{1111}^-(\mathbf{x}) \right)^2 \left(W_{2222}^+(\mathbf{x} + \hat{i}) - 2W_{1111}(\mathbf{x} + \hat{i}) \right) \right] \tag{A.35}
\end{aligned}$$

A.4.2. Three-point interaction

The main part of the three-point interaction stems from eq. (2.61) and thus starts at $\mathcal{O}(\kappa^4)$. Here, two fundamentally different geometries have to be distinguished for the further derivation. In the first case, both hops occur in the same direction i and the graph forms a straight line:

$$\begin{aligned}
& -N_f \kappa^4 \sum_{\mathbf{x}, i} \int [dU_i] \operatorname{tr}_{c,d,t} \left[S_{\mathbf{x}, \mathbf{x}+\hat{i}}^+ (\mathbb{1} - \kappa T)_{\mathbf{x}+\hat{i}}^{-1} S_{\mathbf{x}+\hat{i}, \mathbf{x}+2\hat{i}}^+ (\mathbb{1} - \kappa T)_{\mathbf{x}+2\hat{i}}^{-1} \right. \\
& \quad \left. S_{\mathbf{x}+2\hat{i}, \mathbf{x}+\hat{i}}^- (\mathbb{1} - \kappa T)_{\mathbf{x}+\hat{i}}^{-1} S_{\mathbf{x}+\hat{i}, \mathbf{x}}^- (\mathbb{1} - \kappa T)_{\mathbf{x}}^{-1} \right] \\
& = 2N_f h_{33} \frac{N_\tau - 1}{N_\tau} \sum_{\mathbf{x}, i} W_{1111}^-(\mathbf{x}) \left(W_{2121}^+(\mathbf{x} + \hat{i}) - 2 \frac{1}{N_\tau - 1} \sum_{\tau=1}^{N_\tau-1} (2\kappa)^{2\tau} W_{1010}(\mathbf{x} + \hat{i}) \right) \\
& \quad W_{1111}^-(\mathbf{x} + 2\hat{i}) \\
& - 2N_f h_{33} \frac{1}{N_\tau} \sum_{\mathbf{x}, i} W_{1111}^-(\mathbf{x}) \left(4N_c + W_{2222}^+(\mathbf{x} + \hat{i}) - 4W_{1111}^+(\mathbf{x} + \hat{i}) + 2W_{1111}(\mathbf{x} + \hat{i}) \right) \\
& \quad W_{1111}^-(\mathbf{x} + 2\hat{i})
\end{aligned} \tag{A.36}$$

In the second case, the directions i and j of the two hops are different. The graph then forms a corner Γ on the spatial lattice. We introduce the notation $\Gamma_{\bullet, \bullet, \bullet}$ to refer to the two end points $\mathbf{x}_{\bullet, \bullet}$ and the midpoint \mathbf{x}_\bullet which make up this corner. For the calculation of the effective action, one has to sum over all such corners on the spatial lattice, including every distinguishable corner only once, which is indicated by $\sum_{\{\Gamma\}}$:

$$\begin{aligned}
& -N_f \kappa^4 \sum_{\{\Gamma\}} \int [dU_i] \operatorname{tr}_{c,d,t} \left[S_{\Gamma_\bullet, \Gamma_\bullet} (\mathbb{1} - \kappa T)_{\Gamma_\bullet}^{-1} S_{\Gamma_\bullet, \Gamma_\bullet} (\mathbb{1} - \kappa T)_{\Gamma_\bullet}^{-1} S_{\Gamma_\bullet, \Gamma_\bullet} (\mathbb{1} - \kappa T)_{\Gamma_\bullet}^{-1} \right. \\
& \quad \left. S_{\Gamma_\bullet, \Gamma_\bullet} (\mathbb{1} - \kappa T)_{\Gamma_\bullet}^{-1} \right] \\
& = 2N_f h_{33} \frac{N_\tau - 1}{N_\tau} \sum_{\{\Gamma\}} W_{1111}^-(\Gamma_\bullet) W_{2121}^+(\Gamma_\bullet) W_{1111}^-(\Gamma_\bullet) \\
& - N_f h_{33} \frac{1}{N_\tau} \sum_{\{\Gamma\}} W_{1111}^-(\Gamma_\bullet) \left(4N_c + 2W_{2222}^+(\Gamma_\bullet) - 4W_{1111}^+(\Gamma_\bullet) \right) W_{1111}^-(\Gamma_\bullet).
\end{aligned} \tag{A.37}$$

An additional contribution to the three-point interaction arises from $\operatorname{tr}_{c,d,t}^2(\tilde{M}_{C_2})$ in the case that the two loops share exactly one spatial point. This is also of $\mathcal{O}(\kappa^4)$:

$$\begin{aligned}
& \frac{N_f^2}{2} \kappa^4 \sum'_{\mathbf{x}, \mathbf{y}, i, j} \int [dU_i] \operatorname{tr}_{c,d,t} \left[S_{\mathbf{x}, \mathbf{x}+\hat{i}}^+ (\mathbb{1} - \kappa T)_{\mathbf{x}+\hat{i}}^{-1} S_{\mathbf{x}+\hat{i}, \mathbf{x}}^- (\mathbb{1} - \kappa T)_{\mathbf{x}}^{-1} \right] \\
& \quad \operatorname{tr}_{c,d,t} \left[S_{\mathbf{y}, \mathbf{y}+\hat{j}}^+ (\mathbb{1} - \kappa T)_{\mathbf{y}+\hat{j}}^{-1} S_{\mathbf{y}+\hat{j}, \mathbf{y}}^- (\mathbb{1} - \kappa T)_{\mathbf{y}}^{-1} \right] \\
& = 2N_f^2 h_{33} \sum'_{\mathbf{x}, \mathbf{y}, i, j} W_{1111}^-(\mathbf{x}) W_{1111}^-(\mathbf{x} + \hat{i}) W_{1111}^-(\mathbf{y}) W_{1111}^-(\mathbf{y} + \hat{j}),
\end{aligned} \tag{A.38}$$

where the prime on the sum indicates that it is restricted to terms where $\{\mathbf{x}, \mathbf{x} + \hat{i}\}$ and $\{\mathbf{y}, \mathbf{y} + \hat{j}\}$ share exactly one point, i. e. $\sum'_{\mathbf{x}, \mathbf{y}, i, j} = \sum_{\mathbf{x}, \mathbf{y}, i, j} [\delta_{\mathbf{x}, \mathbf{y}} (1 - \delta_{i, j}) + \delta_{\mathbf{x} + \hat{i}, \mathbf{y}}]$.

A.4.3. Four-point interaction

There are only two four-point interactions to $\mathcal{O}(\kappa^4)$: The first one stems from eq. (2.61) when the spatial loop C_4 forms a square. It vanishes in the strong-coupling limit and only acquires a

A. Appendix

non-zero value if a gauge plaquette is inserted into the square, making it proportional to $\kappa^4 u$:

$$\begin{aligned}
& N_f N_c \kappa^4 u \sum_{\mathbf{x}, i \neq j} \int [dU_i] \text{tr}_{c,t} \left[U_j^\dagger(\mathbf{x} + \hat{i}) U_i^\dagger(\mathbf{x}) U_j(\mathbf{x}) U_i(\mathbf{x} + \hat{j}) \right] \\
& \quad \text{tr}_{c,d,t} \left[S_{\mathbf{x}, \mathbf{x} + \hat{i}}^+ (\mathbb{1} - \kappa T)_{\mathbf{x} + \hat{i}}^{-1} S_{\mathbf{x} + \hat{i}, \mathbf{x} + \hat{i} + \hat{j}}^+ (\mathbb{1} - \kappa T)_{\mathbf{x} + \hat{i} + \hat{j}}^{-1} \right. \\
& \quad \quad \left. S_{\mathbf{x} + \hat{i} + \hat{j}, \mathbf{x} + \hat{j}}^- (\mathbb{1} - \kappa T)_{\mathbf{x} + \hat{j}}^{-1} S_{\mathbf{x} + \hat{j}, \mathbf{x}}^- (\mathbb{1} - \kappa T)_{\mathbf{x}}^{-1} \right] \\
& = N_f h_{34} \sum_{\mathbf{x}, i \neq j} \left[(2N_c - W_{1111}^+(\mathbf{x})) (2N_c - W_{1111}^+(\mathbf{x} + \hat{i})) (2N_c - W_{1111}^+(\mathbf{x} + \hat{i} + \hat{j})) \right. \\
& \quad (2N_c - W_{1111}^+(\mathbf{x} + \hat{j})) \\
& \quad - W_{1111}^-(\mathbf{x}) W_{1111}^-(\mathbf{x} + \hat{i}) (2N_c - W_{1111}^+(\mathbf{x} + \hat{i} + \hat{j})) (2N_c - W_{1111}^+(\mathbf{x} + \hat{j})) \\
& \quad - W_{1111}^-(\mathbf{x}) (2N_c - W_{1111}^+(\mathbf{x} + \hat{i})) W_{1111}^-(\mathbf{x} + \hat{i} + \hat{j}) (2N_c - W_{1111}^+(\mathbf{x} + \hat{j})) \\
& \quad - (2N_c - W_{1111}^+(\mathbf{x})) W_{1111}^-(\mathbf{x} + \hat{i}) W_{1111}^-(\mathbf{x} + \hat{i} + \hat{j}) (2N_c - W_{1111}^+(\mathbf{x} + \hat{j})) \\
& \quad - W_{1111}^-(\mathbf{x}) (2N_c - W_{1111}^+(\mathbf{x} + \hat{i})) (2N_c - W_{1111}^+(\mathbf{x} + \hat{i} + \hat{j})) W_{1111}^-(\mathbf{x} + \hat{j}) \\
& \quad - (2N_c - W_{1111}^+(\mathbf{x})) W_{1111}^-(\mathbf{x} + \hat{i}) (2N_c - W_{1111}^+(\mathbf{x} + \hat{i} + \hat{j})) W_{1111}^-(\mathbf{x} + \hat{j}) \\
& \quad - (2N_c - W_{1111}^+(\mathbf{x})) (2N_c - W_{1111}^+(\mathbf{x} + \hat{i})) W_{1111}^-(\mathbf{x} + \hat{i} + \hat{j}) W_{1111}^-(\mathbf{x} + \hat{j}) \\
& \quad \left. + W_{1111}^-(\mathbf{x}) W_{1111}^-(\mathbf{x} + \hat{i}) W_{1111}^-(\mathbf{x} + \hat{i} + \hat{j}) W_{1111}^-(\mathbf{x} + \hat{j}) \right] \tag{A.39}
\end{aligned}$$

The second contribution comes from $\text{tr}_{c,d,t}^2(\tilde{M}_{C_2})$ in the case that the two spatial loops share no point at all. This yields the same result as eq. (A.38), but now with a different restriction on the sum: Only such terms where $\{\mathbf{x}, \mathbf{x} + \hat{i}\}$ and $\{\mathbf{y}, \mathbf{y} + \hat{j}\}$ share no point are to be considered, so that here $\sum'_{\mathbf{x}, \mathbf{y}, i, j} = \sum_{\mathbf{x}, i, j} \sum_{\mathbf{y} \notin \{\mathbf{x}, \mathbf{x} + \hat{i}\}}$.

A.5. Additional plots for static quarks

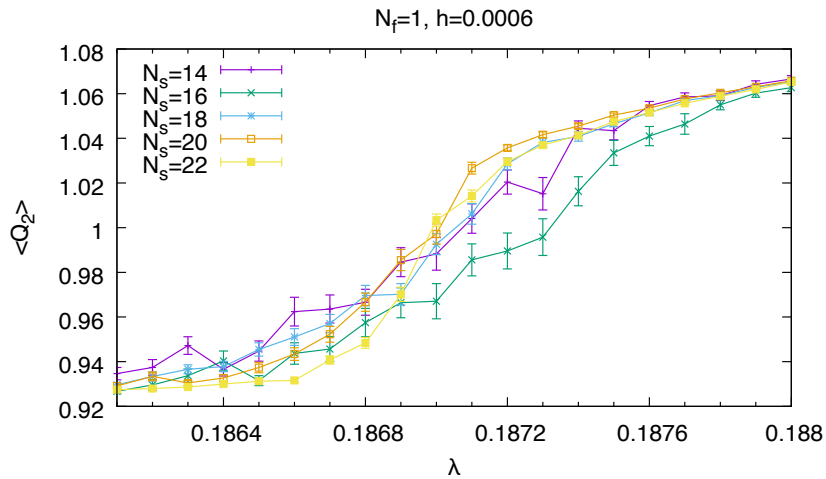


Figure A.1.: Expectation value of Q_2 for static quarks with one flavour and $h_1 = \bar{h}_1 = 0.0006$ on various volumes

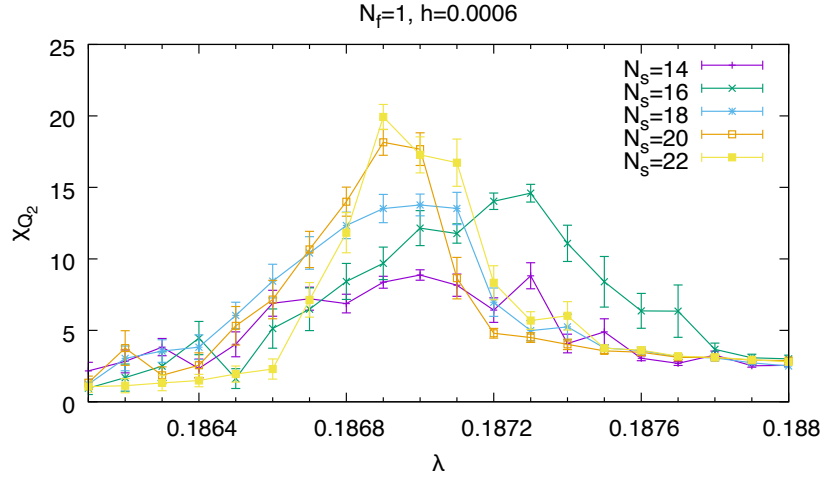


Figure A.2.: Susceptibility of Q_2 for static quarks with one flavour and $h_1 = \bar{h}_1 = 0.0006$ on various volumes

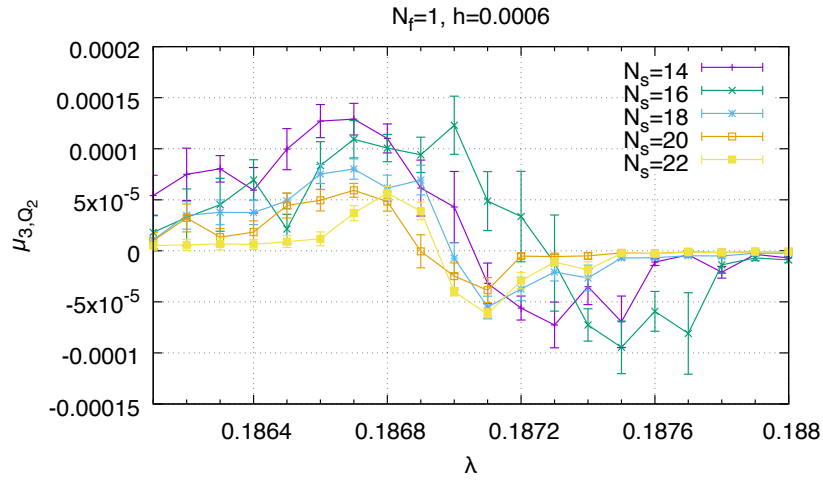


Figure A.3.: Skewness of Q_2 for static quarks with one flavour and $h_1 = \bar{h}_1 = 0.0006$ on various volumes

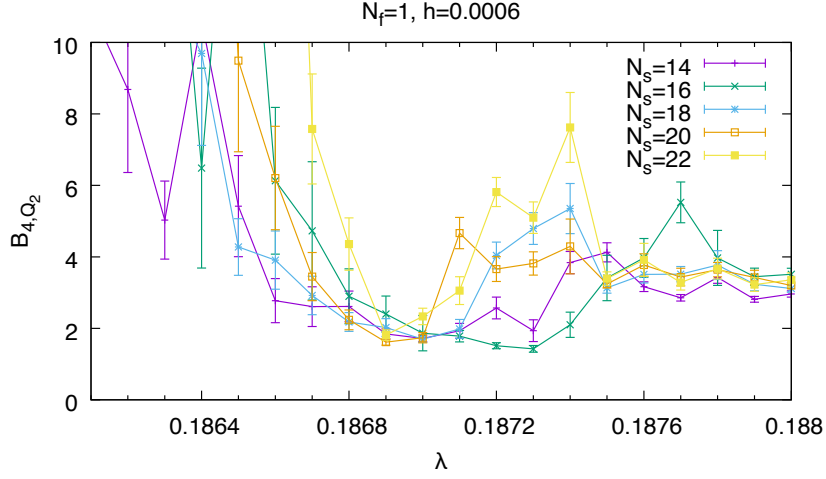
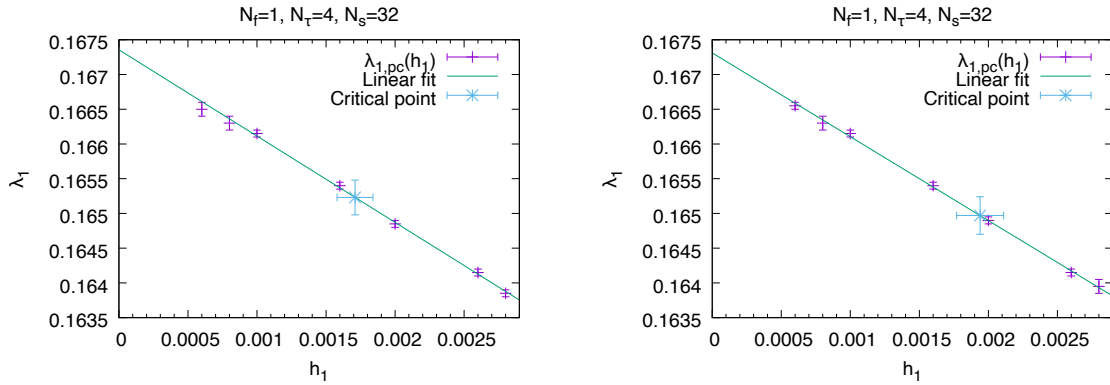


Figure A.4.: Kurtosis of Q_2 for static quarks with one flavour and $h_1 = \bar{h}_1 = 0.0006$ on various volumes

A.6. Plots using the ‘full’ implemented action

A.6.1. One-flavour theory with $N_\tau = 4$



(a) As obtained from Q_1

(b) As obtained from Q_2

Figure A.5.: The pseudo-critical line for one flavour, $N_\tau = 4$ and $N_s = 32$. Linear fits according to eqs. (3.30), (3.35) and (3.36) and the critical point eqs. (3.39) and (3.40) are also shown

A.6. Plots using the ‘full’ implemented action

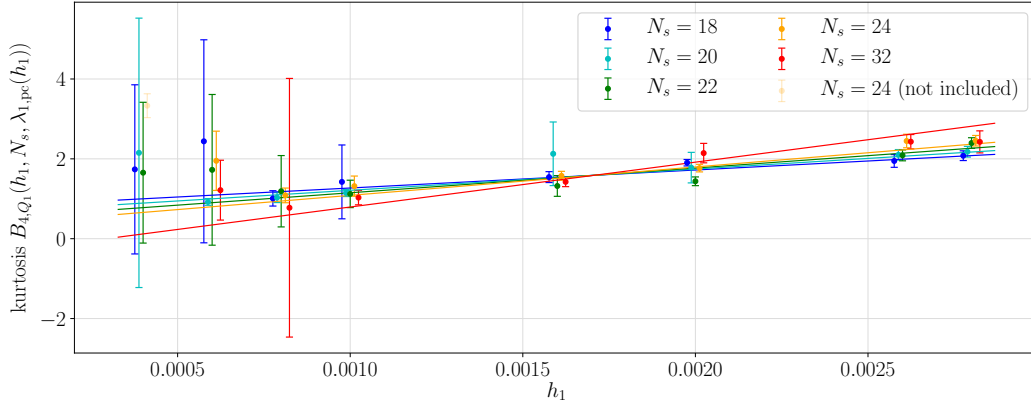


Figure A.6.: Kurtosis B_{4,Q_1} as a function of h_1 on the pseudo-critical line $\lambda_{1,\text{pc}}(h_1)$ for one flavour and $N_\tau = 4$ on various volumes

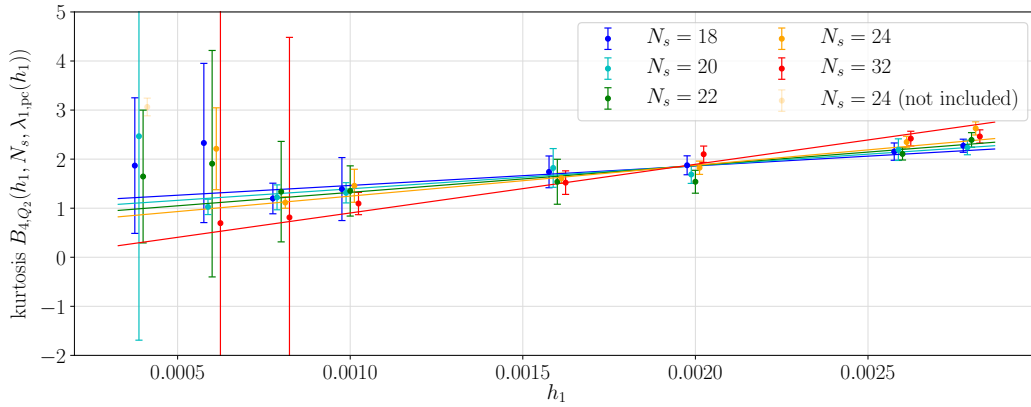


Figure A.7.: Kurtosis B_{4,Q_2} as a function of h_1 on the pseudo-critical line $\lambda_{1,\text{pc}}(h_1)$ for one flavour and $N_\tau = 4$ on various volumes

A.6.2. One-flavour theory with $N_\tau = 6$

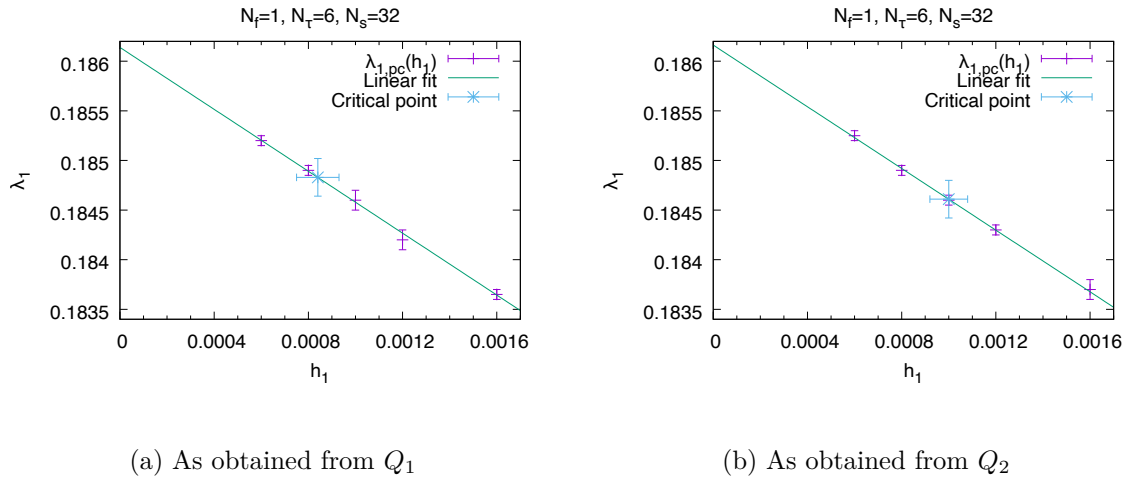


Figure A.8.: The pseudo-critical line for one flavour, $N_\tau = 6$ and $N_s = 32$. Linear fits according to eq. (3.30) and the critical point are also shown

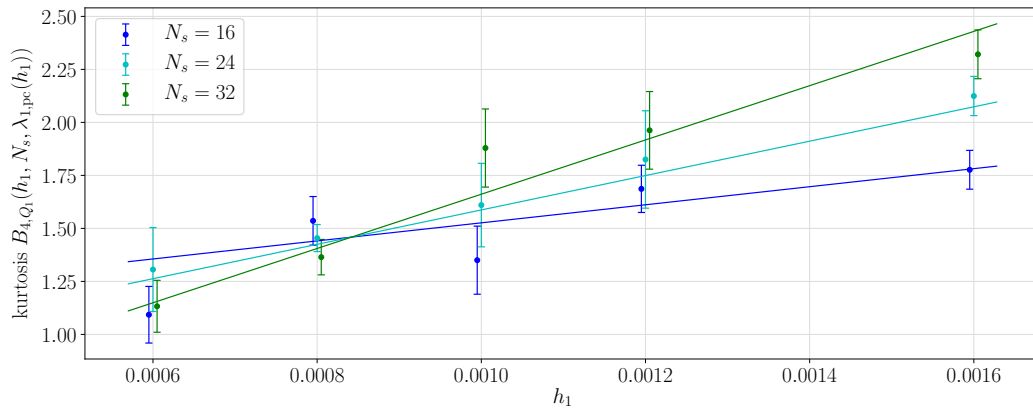


Figure A.9.: Kurtosis B_{4,Q_1} as a function of h_1 on the pseudo-critical line $\lambda_{1,pc}(h_1)$ for one flavour and $N_\tau = 6$ on various volumes

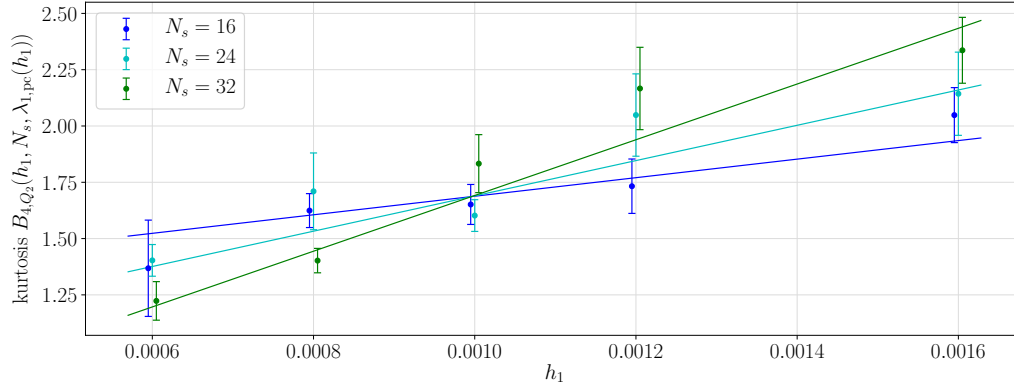
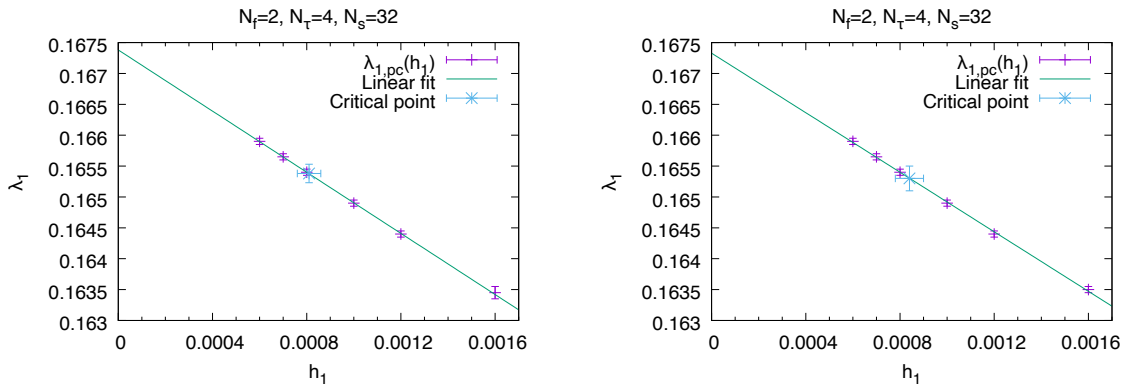


Figure A.10.: Kurtosis B_{4,Q_2} as a function of h_1 on the pseudo-critical line $\lambda_{1,pc}(h_1)$ for one flavour and $N_\tau = 6$ on various volumes

A.6.3. Two-flavour theory with $N_\tau = 4$



(a) As obtained from Q_1

(b) As obtained from Q_2

Figure A.11.: The pseudo-critical line for two flavours, $N_\tau = 4$ and $N_s = 32$. Linear fits according to eq. (3.30) and the critical point are also shown

A. Appendix

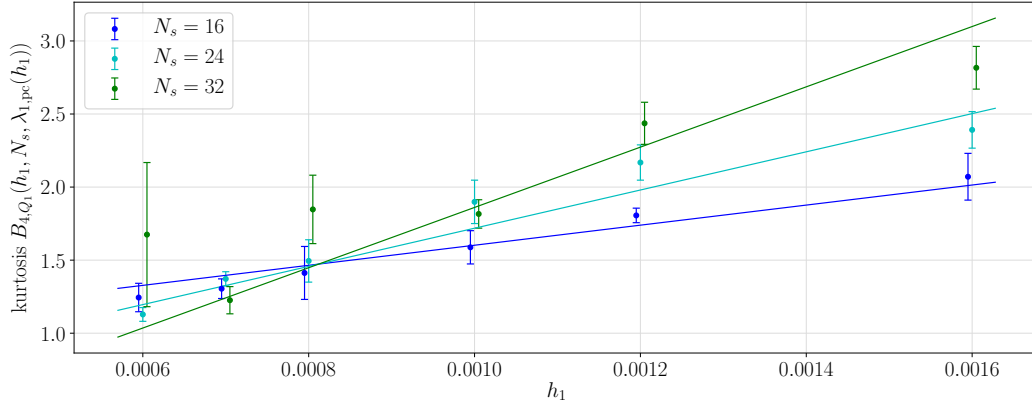


Figure A.12.: Kurtosis B_{4,Q_1} as a function of h_1 on the pseudo-critical line $\lambda_{1,\text{pc}}(h_1)$ for two flavours and $N_\tau = 4$ on various volumes

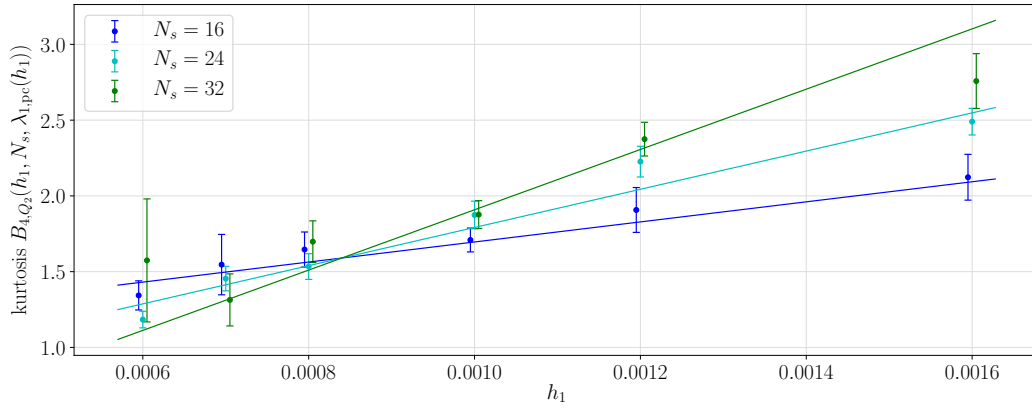
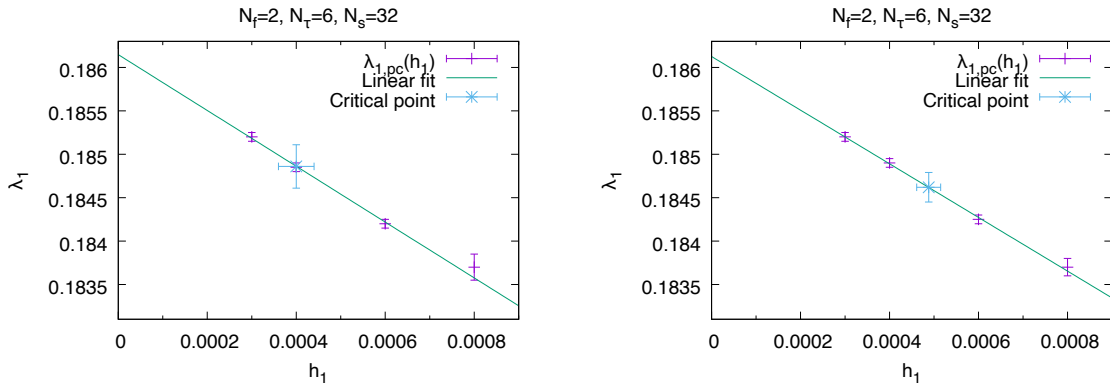


Figure A.13.: Kurtosis B_{4,Q_2} as a function of h_1 on the pseudo-critical line $\lambda_{1,\text{pc}}(h_1)$ for two flavours and $N_\tau = 4$ on various volumes

A.6.4. Two-flavour theory with $N_\tau = 6$

(a) As obtained from Q_1

(b) As obtained from Q_2

Figure A.14.: The pseudo-critical line for two flavours, $N_\tau = 6$ and $N_s = 32$. Linear fits according to eq. (3.30) and the critical point are also shown

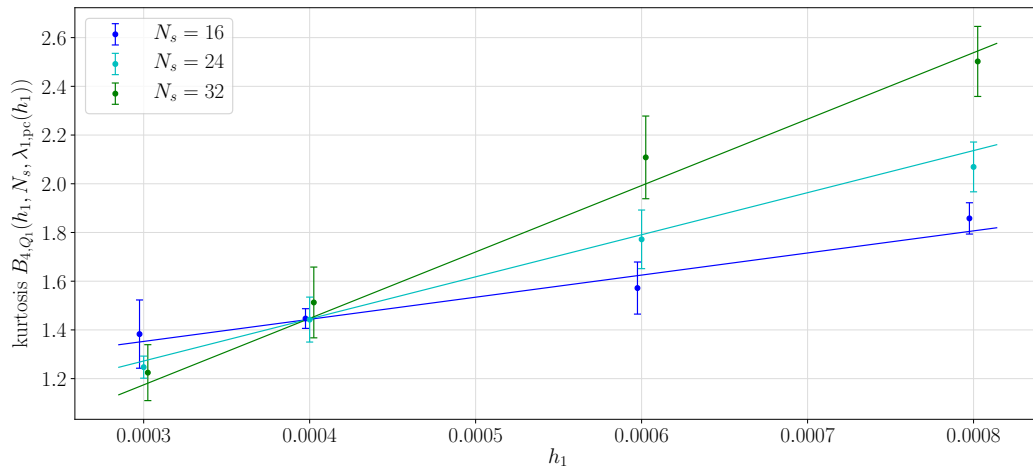


Figure A.15.: Kurtosis B_{4,Q_1} as a function of h_1 on the pseudo-critical line $\lambda_{1,pc}(h_1)$ for two flavours and $N_\tau = 6$ on various volumes

A. Appendix

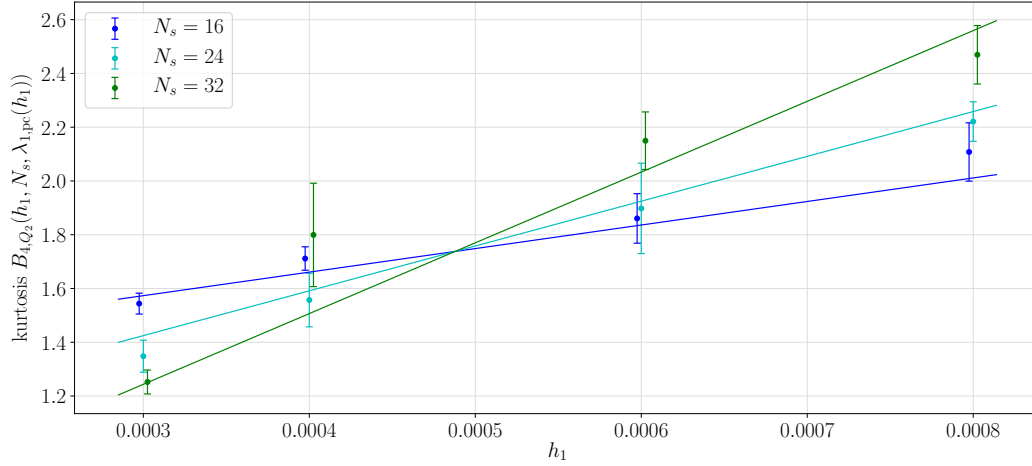


Figure A.16.: Kurtosis B_{4,Q_2} as a function of h_1 on the pseudo-critical line $\lambda_{1,pc}(h_1)$ for two flavours and $N_\tau = 6$ on various volumes

A.7. Plots for the study of the large- N_τ approximation

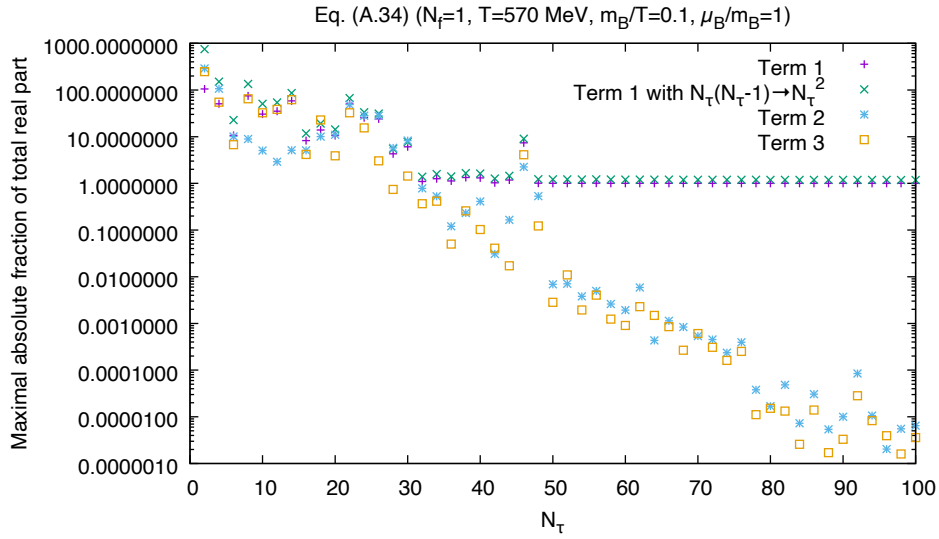


Figure A.17.: Maximal relative contributions of the different parts of eq. (A.34) to its total real part for 1000 random samples as a function of N_τ

A.7. Plots for the study of the large- N_τ approximation

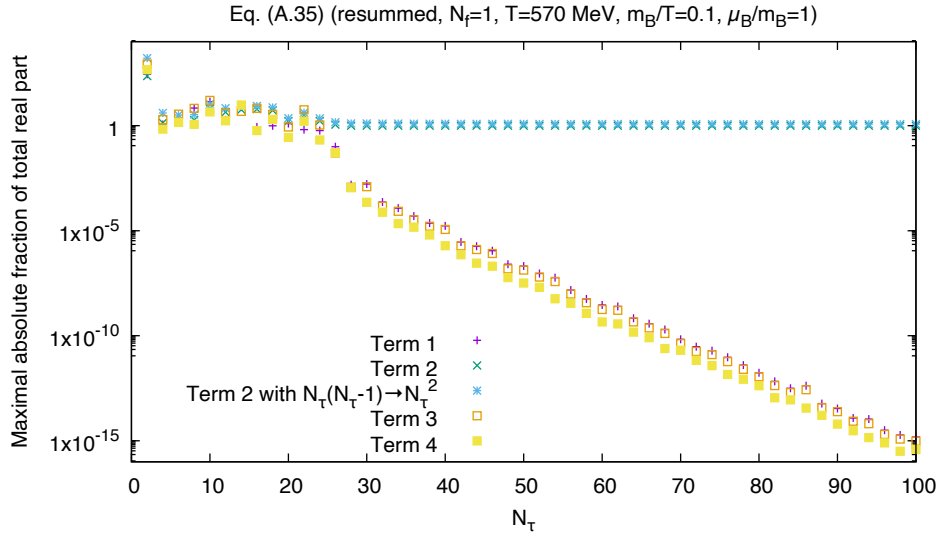


Figure A.18.: Maximal relative contributions of the different parts of eq. (A.35) (with the modifications due to the resummation) to its total real part for 1000 random samples as a function of N_τ

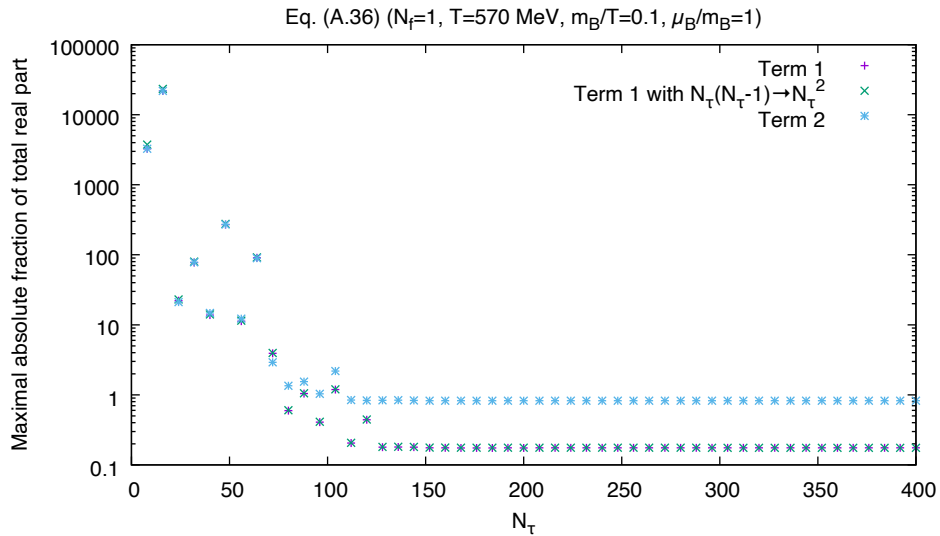


Figure A.19.: Maximal relative contributions of the different parts of eq. (A.36) to its total real part for 1000 random samples as a function of N_τ

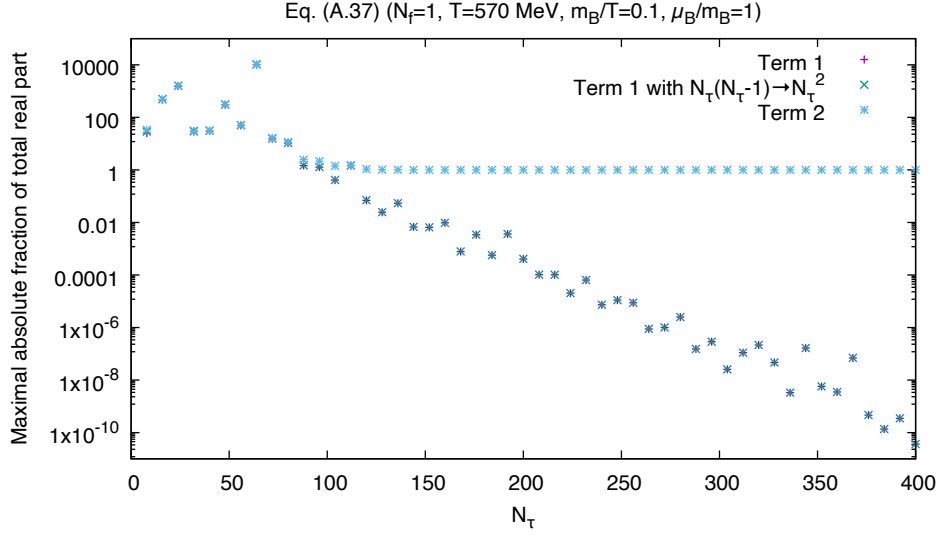


Figure A.20.: Maximal relative contributions of the different parts of eq. (A.37) to its total real part for 1000 random samples as a function of N_τ

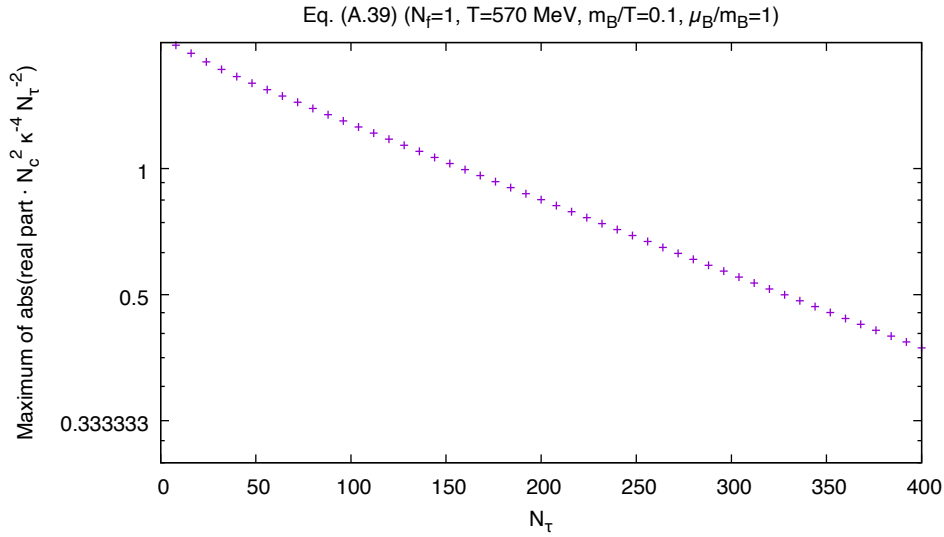


Figure A.21.: Maximum of the absolute real part of eq. (A.39), divided by $\kappa^4 N_\tau^2 / N_c^2$, for 1000 random samples as a function of N_τ

A.8. Result for the $\mathcal{O}(\kappa^6)$ -contribution to the nearest-neighbour fermion interaction

In this appendix, the $\mathcal{O}(\kappa^6)$ -contribution of the nearest-neighbour interaction to the kinetic quark determinant is shown. This corresponds to the $\mathcal{O}(\kappa^6)$ -terms in $\prod_{\{C_2\}} \det_{c,d,t} \left(\mathbb{1} - \kappa^2 \tilde{M}_{C_2} \right)^{N_f}$ as they are given in eq. (4.1). All terms are understood to be summed over the spatial position

A.8. Result for the $\mathcal{O}(\kappa^6)$ -contribution to the nearest-neighbour fermion interaction

\mathbf{x} and the direction $i = (1, 2, 3)$, as well as over the temporal coordinates τ_j . Here, differently named indices are intended to be unequal. A term that contains τ_1 and τ_2 , for instance, is summed over $\tau_1 \neq \tau_2$. The traces and determinants are taken over colour space.

$$\begin{aligned}
& - \frac{128}{5} N_f \left(2N_f^2 + 3N_f + 1 \right) \det(B(\mathbf{x}, \tau_1, \tau_1)) \det(B(\mathbf{x} + \hat{i}, \tau_1, \tau_1)) \\
& - \frac{128}{3} N_f \left(2N_f^2 + 3N_f + 1 \right) \det(B(\mathbf{x}, \tau_2, \tau_1)) \det(B(\mathbf{x} + \hat{i}, \tau_1, \tau_2)) \\
& + \text{tr}(B(\mathbf{x} + \hat{i}, \tau_1, \tau_1)) \left(\text{tr}(B(\mathbf{x}, \tau_2, \tau_2)) \left(-\frac{64}{9} N_f (N_f + 1) \text{tr}(B(\mathbf{x}, \tau_1, \tau_1) B(\mathbf{x}, \tau_1, \tau_1)) \right. \right. \\
& \qquad \qquad \qquad \left. \left. \text{tr}(B(\mathbf{x} + \hat{i}, \tau_1, \tau_2) B(\mathbf{x} + \hat{i}, \tau_2, \tau_1)) \right. \right. \\
& \qquad \left. \left. - \frac{32}{9} N_f \text{tr}(B(\mathbf{x}, \tau_1, \tau_2) B(\mathbf{x}, \tau_2, \tau_1)) \text{tr}(B(\mathbf{x} + \hat{i}, \tau_2, \tau_2) B(\mathbf{x} + \hat{i}, \tau_2, \tau_2)) \right) \right) \\
& - \frac{256}{81} N_f \text{tr}(B(\mathbf{x}, \tau_3, \tau_3)) \text{tr}(B(\mathbf{x}, \tau_1, \tau_2) B(\mathbf{x}, \tau_2, \tau_1)) \text{tr}(B(\mathbf{x} + \hat{i}, \tau_2, \tau_3) B(\mathbf{x} + \hat{i}, \tau_3, \tau_2)) \\
& + \frac{512}{27} N_f^2 \text{tr}(B(\mathbf{x}, \tau_1, \tau_3) B(\mathbf{x}, \tau_3, \tau_2) B(\mathbf{x}, \tau_2, \tau_1)) \text{tr}(B(\mathbf{x} + \hat{i}, \tau_3, \tau_3)) \\
& \qquad \qquad \qquad \text{tr}(B(\mathbf{x} + \hat{i}, \tau_1, \tau_2) B(\mathbf{x} + \hat{i}, \tau_2, \tau_1)) \\
& - \frac{16}{45} N_f \left(20N_f^2 + 12N_f + 5 \right) \text{tr}(B(\mathbf{x}, \tau_1, \tau_1) B(\mathbf{x}, \tau_1, \tau_1) B(\mathbf{x}, \tau_1, \tau_1)) \\
& \qquad \qquad \qquad \text{tr}(B(\mathbf{x} + \hat{i}, \tau_1, \tau_1) B(\mathbf{x} + \hat{i}, \tau_1, \tau_1) B(\mathbf{x} + \hat{i}, \tau_1, \tau_1)) \\
& + \text{tr}^3(B(\mathbf{x}, \tau_1, \tau_1)) \left(-\frac{16}{45} N_f^2 (10N_f + 3) \text{tr}^3(B(\mathbf{x} + \hat{i}, \tau_1, \tau_1)) \right. \\
& \qquad + \frac{32}{15} N_f \left(2N_f^2 + 5N_f + 1 \right) \text{tr}(B(\mathbf{x} + \hat{i}, \tau_1, \tau_1) B(\mathbf{x} + \hat{i}, \tau_1, \tau_1)) \text{tr}(B(\mathbf{x} + \hat{i}, \tau_1, \tau_1)) \\
& \qquad \left. - \frac{32}{45} N_f (6N_f + 5) \text{tr}(B(\mathbf{x} + \hat{i}, \tau_1, \tau_1) B(\mathbf{x} + \hat{i}, \tau_1, \tau_1) B(\mathbf{x} + \hat{i}, \tau_1, \tau_1)) \right) \\
& - \frac{32}{9} N_f \left(4N_f^2 + N_f + 1 \right) \text{tr}(B(\mathbf{x}, \tau_1, \tau_1) B(\mathbf{x}, \tau_1, \tau_2) B(\mathbf{x}, \tau_2, \tau_1)) \\
& \qquad \qquad \qquad \text{tr}(B(\mathbf{x} + \hat{i}, \tau_1, \tau_1) B(\mathbf{x} + \hat{i}, \tau_1, \tau_2) B(\mathbf{x} + \hat{i}, \tau_2, \tau_1)) \\
& + \text{tr}^2(B(\mathbf{x}, \tau_1, \tau_1)) \left(-\frac{64}{9} N_f^3 \text{tr}(B(\mathbf{x}, \tau_2, \tau_2)) \text{tr}^2(B(\mathbf{x} + \hat{i}, \tau_1, \tau_1)) \text{tr}(B(\mathbf{x} + \hat{i}, \tau_2, \tau_2)) \right. \\
& \qquad + \text{tr}(B(\mathbf{x}, \tau_2, \tau_2)) \left(\frac{128}{27} N_f^3 \text{tr}(B(\mathbf{x} + \hat{i}, \tau_2, \tau_2)) \text{tr}(B(\mathbf{x} + \hat{i}, \tau_1, \tau_1) B(\mathbf{x} + \hat{i}, \tau_1, \tau_1)) \right. \\
& \qquad \left. \left. - \frac{64}{9} N_f (N_f + 1) \text{tr}(B(\mathbf{x} + \hat{i}, \tau_1, \tau_1) B(\mathbf{x} + \hat{i}, \tau_1, \tau_2) B(\mathbf{x} + \hat{i}, \tau_2, \tau_1)) \right) \right) \\
& \qquad + \frac{64}{27} N_f (9N_f + 1) \text{tr}(B(\mathbf{x}, \tau_2, \tau_2)) \text{tr}(B(\mathbf{x} + \hat{i}, \tau_1, \tau_1)) \text{tr}(B(\mathbf{x} + \hat{i}, \tau_1, \tau_2) B(\mathbf{x} + \hat{i}, \tau_2, \tau_1)) \\
& - \frac{16}{9} N_f \left(4N_f^2 + 2N_f + 1 \right) \text{tr}(B(\mathbf{x}, \tau_1, \tau_2) B(\mathbf{x}, \tau_2, \tau_2) B(\mathbf{x}, \tau_2, \tau_1)) \\
& \qquad \qquad \qquad \text{tr}(B(\mathbf{x} + \hat{i}, \tau_1, \tau_2) B(\mathbf{x} + \hat{i}, \tau_2, \tau_2) B(\mathbf{x} + \hat{i}, \tau_2, \tau_1))
\end{aligned}$$

A. Appendix

$$\begin{aligned}
& + \text{tr}(B(\mathbf{x}, \tau_2, \tau_2)) \left(\frac{32}{27} N_f (4N_f^2 + 18N_f + 1) \text{tr}(B(\mathbf{x}, \tau_1, \tau_2)B(\mathbf{x}, \tau_2, \tau_1)) \right. \\
& \qquad \qquad \qquad \left. \text{tr}(B(\mathbf{x} + \hat{i}, \tau_1, \tau_2)B(\mathbf{x} + \hat{i}, \tau_2, \tau_2)B(\mathbf{x} + \hat{i}, \tau_2, \tau_1)) \right. \\
& + \text{tr}(B(\mathbf{x} + \hat{i}, \tau_2, \tau_2)) \left(-\frac{64}{9} N_f^3 \text{tr}(B(\mathbf{x}, \tau_1, \tau_1)B(\mathbf{x}, \tau_1, \tau_1)) \text{tr}(B(\mathbf{x} + \hat{i}, \tau_1, \tau_1)B(\mathbf{x} + \hat{i}, \tau_1, \tau_1)) \right. \\
& \quad \left. - \frac{16}{9} N_f (4N_f^2 + 2N_f + 1) \text{tr}(B(\mathbf{x}, \tau_1, \tau_2)B(\mathbf{x}, \tau_2, \tau_1)) \text{tr}(B(\mathbf{x} + \hat{i}, \tau_1, \tau_2)B(\mathbf{x} + \hat{i}, \tau_2, \tau_1)) \right) \\
& - \frac{128}{81} N_f \text{tr}(B(\mathbf{x}, \tau_1, \tau_3)B(\mathbf{x}, \tau_3, \tau_1)) \text{tr}(B(\mathbf{x} + \hat{i}, \tau_3, \tau_3)) \text{tr}(B(\mathbf{x} + \hat{i}, \tau_1, \tau_2)B(\mathbf{x} + \hat{i}, \tau_2, \tau_1)) \\
& + \frac{64}{27} N_f (9N_f + 1) \text{tr}(B(\mathbf{x}, \tau_1, \tau_1)B(\mathbf{x}, \tau_1, \tau_1)) \text{tr}(B(\mathbf{x} + \hat{i}, \tau_1, \tau_1)B(\mathbf{x} + \hat{i}, \tau_1, \tau_2)B(\mathbf{x} + \hat{i}, \tau_2, \tau_1)) \\
& - \frac{128}{81} N_f \text{tr}(B(\mathbf{x}, \tau_1, \tau_2)B(\mathbf{x}, \tau_2, \tau_3)B(\mathbf{x}, \tau_3, \tau_1)) \text{tr}(B(\mathbf{x} + \hat{i}, \tau_1, \tau_2)B(\mathbf{x} + \hat{i}, \tau_2, \tau_3)B(\mathbf{x} + \hat{i}, \tau_3, \tau_1)) \\
& - \frac{512}{81} N_f^3 \text{tr}(B(\mathbf{x}, \tau_1, \tau_3)B(\mathbf{x}, \tau_3, \tau_2)B(\mathbf{x}, \tau_2, \tau_1)) \text{tr}(B(\mathbf{x} + \hat{i}, \tau_1, \tau_2)B(\mathbf{x} + \hat{i}, \tau_2, \tau_3)B(\mathbf{x} + \hat{i}, \tau_3, \tau_1)) \\
& + \text{tr}(B(\mathbf{x}, \tau_1, \tau_1)) \left(\frac{64}{15} N_f (2N_f^2 + 5N_f + 1) \text{tr}(B(\mathbf{x}, \tau_1, \tau_1)B(\mathbf{x}, \tau_1, \tau_1)) \right. \\
& \qquad \qquad \qquad \left. \text{tr}(B(\mathbf{x} + \hat{i}, \tau_1, \tau_1)B(\mathbf{x} + \hat{i}, \tau_1, \tau_1)B(\mathbf{x} + \hat{i}, \tau_1, \tau_1)) \right. \\
& + \frac{64}{27} N_f (4N_f^2 + 9N_f + 1) \text{tr}(B(\mathbf{x}, \tau_1, \tau_2)B(\mathbf{x}, \tau_2, \tau_1)) \\
& \qquad \qquad \qquad \left. \text{tr}(B(\mathbf{x} + \hat{i}, \tau_1, \tau_1)B(\mathbf{x} + \hat{i}, \tau_1, \tau_2)B(\mathbf{x} + \hat{i}, \tau_2, \tau_1)) \right) \\
& + \text{tr}(B(\mathbf{x} + \hat{i}, \tau_1, \tau_1)) \left(-\frac{256}{27} N_f^3 \text{tr}(B(\mathbf{x}, \tau_2, \tau_3)B(\mathbf{x}, \tau_3, \tau_2)) \text{tr}(B(\mathbf{x} + \hat{i}, \tau_2, \tau_3)B(\mathbf{x} + \hat{i}, \tau_3, \tau_2)) \right. \\
& - \frac{16}{9} N_f^2 (2N_f + 1) \text{tr}(B(\mathbf{x}, \tau_2, \tau_2)B(\mathbf{x}, \tau_2, \tau_2)) \text{tr}(B(\mathbf{x} + \hat{i}, \tau_2, \tau_2)B(\mathbf{x} + \hat{i}, \tau_2, \tau_2)) \\
& - \frac{16}{15} N_f (10N_f^2 + 9N_f + 5) \text{tr}(B(\mathbf{x}, \tau_1, \tau_1)B(\mathbf{x}, \tau_1, \tau_1)) \text{tr}(B(\mathbf{x} + \hat{i}, \tau_1, \tau_1)B(\mathbf{x} + \hat{i}, \tau_1, \tau_1)) \\
& - \frac{32}{9} N_f (4N_f^2 + N_f + 1) \text{tr}(B(\mathbf{x}, \tau_1, \tau_2)B(\mathbf{x}, \tau_2, \tau_1)) \text{tr}(B(\mathbf{x} + \hat{i}, \tau_1, \tau_2)B(\mathbf{x} + \hat{i}, \tau_2, \tau_1)) \\
& + \text{tr}^2(B(\mathbf{x}, \tau_2, \tau_2)) \left(\frac{32}{27} N_f^2 (2N_f + 9) \text{tr}(B(\mathbf{x} + \hat{i}, \tau_2, \tau_2)B(\mathbf{x} + \hat{i}, \tau_2, \tau_2)) \right. \\
& \quad \left. - \frac{16}{9} N_f^2 (2N_f + 1) \text{tr}^2(B(\mathbf{x} + \hat{i}, \tau_2, \tau_2)) \right) \\
& + \text{tr}(B(\mathbf{x}, \tau_2, \tau_2)) \left(\frac{256}{27} N_f^2 \text{tr}(B(\mathbf{x}, \tau_3, \tau_3)) \text{tr}(B(\mathbf{x} + \hat{i}, \tau_2, \tau_3)B(\mathbf{x} + \hat{i}, \tau_3, \tau_2)) \right. \\
& \quad \left. - \frac{256}{81} N_f^3 \text{tr}(B(\mathbf{x}, \tau_3, \tau_3)) \text{tr}(B(\mathbf{x} + \hat{i}, \tau_2, \tau_2)) \text{tr}(B(\mathbf{x} + \hat{i}, \tau_3, \tau_3)) \right) \\
& + \text{tr}^2(B(\mathbf{x}, \tau_2, \tau_2)) \left(\frac{32}{27} N_f \text{tr}(B(\mathbf{x} + \hat{i}, \tau_2, \tau_2)) \text{tr}(B(\mathbf{x} + \hat{i}, \tau_1, \tau_2)B(\mathbf{x} + \hat{i}, \tau_2, \tau_1)) \right. \\
& \quad \left. - \frac{32}{9} N_f \text{tr}(B(\mathbf{x} + \hat{i}, \tau_1, \tau_2)B(\mathbf{x} + \hat{i}, \tau_2, \tau_2)B(\mathbf{x} + \hat{i}, \tau_2, \tau_1)) \right) \\
& - \frac{256}{81} N_f \text{tr}(B(\mathbf{x}, \tau_3, \tau_3)) \text{tr}(B(\mathbf{x}, \tau_2, \tau_2)) \text{tr}(B(\mathbf{x} + \hat{i}, \tau_1, \tau_2)B(\mathbf{x} + \hat{i}, \tau_2, \tau_3)B(\mathbf{x} + \hat{i}, \tau_3, \tau_1)) \\
& + \frac{32}{27} N_f \text{tr}(B(\mathbf{x}, \tau_2, \tau_2)B(\mathbf{x}, \tau_2, \tau_2)) \text{tr}(B(\mathbf{x} + \hat{i}, \tau_1, \tau_2)B(\mathbf{x} + \hat{i}, \tau_2, \tau_2)B(\mathbf{x} + \hat{i}, \tau_2, \tau_1)) \left. \right)
\end{aligned}$$

Bibliography

- [1] Christian S. Fischer. ‘QCD at finite temperature and chemical potential from Dyson-Schwinger equations’. In: *Progress in Particle and Nuclear Physics* 105 (Mar. 2019), pp. 1–60. DOI: 10.1016/j.pnnp.2019.01.002. arXiv: 1810.12938 [hep-ph].
- [2] Michael Edward Peskin and Daniel V. Schroeder. *An Introduction to Quantum Field Theory*. Student Economy Edition. Frontiers in Physics. Boca Raton: CRC, 2018. URL: <https://ebookcentral.proquest.com/lib/senc/detail.action?docID=5371981>.
- [3] István Montvay and Gernot Münster. *Quantum Fields on a Lattice*. Cambridge monographs on mathematical physics. Cambridge: Cambridge University Press, 1994.
- [4] Christof Gattringer and Christian B. Lang. *Quantum Chromodynamics on the Lattice. An Introductory Presentation*. Vol. 788. Lecture Notes in Physics. Berlin, Heidelberg: Springer, 2010. DOI: 10.1007/978-3-642-01850-3.
- [5] Kenneth G. Wilson. ‘Confinement of quarks’. In: *Physical Review D: Particles and Fields* 10.8 (Oct. 1974), pp. 2445–2459. DOI: 10.1103/PhysRevD.10.2445.
- [6] Kenneth G. Wilson. ‘Quarks and Strings on a Lattice’. In: *New Phenomena in Subnuclear Physics: Part A*. Ed. by Antonino Zichichi. Vol. 13. The Subnuclear Series. Boston, MA: Springer, 1977, pp. 69–142. DOI: 10.1007/978-1-4613-4208-3_6.
- [7] Mathias Neuman. ‘Effective Theory for Heavy Quark QCD at Finite Temperature and Density with Stochastic Quantization’. PhD thesis. Frankfurt am Main: Johann Wolfgang Goethe-Universität Frankfurt, 2015.
- [8] Jens Langelage, Stefano Lottini and Owe Philipsen. ‘Centre symmetric 3d effective actions for thermal $SU(N)$ Yang-Mills from strong coupling series’. In: *Journal of High Energy Physics* 2011.2 (Feb. 2011), p. 57. DOI: 10.1007/JHEP02(2011)057. arXiv: 1010.0951 [hep-lat]. Erratum-ibid. [31].
- [9] Alexander S. Christensen, Joyce C. Myers and Peter D. Pedersen. ‘Large N lattice QCD and its extended strong-weak connection to the hypersphere’. In: *Journal of High Energy Physics* 2014.2 (Feb. 2014), p. 28. DOI: 10.1007/JHEP02(2014)028. arXiv: 1312.3519 [hep-lat].
- [10] Jens Langelage, Mathias Neuman and Owe Philipsen. ‘Heavy dense QCD and nuclear matter from an effective lattice theory’. In: *Journal of High Energy Physics* 2014.9 (Sept. 2014), p. 131. DOI: 10.1007/JHEP09(2014)131. arXiv: 1403.4162 [hep-lat].
- [11] Tobias Rindlisbacher and Philippe de Forcrand. ‘Two-Flavor Lattice QCD with a Finite Density of Heavy Quarks: Heavy-Dense Limit and “Particle-Hole” Symmetry’. In: *Journal of High Energy Physics* 2016.2 (Feb. 2016), p. 51. DOI: 10.1007/JHEP02(2016)051. arXiv: 1509.00087 [hep-lat].
- [12] Giuseppe Gagliardi and Wolfgang Unger. ‘Towards a Dual Representation of Lattice QCD’. In: *Proceedings of The 36th Annual International Symposium on Lattice Field Theory — PoS(LATTICE2018)*. Vol. 334. SISSA, May 2019, p. 224. DOI: 10.22323/1.334.0224. arXiv: 1811.02817 [hep-lat].

- [13] Alena Schön. ‘Effective heavy quark theory of strong coupling lattice QCD in 1+1 dimensions’. MA thesis. Frankfurt am Main: Johann Wolfgang Goethe-Universität Frankfurt, Aug. 2018.
- [14] Peter Lancaster. *Theory of Matrices*. New York, London: Academic Press, 1969.
- [15] E. Terry Tomboulis. ‘Chiral symmetry restoration at large chemical potential in strongly coupled $SU(N)$ gauge theories’. In: *Journal of Mathematical Physics* 54.12 (Dec. 2013), p. 122301. DOI: 10.1063/1.4837115. arXiv: 1304.4678 [hep-lat].
- [16] John Bartholomew et al. ‘Effects of quarks on $SU(N)$ deconfinement phase transitions’. In: *Physics Letters B* 133.3 (Dec. 1983), pp. 218–220. DOI: 10.1016/0370-2693(83)90564-6.
- [17] Alessandro Sciarra. ‘The QCD phase diagram at purely imaginary chemical potential from the lattice’. PhD thesis. Frankfurt am Main: Johann Wolfgang Goethe-Universität Frankfurt, 2016.
- [18] Michael Fromm et al. ‘The QCD deconfinement transition for heavy quarks and all baryon chemical potentials’. In: *Journal of High Energy Physics* 2012.1 (Jan. 2012), p. 42. DOI: 10.1007/JHEP01(2012)042. arXiv: 1111.4953 [hep-lat].
- [19] Kurt Binder. ‘Finite Size Scaling Analysis of Ising Model Block Distribution Functions’. In: *Zeitschrift für Physik B Condensed Matter* 43.2 (June 1981), pp. 119–140. DOI: 10.1007/BF01293604.
- [20] Mark G. Alford et al. ‘Solution of the Complex Action Problem in the Potts Model for Dense QCD’. In: *Nuclear Physics B* 602.1 (May 2001), pp. 61–86. DOI: 10.1016/S0550-3213(01)00068-2. arXiv: hep-lat/0101012.
- [21] Georg Bergner, Jens Langelage and Owe Philipsen. ‘Numerical corrections to the strong coupling effective Polyakov-line action for finite T Yang-Mills theory’. In: *Journal of High Energy Physics* 2015.11 (Nov. 2015), p. 10. DOI: 10.1007/JHEP11(2015)010. arXiv: 1505.01021 [hep-lat].
- [22] Shinji Ejiri et al. (WHOT-QCD Collaboration). ‘End point of the first-order phase transition of QCD in the heavy quark region by reweighting from quenched QCD’. In: *Physical Review D: Particles and Fields* 101.5 (Mar. 2020), p. 054505. DOI: 10.1103/PhysRevD.101.054505. arXiv: 1912.10500 [hep-lat].
- [23] Francesca Cuteri et al. ‘The deconfinement critical point of lattice QCD with $N_f = 2$ Wilson fermions’. Sept. 2020. arXiv: 2009.14033 [hep-lat].
- [24] Jonas Rylund Glesaaen. ‘Heavy Quark QCD at Finite Temperature and Density Using an Effective Theory’. PhD thesis. Frankfurt am Main: Johann Wolfgang Goethe-Universität Frankfurt, 2016.
- [25] Leonard C. Carlitz, D. P. Roselle and Richard A. Scoville. ‘Permutations and Sequences with Repetitions by Number of Increases’. In: *Journal of Combinatorial Theory* 1.3 (1966), pp. 350–374. DOI: 10.1016/S0021-9800(66)80057-1.
- [26] David C. Wood. *The Computation of Polylogarithms*. Tech. rep. 15-92*. University of Kent, Canterbury, UK: University of Kent, Computing Laboratory, June 1992, pp. 182–196. URL: <http://www.cs.kent.ac.uk/pubs/1992/110>.
- [27] Michael Creutz. ‘On invariant integration over $SU(N)$ ’. In: *Journal of Mathematical Physics* 19.10 (Oct. 1978), p. 2043. DOI: 10.1063/1.523581.
- [28] Karl-Erik Eriksson, N. Svartholm and Bo-Sture K. Skagerstam. ‘On invariant group integrals in lattice QCD’. In: *Journal of Mathematical Physics* 22.10 (Oct. 1981), pp. 2276–2278. DOI: 10.1063/1.524760.

- [29] Benoît Collins. ‘Moments and Cumulants of Polynomial Random Variables on Unitary Groups, the Itzykson-Zuber Integral, and Free Probability’. In: *International Mathematics Research Notices* 2003.17 (Jan. 2003), pp. 953–982. DOI: 10.1155/S107379280320917X. arXiv: math-ph/0205010.
- [30] Jean-Bernard Zuber. ‘Revisiting $SU(N)$ integrals’. In: *Journal of Physics A: Mathematical and Theoretical* 50.1 (Nov. 2016), p. 015203. DOI: 10.1088/1751-8113/50/1/015203. arXiv: 1611.00236 [math-ph].
- [31] Jens Langelage, Stefano Lottini and Owe Philipsen. ‘Erratum: centre symmetric 3d effective actions for thermal $SU(N)$ Yang-Mills from strong coupling series’. In: *Journal of High Energy Physics* 2011.7 (July 2011), p. 14. DOI: 10.1007/JHEP07(2011)014.

List of Figures

Logo Goethe-Uni from https://de.wikipedia.org/wiki/Datei:Goethe-Logo.svg	1
1.1. Sketch of the QCD phase diagram in the temperature and baryon chemical potential plane [1]	6
2.1. Illustration of the Wick rotation, indicated by curved arrows (adapted from [3])	8
2.2. The four link variables which build up the plaquette $U_{\mu\nu}(x)$. The circle indicates the order that the links are run through in the plaquette [4]	10
2.3. Illustration of the fractional Wilson lines eqs. (2.49) and (2.50) which appear in the static propagator. $W_{\mathbf{x}}$ always describes propagation in positive time direction, $W_{\mathbf{x}}^\dagger$ in negative time direction. Earlier time slices can be reached by crossing the antiperiodic boundaries of the lattice	16
3.1. The Polyakov loop potential for SU(3) $V_{\mathbf{x}}$ induced by the change of the integration measure (cf. eq. (3.2))	25
3.2. The adaptive stepsize function eq. (3.12) for an old stepsize of $\varepsilon = 0.2$. The orange area indicates the tolerable interval for the acceptance rate	27
3.3. Sub-lattices and associated CPU cores in two dimensions with $N_s = 8$. The sites which are updated simultaneously for one possible update are marked in red	28
3.4. The phase structure of Lattice QCD at zero chemical potential	30
3.5. Integrated autocorrelation time eq. (3.23) for the observable Q_2 (cf. eq. (3.15)) measured every 150 sweeps close to the phase transition	32
3.6. Integrated autocorrelation time eq. (3.23) for the observable Q_2 (cf. eq. (3.15)) measured every 150 sweeps far away from the phase transition	33
3.7. Error analysis by binning and Jackknife for the skewness of Q_2 with measurements every 150 sweeps close to the phase transition	34
3.8. Error analysis by binning and Jackknife for the skewness of Q_2 with measurements every 150 sweeps far away from the phase transition	35
3.9. Sketch of the phase diagram for the effective theory at $\mu = 0$ and given N_f, N_τ [18]	35
3.10. The pseudo-critical line for static quarks with one flavour and $N_s = 22$. A linear fit according to eqs. (3.30) and (3.31) and the critical point eq. (3.34) are also shown	37
3.11. Kurtosis B_{4,Q_2} as a function of h on the pseudo-critical line $\lambda_{\text{pc}}(h)$ for static quarks with one flavour on various volumes	38
3.12. Skewness of Q_2 for pure gauge theory with two couplings and fixed $\lambda_2 = 0.0288$ on various volumes	39
3.13. Histograms of Q_2 for two different simulations with one flavour, $N_\tau = 4$ and $N_s = 24$ in the minimum of B_{4,Q_2}	40
3.14. Chemical potential in lattice units as a function of N_τ for constant baryon chemical potential $\mu_B = m_B = 0.1T = 57 \text{ MeV}$	46

3.15.	The fermionic couplings κ and h_1 as a function of N_τ for constant temperature $T = 570$ MeV and baryon mass $m_B = 0.1T$ at $\mu_B = m_B$	48
4.1.	Illustration of the physically distinct particle configurations for the $\mathcal{O}(\kappa^6)$ -contribution to the nearest-neighbour interaction	51
A.1.	Expectation value of Q_2 for static quarks with one flavour and $h_1 = \bar{h}_1 = 0.0006$ on various volumes	74
A.2.	Susceptibility of Q_2 for static quarks with one flavour and $h_1 = \bar{h}_1 = 0.0006$ on various volumes	75
A.3.	Skewness of Q_2 for static quarks with one flavour and $h_1 = \bar{h}_1 = 0.0006$ on various volumes	75
A.4.	Kurtosis of Q_2 for static quarks with one flavour and $h_1 = \bar{h}_1 = 0.0006$ on various volumes	76
A.5.	The pseudo-critical line for one flavour, $N_\tau = 4$ and $N_s = 32$. Linear fits according to eqs. (3.30), (3.35) and (3.36) and the critical point eqs. (3.39) and (3.40) are also shown	76
A.6.	Kurtosis B_{4,Q_1} as a function of h_1 on the pseudo-critical line $\lambda_{1,\text{pc}}(h_1)$ for one flavour and $N_\tau = 4$ on various volumes	77
A.7.	Kurtosis B_{4,Q_2} as a function of h_1 on the pseudo-critical line $\lambda_{1,\text{pc}}(h_1)$ for one flavour and $N_\tau = 4$ on various volumes	77
A.8.	The pseudo-critical line for one flavour, $N_\tau = 6$ and $N_s = 32$. Linear fits according to eq. (3.30) and the critical point are also shown	78
A.9.	Kurtosis B_{4,Q_1} as a function of h_1 on the pseudo-critical line $\lambda_{1,\text{pc}}(h_1)$ for one flavour and $N_\tau = 6$ on various volumes	78
A.10.	Kurtosis B_{4,Q_2} as a function of h_1 on the pseudo-critical line $\lambda_{1,\text{pc}}(h_1)$ for one flavour and $N_\tau = 6$ on various volumes	79
A.11.	The pseudo-critical line for two flavours, $N_\tau = 4$ and $N_s = 32$. Linear fits according to eq. (3.30) and the critical point are also shown	79
A.12.	Kurtosis B_{4,Q_1} as a function of h_1 on the pseudo-critical line $\lambda_{1,\text{pc}}(h_1)$ for two flavours and $N_\tau = 4$ on various volumes	80
A.13.	Kurtosis B_{4,Q_2} as a function of h_1 on the pseudo-critical line $\lambda_{1,\text{pc}}(h_1)$ for two flavours and $N_\tau = 4$ on various volumes	80
A.14.	The pseudo-critical line for two flavours, $N_\tau = 6$ and $N_s = 32$. Linear fits according to eq. (3.30) and the critical point are also shown	81
A.15.	Kurtosis B_{4,Q_1} as a function of h_1 on the pseudo-critical line $\lambda_{1,\text{pc}}(h_1)$ for two flavours and $N_\tau = 6$ on various volumes	81
A.16.	Kurtosis B_{4,Q_2} as a function of h_1 on the pseudo-critical line $\lambda_{1,\text{pc}}(h_1)$ for two flavours and $N_\tau = 6$ on various volumes	82
A.17.	Maximal relative contributions of the different parts of eq. (A.34) to its total real part for 1000 random samples as a function of N_τ	82
A.18.	Maximal relative contributions of the different parts of eq. (A.35) (with the modifications due to the resummation) to its total real part for 1000 random samples as a function of N_τ	83
A.19.	Maximal relative contributions of the different parts of eq. (A.36) to its total real part for 1000 random samples as a function of N_τ	83
A.20.	Maximal relative contributions of the different parts of eq. (A.37) to its total real part for 1000 random samples as a function of N_τ	84
A.21.	Maximum of the absolute real part of eq. (A.39), divided by $\kappa^4 N_\tau^2 / N_c^2$, for 1000 random samples as a function of N_τ	84

List of Tables

- 3.1. Numerical results for the pseudo-critical line eq. (3.30), the finite-size scaling of the kurtosis eq. (3.32) and the critical point. The fits to the pseudo-critical line all have $0.04 \lesssim \chi^2/\text{d.o.f.} \lesssim 0.65$, the ones to the kurtosis $0.29 \lesssim \chi^2/\text{d.o.f.} \lesssim 1.48$. 42

Erklärung nach § 30 (12) Ordnung für den Bachelor- und den Masterstudiengang

Hiermit erkläre ich, dass ich die Arbeit selbstständig und ohne Benutzung anderer als der angegebenen Quellen und Hilfsmittel verfasst habe. Alle Stellen der Arbeit, die wörtlich oder sinngemäß aus Veröffentlichungen oder aus anderen fremden Texten entnommen wurden, sind von mir als solche kenntlich gemacht worden. Ferner erkläre ich, dass die Arbeit nicht – auch nicht auszugsweise – für eine andere Prüfung verwendet wurde.

Frankfurt, den 5. November 2020

Miguel Salg